Trapping and Rydberg Excitation of a Single Atom Qubit in a Blue Detuned Bottle

Ву

Siyuan Zhang

A dissertation submitted in partial fulfillment of the requirements for the degree of

Doctor of Philosophy
(Physics)

at the
UNIVERSITY OF WISCONSIN-MADISON
2012

Date of final oral examination: 09/26/12

The dissertation is approved by the following members of the Final Oral Committee:

Mark Saffman, Professor, Physics Thad Walker, Professor, Physics Deniz Yavuz, Assistant Professor, Physics Robert McDermott, Associate Professor, Physics Martin Zanni, Professor, Chemistry To my mom and dad.

ACKNOWLEDGMENTS

First, I wish to thank my advisor Prof. Mark Saffman. Mark introduced me to the exciting world of atomic and optical physics and quantum computation. He sets an excellent example of how to conduct successfuly research with great big ideas and attention to details. He taught me how to write scientific papers and has been very supportive on my thesis work. Mark has been patient with us when the results are slow and always provide insightful ideas at the right moment. I am very grateful that Mark is my advisor.

Another person I owe a lot of thanks to is Gang Li. Gang taught me a lot of nice experimental skills of optical physics and atom trapping. His optimism, persistence, and intellectual sparks were the key ingredients for the success of the single atom trapping in the bottle beam trap after the experiment had been stuck in many problems for almost two years. Without his cooperation, the experiment in this thesis could not have been as successful.

I am also greatly thankful to Larry Isenhower for all the lasers he has built for the experiment, for all his bright insights and help when we run into problems and puzzles. Withous Marty Lichtman's labview programs, the experiment would not have started running at all. And I would like to thank Tian Xia and Alex Carr for their great contribution in the tomography experiment, Kara Maller for designing the asphere and setting up the lasers, and Michal Piotrowicz for the working of Gaussian latices.

In addition, I would like to thank Thomas Neal and Johannas Nipper for teaching me the basics of MOT when I was new to the lab. I greatly appreciate the valuable experience passed on from the Rb experiment by Xianli Zhang and Alex Gill. Jinlu Miao has been a great and supportive friend. And it has been great pleasure to work with all other people in the group.

Finally, I would like to take this special chance to thank my parents. My parents have always been

understanding and have faith in me. Without their sustaining support, I could not have gone so far with scientific research.

TABLE OF CONTENTS

		I	Page
LI	ST O	F TABLES	vii
LI	ST O	F FIGURES	viii
1	Intr	roduction	1
	1.1 1.2 1.3	Quantum Computer Neutral atom QC Optical Dipole Trap	2
2	Bot	tle Beam Trap	8
	2.1	Gaussian Interference Bottle Beam	10
	2.2	2.1.2 Trap Calculations Vortex Bottle Beam 2.2.1 Laguerre-Gaussian Vortex Beam	13 14
	2.3 2.4	Gaussian Lattice Trap	
		2.4.1 Gaussian Interference BBT 2.4.2 Vortex BBT 2.4.3 Gaussian Lattice BBT 2.4.4 Summary	21 22
	2.5	Scalability	
3	Qua	asi-magic trapping of ground and Rydberg state atoms	27
	3.1 3.2 3.3	Ponderomotive Energy of Rydberg Atoms	28
	3.4 3.5	Ponderomotive Energy Shift in Bottle Beam Traps	31 34
		3.5.1 Photoionization rate of Bottle Beam/Gaussian lattice	36

			Page				
		3.5.2 Blackbody Radiation Photoionization	. 37				
4	Exp	perimental Setup	. 40				
	4.1	Magneto Optical Trap	. 40				
		4.1.1 MOT Temperature	. 41				
		4.1.2 Loading Time and Atom Density Measurements	. 42				
	4.2	Optical Setup of the BoB Module					
	4.3	Filtering Test					
	4.4	Optical Pumping					
		4.4.1 Bias Magnetic Field	. 45				
	4.5	State Detection	. 45				
5	Sin	gle Atom Loading	. 49				
	5.1	Timing Sequence	. 49				
	5.2	Results	. 50				
	5.3	Atom Temperature					
	5.4	Lifetime Measurement					
	5.5	Collisional Atom Loss	. 54				
6	Gro	ound State Rabi	. 57				
	6.1	Rabi Frequency Calculation	. 59				
	6.2	AC Stark shift	. 61				
	6.3	Raman Laser Setup	. 61				
	6.4	Experimental Results of TPS and RFE	. 63				
	6.5	T2 measurements	. 66				
	6.6	Decoherence Factors	. 66				
		6.6.1 Motional Decoherence	. 66				
		6.6.2 Magnetic Field Fluctuations	. 69				
	6.7	Quantum Tomography	. 69				
		6.7.1 State Tomography	. 71				
		6.7.2 Process Tomography	. 72				
7	Rydberg Excitation						
	7.1	Rabi Frequency	. 75				
	7.2	TPS and RFE	. 76				
	7.3	Photoionization Rate	. 79				

Appendix

				P	age
	7.4	Rydbei	rg Energy Shift in Bottle Beam Trap		81
	7.5		rg Lifetime		
		7.5.1	Decay of Rydberg States		82
		7.5.2	Model of Rydberg Atom Loss with Multiple Rydberg Ionization Pulses .		85
		7.5.3	Direct Lifetime Measurement with Ground State Blowaway		92
		7.5.4	Monte Carlo Simulation of Rydberg Decay		92
8	Sun	nmary .			96
LI	ST O	F REFE	ERENCES		97
Al	PPEN	DICES			
			Zemax Designs		
	App	enaix B:	Electric Field of a Strongly Focused Gaussian Beam		109

LIST OF TABLES

Table		Page	е
2.1	Trap Frequencies of the Dipole Traps for Cs 6s, $\lambda=780~\mathrm{nm}$, power $P=50~\mathrm{mW}$ for a) Gaussian interference BBT $w_1=2~\mu\mathrm{m}$, $w_2=3.78~\mu\mathrm{m}$, b) crossed vortex BBT $w_0=3~\mu\mathrm{m}$, $\theta=8.6^o$, and c) Gaussian lattice trap $w_0=1.5~\mu\mathrm{m}$, $d=4~\mu\mathrm{m}$. 20	О
2.2	Comparison of the Gaussian interference BBT, vortex BBT, and Gaussian lattice trap.	23	3
3.1	Parameters for the Cs model potential (Equation 3.6)	. 29	9
3.2	Self-magic conditions for selected n states in a Gaussian lattice trap with $\lambda=780~\mathrm{nm},$ $d=4~\mu\mathrm{m}.$. 33	3
4.1	Calibration of Andor Luca camera (camera quantum efficiency @852nm taken into account)	. 43	3
4.2	Performance of different filter combinations to filter out background light from the 532nm light in the atom detection path with $0.2W$ of $532nm$ light out of Verdi	. 44	4
5.1	Photon sources for the background counts in the single atom readout signal. With integration time $t=100 \mathrm{ms}, n_{bg}\approx 85.\ldots\ldots\ldots\ldots\ldots\ldots$. 51	1
6.1	Process tomography results for single qubit gates. The fidelity measures used are $F_{\rm O}^{1/2}={\rm Tr}\left[\sqrt{\sqrt{\chi_{\rm meas}}\chi_{\rm id}\sqrt{\chi_{\rm meas}}}\right], F_{\rm O}={\rm Tr}^2\left[\sqrt{\sqrt{\chi_{\rm meas}}\chi_{\rm id}\sqrt{\chi_{\rm meas}}}\right], F_{\rm D}=1-\frac{1}{2}{\rm Tr}\left[\sqrt{(\chi_{\rm id}-\chi_{\rm meas})^{\dagger}(\chi_{\rm id}-\chi_{\rm meas})}\right].$. 73	3
7.1	Measurement of transition frequency (in GHz) of $ 6S_{1/2}, F=4, m_F=0\rangle \rightarrow 61D_{3/2}, m_F=1/2\rangle$.	$m_J =$. 79	= 9
7.2	Scaling coefficients of Cs in Equation 7.7, data taken from [Beterov 09]	. 85	5
A.1	Parameters of the custom Optimax aspheric lens, CT=15mm, DIA=20mm, CA=18mm	n. 103	3

LIST OF FIGURES

Figu	re	Page
1.1	(a)Ground state Raman transition and (b)Rydberg excitation of Cs used in experiments	3
1.2	(a)Rydberg blockade mediated controlled phase gate, (b)CNOT gate constructed from controlled phase gate	4
1.3	(a)Red detuned and (b)blue detuned optical dipole trap.	5
2.1	(color online) Scalar polarizability of ground and Rydberg states of Rb and Cs. The vector polarizability of the ground state is shown by the dashed lines	9
2.2	Optical setup of Gaussian BBT.	11
2.3	Trapping depth in the xy and xz plane for Gaussian interference BBT, λ =780nm, $w_1 = 2\mu\text{m}$, $w_2 = 3.78\mu\text{m}$, P=0.05W	12
2.4	Intensity profile in different transverse planes for Gaussian interference BBT, λ =780nm, $w_1=2\mu\mathrm{m},w_2=3.78\mu\mathrm{m},\mathrm{P}$ =0.05W	12
2.5	(a)A diagram showing a helical surface of equal phase with the Poynting vector indicated by a curved line[Dennis 09], (b) a spiral phase plate.	13
2.6	Creation of vortex BoB.	14
2.7	Trapping depth in the xy and xz plane for vortex BoB, λ =532nm, d =6mm, f =34mm, $w_0 = 3\mu$ m, P=0.3W, trapping depth $T_{trap} = 192\mu$ K	16
2.8	Intensity profile in different transverse planes for vortex BoB, λ =532nm, d =6mm, f =34mm, $w_0 = 3\mu$ m, P=0.3W	16
2.9	Measured(a) and theoretical(b) intensity profile in different transverse planes, and reconstructed 3D profile for vortex BoB, λ =532nm, d =6mm, f =34mm, $w_0 = 3\mu$ m, P=0.3W	17

Figur	re I	Page
2.10	(a)Trap depths, (b)trap sizes, and (c)trap frequencies of crossed vortex BBT for different waist size with $\theta=5{\rm deg}$ (tan $\theta=0.088$), $\lambda=532{\rm nm}$, P=0.3W	17
2.11	(a)Trap depths, (b)trap sizes, and (c)trap frequencies of crossed vortex BBT for different θ with $w_0=3\mu\mathrm{m}$, λ =532nm, P=0.3W	18
2.12	Optical setup of Gaussian lattice trap	18
2.13	Intensity profile in different transverse planes for Gaussian lattice trap, λ =780nm, $d=4\mu\mathrm{m}, w_0=1.56\mu\mathrm{m}, P=50\mathrm{mW}.$	19
2.14	Trapping depth in the xy and xz plane for Gaussian lattice trap, λ =780nm, $d=4\mu\mathrm{m}$, $w_0=1.56\mu\mathrm{m}$, P=50mW	19
2.15	Gaussian lattice (a)trap depth, (b)potential at the trap center, and (c)the ratio between the two, with different Gaussian beam waist, λ =780nm, $d=4\mu\mathrm{m}$, P=50mW	20
2.16	Trap potential with different phase differences for the Gaussian lattice BBT, λ =780nm, $d=4\mu\mathrm{m},w_0=1.56\mu\mathrm{m},\mathrm{P}$ =50mW	22
2.17	Trapping depth in the xy and xz plane for Gaussian lattice trap with $\phi_1=\pi$, $\phi_2=\pi$, λ =780nm, $d=4\mu\mathrm{m}$, $w_0=1.56\mu\mathrm{m}$, P=50mW, and (c)optical setup of non-interfering Gaussian lattice trap	23
2.18	Schematic for creating a trap array with a diffraction beam splitter	24
2.19	Beam quality of of vortex beam arrays for different aspect ratio, with the HOLO-OR MS-049-Q-Y-A beam splitter $l=87\mu\mathrm{m}$, $\lambda=532\mathrm{nm}$, (a) $w_1=115\mu\mathrm{m}$, (b) $w_1=154\mu\mathrm{m}$. 25
2.20	Beam quality of Gaussian beam arrays for different aspect ratio, with the HOLO-OR MS-049-Q-Y-A beam splitter $l=87\mu\mathrm{m}$, $\lambda=532\mathrm{nm}$, (a) $w_1=115\mu\mathrm{m}$, (b) $w_1=154\mu\mathrm{m}$. 26
2.21	Schematic for creating a trap array with a calcite beam displacer and a diffraction beam splitter	26
3.1	Wavefunctions of Cs Rydberg states calculated from the model potential method	30

Appendix Figure		Page
3.2	(color online) Potential energy of Cs ground and ns Rydberg states in a) Gaussian interference BoB, b) vortex BoB, and c) Gaussian lattice BoB. Trap parameters are: power $P=50~\mathrm{mW}$ for a) Gaussian interference BoB $w_1=2~\mu\mathrm{m},w_2=3.78~\mu\mathrm{m}$, b) crossed vortex BoB $w=3~\mu\mathrm{m},\theta=8.6^{o}$, and c) Gaussian lattice trap $w=1.5~\mu\mathrm{m},d=4~\mu\mathrm{m}.$. 32
3.3	(color online) Energy shift compensation for the crossed vortex BoB with a planewave of intensity $I_m=128~\mu\mathrm{W}/\mu\mathrm{m}^2$, $w=3~\mu\mathrm{m}$, $\theta=8.6^{\circ}$, and $P=50~\mathrm{mW}$. 33
3.4	(color online) Trapping potential (top row) and shift difference (bottom row) between Cs $6s$ and $125s$ for a self-magic Gaussian lattice trap with $\lambda=780$ nm, $d=4$ μ m, $w=1.56$ μ m, and $P=50$ mW	. 34
3.5	Self-magic conditions for different nS states in a Gaussian lattice trap with $\lambda=780~\mathrm{nm},d=4~\mu\mathrm{m}.$. 35
3.6	Average transition shift between ground and 125s states of Cs in Gaussian lattice trap with $d=4~\mu\mathrm{m}$, $w=1.57~\mu\mathrm{m}$, $P=50~\mathrm{mW}$, and $U_{\mathrm{trap}}=k_B\times300~\mu\mathrm{K}$. 35
3.7	Photoionization rate for 125s Cs in a 780nm self-magic Gaussian lattice dipole trap, $w_0=1.56~\mu\mathrm{m},d=4~\mu\mathrm{m},P=50~\mathrm{mW},\mathrm{and}~U_{\mathrm{trap}}=k_B\times300~\mu\mathrm{K}.$. 38
3.8	(color online) Reconstructed field intensity by inverse Fourier transformation from discretized Fourier components for a Gaussian lattice dipole trap, $\lambda=780 \mathrm{nm}, w_0=1.56~\mu\mathrm{m}, d=4~\mu\mathrm{m}.$. 38
3.9	Blackbody radiation induced photoionization rate for Cs Rydberg states	. 39
4.1	(a)D2 line transition of Cesium and (b) setup of the magneto optical trap (MOT)	. 40
4.2	MOT imaging optics	. 42
4.3	MOT loading time measurement, $\tau=1.7\mathrm{s.}$. 42
4.4	(a)Optical layout and (b)picture of the green crossed vortex bottle beam setup	. 47
4.5	(a)Cesium transition line and (b) saturated absorption spectrum [Sacher] of the 894nm optical pumping laser for the clock state.	. 48

5.1

Appendix Figure		Page
5.2	(a)Typical photon counter data for a lifetime measurement with cooling light on, and continuous readout.(b)Histogram of photon counts for atom loading, integrated for 100ms, loading probability=47%	50
5.3	Temperature measurements of a single atom in a 200 μ K vortex BoB, (a) with one stage PGC at detuning -6Γ , (b) with two stage PGC at detuning -6Γ and -10Γ	53
5.4	Lifetime of a single atom in a 380 μ K vortex BoB	53
5.5	Lifetime of a single atom in a vortex BoB for different trapping depth	54
5.6	Calculated collisional atom lifetime in the trap with the cooling light on (bright) and off (dark), along with experimental lifetime data represented by error bar data points	56
6.1	(a)Two photon Raman transition, (b)Raman transition of the Cs ground hyperfine states	. 58
6.2	Caculated Rabi frequency and AC Stark shift of ground state Raman transition, from $6S_{1/2}, F=4, m_F=0$ to $6S_{1/2}, F=3, m_F=0$ via $7P_{1/2}, m_F=1, P_1=1$ mW, $P_2=0.5$ mW, $w_{457}=5.9\mu$ m	62
6.3	Laser setup for the Raman transition of the ground hyperfine states	64
6.4	Two photon spectrum of the ground Raman transition, with fitted $f_c=-13 \mathrm{kHz}$, $\Omega_R=53 \mathrm{kHz}$. The beam parameters are $P_1=0.93 \mathrm{mW}$, $P_2=0.47 \mathrm{mW}$ with some misalignment, $w=5.9 \mu \mathrm{m}$, $\Delta=40 \mathrm{GHz}$	65
6.5	Rabi flopping of ground hyperfine states, $P_1=0.93 \mathrm{mW}, P_2=0.47 \mathrm{mW}, w=5.9 \mu \mathrm{m},$ $\Delta=40 \mathrm{GHz}, f_{RF}=9.192620 \mathrm{GHz},$ Rabi frequency $\Omega/2\pi=0.31 \mathrm{MHz},$ amplitude $A=0.95.\ldots$	65
6.6	Ramsey fringes for different T_p intervals	66
6.7	T2 decoherence time fit	67
6.8	Calculated (a)motional decoherence T_2 time for Cs atom in a 532nm BBT, (b)decoherence caused by magnetic field fluctuations.	
6.9	χ matrices for the process tomography of different rotation gates	74
7.1	Two photon excitation of Cs Rydberg state	76

Appe Figur		Page
7.2	Calculated Rabi frequency and AC Stark shift of two photon excitation to $61D_{3/2}$ Rydberg state via $7P_{1/2},\ P_{459}=65\mu{\rm W},\ w_{459}=6\mu{\rm m},\ P_{1038}=3.5{\rm mW},\ w_{1038}=2.8\mu{\rm m},\ \Delta/2\pi=2{\rm GHz},\ (a)(b)\ m_J=-1/2,\ (c)(d)m_J=-3/2.\ .\ .\ .\ .\ .\ .\ .\ .\ .\ .\ .\ .\ .$	77
7.3	TPS scan of Cs Rydberg state $61D_{3/2}$. (a)pulse sequence for detecting Rydberg state with 1038nm laser photoionization, in which Rydberg excitation pulse $r=0.6\mu\mathrm{s}$, high power 1038 ionization pulse $r_i=2\mu\mathrm{s}$, and a gap time of $r_g=10\mu\mathrm{s}$ is used to enhance retention. (b)TPS curve, with $f_{center}=733.131\pm0.043\mathrm{MHz}$, half line width $df=0.768\mathrm{MHz}$	78
7.4	Rabi flopping between ground state $6S_{1/2}$, $F=4$, $m_F=0$ and Rydberg state $61D_{3/2}$, $m_F=1/2$	
7.5	Cross section of photoionization of Cs Rydberg states	80
7.6	Cross section of photoionization of Cs Rydberg states for different wavelengths	82
7.7	(a)Radial matrix element for transitions $60F \to nD$, (b)relative radial matrix element for transitions from $nS_{1/2}$ bound states to $P_{1/2}$ free states	83
7.8	Ponderomotive energy shift of Rydberg states in the crossed vortex BBT, with trap parameters λ =532nm, d =6mm, f =34mm, $w_0 = 3\mu m$, P=0.4W	84
7.9	Two photon spectrum of Cs $61D_{3/2}$, (a)with the BBT on, $f_{center}=367.514\pm0.02 \mathrm{MHz}$; (b)with BBT off, $f_{center}=367.547\pm0.03 \mathrm{MHz}$	84
7.10	Lifetime of Rydberg states, (a)0K lifetime, (b)blackbody lifetime at 300K, (c)lifetime at 300K	85
7.11	Model of Rydberg atom decay and loss	86
7.12	Rydberg lifetime model fit, varying $P_{r,0}$. (a) $r_i=0$, and 5 repetitions; (b) $r_i=2\mu s$, gap time r_g after 1038 pulse r_i , and 5 repetitions; (c) $r_i=2\mu s$, gap time r_g before 1038 pulse r_i , and 5 repetitions; (d) $r_i=2\mu s$, gap time r_g after 1038 pulse r_i , 1 repetition, Shade area is the experimental Rabi flopping amplitude uncertainty range.	89
7.13	Rydberg lifetime model fit, varying $\tau_{bob} = 1/\Gamma_{bob}$. (a) $r_i = 0$, and 5 repetitions; (b) $r_i = 2\mu s$, gap time r_g after 1038 pulse r_i , and 5 repetitions; (c) $r_i = 2\mu s$, gap time r_g before 1038 pulse r_i , and 5 repetitions; (d) $r_i = 2\mu s$, gap time r_g after 1038 pulse r_i , 1 repetition. Shade area is the experimental Rabi flopping amplitude uncertainty range.	90

Appe Figur		Page
7.14	Rydberg lifetime model fit, varying $\tau_{1038}=1/\Gamma_{1038}$. (a) $r_i=0$, and 5 repetitions; (b) $r_i=2\mu s$, gap time r_g after 1038 pulse r_i , and 5 repetitions; (c) $r_i=2\mu s$, gap time r_g before 1038 pulse r_i , and 5 repetitions; (d) $r_i=2\mu s$, gap time r_g after 1038 pulse r_i , 1 repetition, Shade area is the experimental Rabi flopping amplitude uncertainty range.	91
7.15	Lifetime measurement of Rydberg state $61D_{3/2}$ with the bottle trap (a)on and (b)off	92
7.16	Verification of the numerical lifetime calculation. (Solid lines represent calculated values from the empirical Equation 7.7, and dotted lines represent numerical results).	93
7.17	Verification of the Monte Carlo simulation, assuming Rydberg Cs atom $61D_{3/2}$ decays directly the ground state	94
7.18	Ground state population results of Monte Carlo decay simulation for Cs state $61D_{3/2}$, $T=300K$, (a)ground state population, with blue dots representing the simulation, red solid curve represents the lifetime curve, time constant $\tau_{red}=77.5\mu\text{s}$, $\tau_{blue}=143\mu\text{s}$, (b)the average time the atom spent on each intermediate state before decaying to the ground state.	95
A.1	Performance of the focusing aspheric lens (a)before and (b)after adding a correction lens	104
A.2	(red)Intensity profile of a pure LG_{01} mode with $w_0=3\mu\mathrm{m}$; (blue)intensity profile calculated from diffraction, with a Gaussian beam of waist $w_{in}=f\lambda/\pi w_0$ passing through a spiral phase plate, and focused by a lens of focal length f ; (black)intensity profile calculated from diffraction, with a Gaussian beam of waist $w_{in}=1.3f\lambda/\pi w_0$ passing through a spiral phase plate, and focused by a lens of focal length f	105
A.3	Layout of the optical system for making the vortex bottle beam trap	105
A.4	Zemax POP modeling of the crossed vortex BBT, (a)(c) are assuming the alignments are perfect, (b)(d) include tolerances with up to 0.5mm lens decentering and 0.5 deg lens tilting.	107
A.5	Measurement of the waist size of the final focused vortex beam (single beam), (a)camera picture, (b)(c)1D intensity profile, measured data(black dots),theoretical calculation from LG_{01} mode with $w_0=3\mu\mathrm{m}$ (red line), and Zemax simulation(blue dashed)	
R 1	Flectric field of a strongly focused Gaussian beam	110

Appe Figur	endix re	Page
B.2	Field at the focus for different focusing powers with $\lambda=852\mathrm{nm},f=4.5\mathrm{mm},$ and (a)(b) $w_1=1.1\mathrm{mm},$ (c)(d) $w_1=1.8\mathrm{mm},$ (e)(f) $w_1=2.7\mathrm{mm},$ and the field amplitudes are normalized to $ E_1 $ on the front surface of the lens	. 112
B.3	Scattering ratio of strongly focused Gaussian beam of a single atom for different waist sizes.	. 113
B.4	Transmission of strongly focused Gaussian beam for a single atom (a)at resonance and (b)at different laser detunings	. 115
B.5	Phase shift of strongly focused Gaussian beam for a single atom at different laser detunings	. 115

TRAPPING AND RYDBERG EXCITATION OF A SINGLE ATOM QUBIT IN A BLUE DETUNED BOTTLE BEAM

Siyuan Zhang

Under the supervision of Professor Mark Saffman At the University of Wisconsin-Madison

This thesis covers the first demonstration of a single neutral atom qubit trapped in a blue detuned optical dipole trap, and the use of this trap to trap Rydberg atoms. A T_2 decoherence time of 42 ms is achieved; process tomography of a complete set of single qubit gates is performed to show a gate fidelity of 70% to 80%; and a Rydberg trapping time longer than the spontaneous decay time is observed.

Three types of blue detuned bottle beam traps are designed and analyzed for different experimental needs. The ponderomotive energy shifts of Rydberg states in the bottle beam traps are numerically calculated and a quasi-magic trapping method is presented. Atoms are cooled by a magneto-optical trap. Single atoms are loaded into the crossed vortex bottle beam trap with a sub-Poissonian number distribution. Two phase locked 457nm lasers are used to coherently Rabi flop Cs atoms between the F=3 and F=4 ground states via a two-photon Raman transition. A 459nm laser and a 1038nm laser stabilized by high finesse cavities are used to drive a two photon transition between the ground F=4, $m_F=0$ state and a Rydberg state.

These preliminary results of long coherence time and Rydberg trapping time in the bottle beam trap set the ground work for future work on building a qubit array with blue detuned optical dipole traps.

Chapter 1

Introduction

1.1 Quantum Computer

As of 2012, the minimum feature size of an integrated circuit is 22nm, and the semiconductor industry is working towards the next 14nm node. With the size of a classical computer getting smaller and smaller, it is natural for scientists to think about building a computer from single atoms or electrons. As it turns out, a quantum computer is not just a smaller successor of a classical computer, it sets itself completely apart due to the effects of quantum mechanics.

A quantum computer is a quantum system that uses quantum states (called qubits) to store information and to carry out computation. A well defined qubit has a quantum state basis that is usually labeled as $|0\rangle$ and $|1\rangle$. The qubit can be in state $|0\rangle$, $|1\rangle$, or in a superposition of these two states $a|0\rangle+b|1\rangle$, due to the quantum nature of the system. If we consider N qubits in a pure state, the system could be represented by $a_0|0...00\rangle+a_1|0...01\rangle+...+a_{2^N-1}|1...11\rangle$. That means we can perform operations effectively on 2^N input numbers with only one input quantum state. Based on this quantum parallelism, a quantum computer can solve certain problems much more effectively than a classical computer. Listed below are some examples.

(1)searching in an unsorted list. With a quantum computer using Grover's algorithm[Grover 97], the time complexity is $O(N^{1/2})$ with storage space $O(\log N)$, while with a classical computer the complexity is O(N) in time, for a list of size N.

(2) factoring big numbers. On a quantum computer using Shor's algorithm [Shor 94], it takes time $O((\log N)^3)$ to factor a large number N, which is exponentially faster than any known algorithms on a classical computer.

Moreover, as in the original proposition of Richard Feynman, quantum computers are extremely useful to run simulations of quantum many body systems[Blatt 12, Kassal 08, Abrams 97]. With only a few hundred qubits, a quantum computer could beat any classical supercomputer available.

To qualify as a practical quantum computer, a system must satisfy the following requirements[DiVincenzo 01]:

- (1)Scalable system with well characterized qubits
- (2) Ability to initialize the system to a simple state
- (3)Long decoherence times
- (4)A universal set of quantum gates
- (5) Qubit-specific state measurement capability
- (6) Ability to interconvert stationary and flying qubits
- (7) Ability to faithfully transmit flying qubits between locations

The last two requirements are related to quantum networks. Many quantum systems have been studied to build a quantum computer. The most advanced ones are cold ions, superconductor circuits, quantum dots, linear optics, impurity vacancies and neutral atoms. Among them, the cold ion system holds the record of fidelity so far (above 99%), and has implemented error correction[Schindler 11], and quantum simulation with up to 5 qubits. The superconductor system has demonstrated greatly improved decoherence time recently, with $T_2 \sim 20 \mu s$ compared with the gate time of $\sim 10 ns$ [Paik 11], and it looks very promising in the future for implementing surface codes[DiVincenzo 09]. The impurity vacancy system has demonstrated very long quantum information storage times up to 180 s[Steger 12, Maurer 12], which makes it very favorable to be used as quantum storage.

1.2 Neutral atom QC

The most distinctive feature of the neutral atom system compared with the cold ion system is the absence of strong Coulomb forces, so that coupling to stray fields is low. And compared with the solid state systems, neutral atoms could be easily cooled to motional ground states, and the coupling to the environment is weak. These features would suggest a long decoherence time for a neutral atom quantum computer. In order for a large scale quantum computer to work, strong qubit-qubit coupling is necessary. Two qubit gates in neutral atom systems can be implemented by collisions[Jaksch 99], photon mediated gates in a high finesse cavity[Pellizzari 95], and strong dipole-dipole interactions[Jaksch 00]. The collisional gate is relatively slow, and the photon mediated gate is not easily scalable, so we are pursuing the dipole-dipole interaction gate mediated by Rydberg levels.

The computational basis states we are using are the hyperfine ground states of Cs (Figure 1.1), which are separated by 9.2GHz. The clock states ($m_F = 0$) are chosen because of their insensitivity to magnetic field fluctuations. A two photon Raman transition is used to coherently drive the atom from state $|1\rangle$ to state $|0\rangle$, in order to be able to address the atoms individually.

The scaling of the Van der Waals interaction between two atom is very rapid $V \propto n^{11}$. By exciting

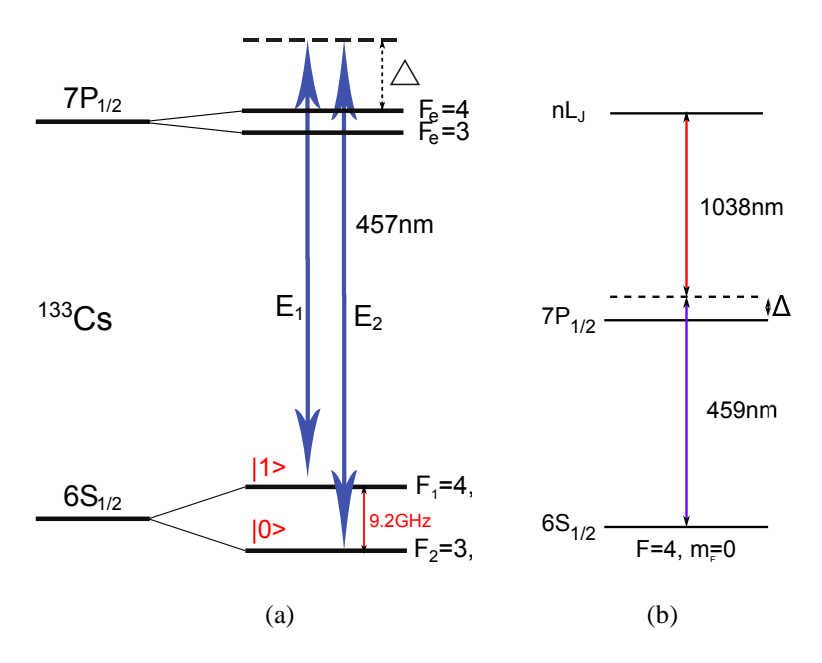


Figure 1.1 (a)Ground state Raman transition and (b)Rydberg excitation of Cs used in experiments.

the atoms to high lying Rydberg states, we can induce strong dipole-dipole interactions between two nearby atoms. The Rydberg interaction occurs because of either a direct dipole-dipole interaction in a hybridizing electric field or by the Forster mechanism in zero electric field. Either way, the interaction will result in a shift in the two-Rydberg-atom energy level by B. In the limit of large

dipole-dipole frequency shift, $B\gg |\Omega_R|$, where Ω_R is the Rydberg excitation Rabi frequency, we will get the Rydberg blockade. In the simple case of two atoms, the probability of exciting both atoms to the Rydberg level is $P=\frac{|\Omega_R|^2}{2B^2}$, which will be small when $B\gg |\Omega_R|$.

The Rydberg blockade mediated gate is performed by applying the pulse sequence shown in Figure 1.2: (1) a π Rydberg pulse is applied on the control atom to excite it to the Rydberg level; (2) a 2π rotation is attempted on the target atom; (3) a π pulse is used to bring the control atom back to the ground state. Due to the π phase change of a 2π rotation, this sequence results in a controlled phase gate. It can be converted to a CNOT gate by adding a Hadamard gate on the target atom before and after the controlled phase operation. And according to theoretical calculations [Zhang 12], the intrinsic gate fidelity of such a neutral atom quantum system could be above 0.998. With this

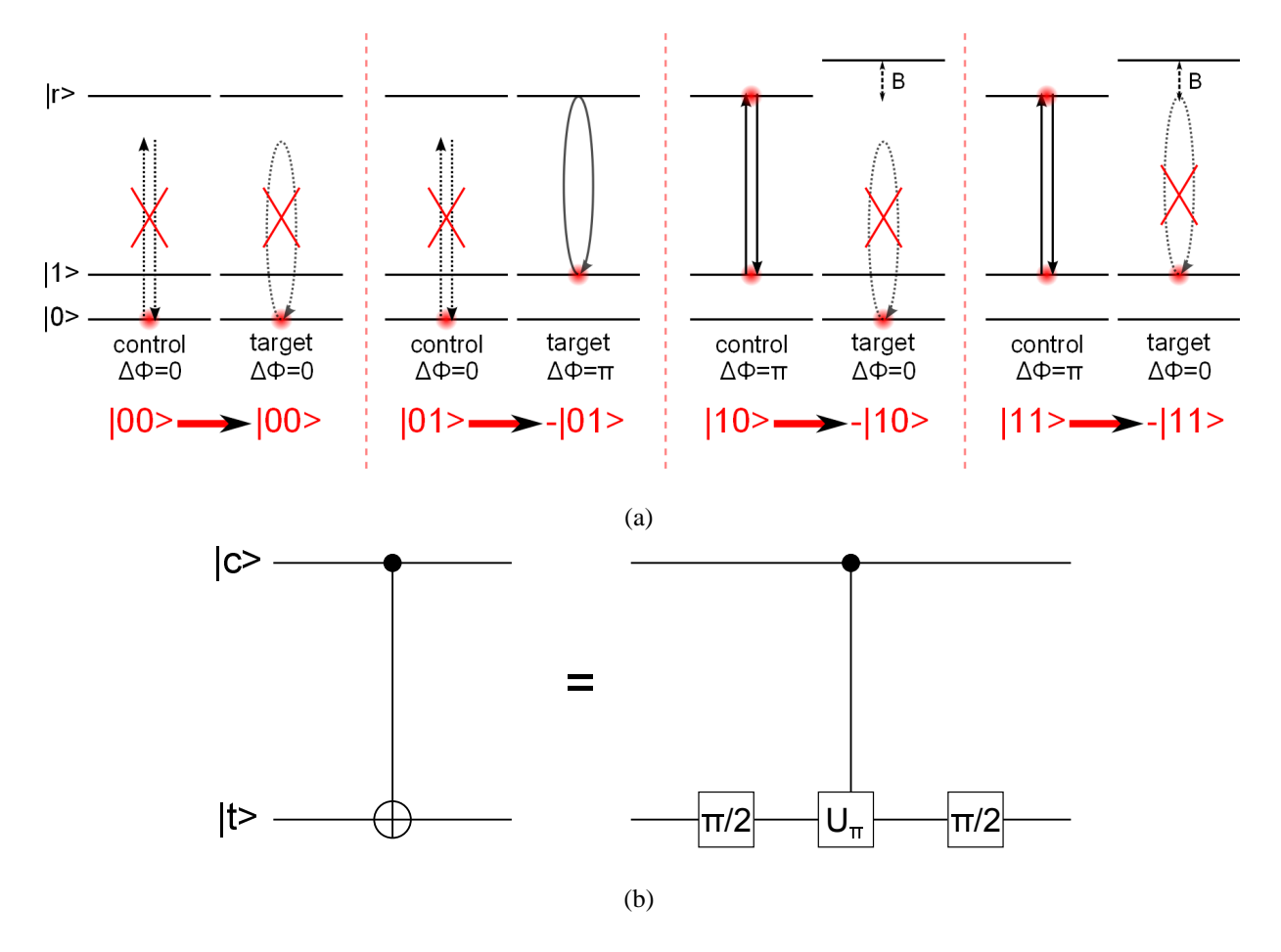


Figure 1.2 (a)Rydberg blockade mediated controlled phase gate, (b)CNOT gate constructed from controlled phase gate.

method, some previous experiments have demonstrated a CNOT gate with a measured population probability fidelity of up to 0.92 and a gate time of $6\mu s$ [Isenhower 10b, Isenhower 10a]. And the entanglement of two neutral atoms via Rydberg blockade has been demonstrated with a Bell state fidelity of F=0.58 after correcting for background collisional losses[Zhang 10].

1.3 Optical Dipole Trap

According to Grimm et al [Grimm 00], in a far detuned laser field, an atom experiences an optical dipole potential

$$U_{dip} = -\frac{1}{2\epsilon_0 c} \alpha I, \tag{1.1}$$

where α is the atomic polarizability, and I is the light intensity.

In a simplified two level system, the dipole potential and scattering rate can be expressed as

$$U_{dip}(\vec{r}) = \frac{3\pi c^2}{2\omega_0^3} \frac{\Gamma}{\Delta} I(\vec{r}), \qquad (1.2)$$

$$\Gamma_{sc}(\vec{r}) = \frac{3\pi c^2}{2\hbar\omega_0^3} \left(\frac{\Gamma}{\Delta}\right)^2 I(\vec{r}), \tag{1.3}$$

where ω_0 is the transition frequency, and $\Delta=\omega-\omega_0$ is the laser detuning. So if $\Delta<0$ (red

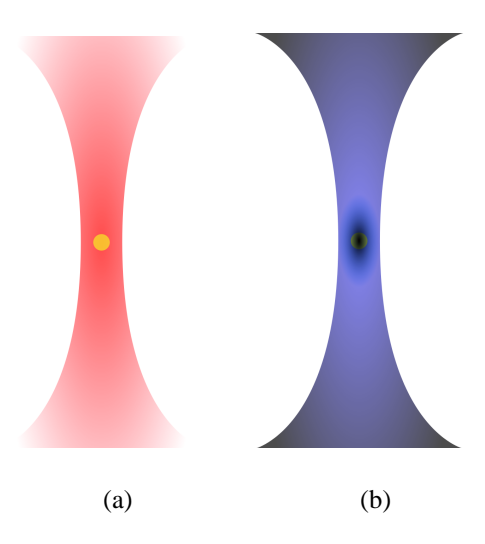


Figure 1.3 (a)Red detuned and (b)blue detuned optical dipole trap.

detuned), the potential is lower where the intensity is higher, and the atom is attracted to high

intensity regions, and if $\Delta > 0$ (blue detuned), the atom is repelled to low intensity regions, as shown in Figure 1.3.

Suppose we have a red detuned laser beam with a Gaussian intensity profile

$$I_{red}(x, y, z) = I_0 \frac{e^{-2(x^2 + y^2)/w_f^2(z)}}{1 + z^2/z_P^2},$$
(1.4)

where the Rayleigh range $z_R=\pi w_0^2/\lambda$, and the waist size at z $w_f(z)=w_0\sqrt{1+z^2/z_R^2}$, with a minimum beam waist size w_0 . With a harmonic approximation, we get maximum trapping potential $|U_m|=\frac{1}{2\epsilon_0c}|\alpha|I_0$, and the oscillation frequencies are $\omega_x=\omega_y=\frac{2}{w_{f0}}\left(\frac{|U_m|}{m}\right)^{1/2}$, $\omega_z=\frac{\sqrt{2}}{z_R}\left(\frac{|U_m|}{m}\right)^{1/2}$. For an atom with temperature T_a , whose velocities and positions obeys the Maxwell-Boltzmann distribution, the average light intensity it sees is

$$\langle I \rangle_{red} = \frac{2\epsilon_0 c}{|\alpha|} \langle U \rangle$$

$$\approx \frac{2\epsilon_0 c}{|\alpha|} (|U_m| - \frac{1}{2} m \omega_x^2 \langle x^2 \rangle - \frac{1}{2} m \omega_y^2 \langle y^2 \rangle - \frac{1}{2} m \omega_z^2 \langle z^2 \rangle)$$

$$= \frac{2\epsilon_0 c}{|\alpha|} \left(|U_m| - \frac{3}{2} k_B T \right).$$
(1.5)

If we have a blue detuned laser trap, with an intensity profile that can be approximated by

$$I_{blue}(x, y, z) \approx \frac{1}{2} m \omega_x^2 x^2 + \frac{1}{2} m \omega_y^2 y^2 + \frac{1}{2} m \omega_z^2 z^2.$$
 (1.6)

The average light intensity the atom sees is about

$$\langle I \rangle_{blue} \approx \frac{2\epsilon_0 c}{|\alpha|} \frac{3}{2} k_B T.$$
 (1.7)

Usually in experiments, the maximum trapping potential is much larger than the atomic temperature ($|U_m| > 10k_BT_a$). We can immediately see that the average light intensity shining on the atom in a blue detuned optical dipole trap is much smaller than that for a red detuned trap. This results in

- (1)less photon scattering;
- (2)less laser noise induced heating;
- (3)less differential AC Stark shifts of qubit levels due to laser intensity fluctuations.

All these will contribute to longer T_1 storage time and longer T_2 decoherence time, which means higher fidelity for our atomic qubit system. The improvements are significant especially when we can cool the atomic temperature to a very low level so that trap laser noise is dominant, because the majority of the decoherence is proportional to the average light intensity seen by the atom.

Another reason that makes a blue detuned trap favorable is related to Rydberg atoms. There is an intrinsic flaw in using a red detuned optical dipole trap: while the ground state atoms have a positive polarizability and are attracted by the high intensity laser beam, the high lying Rydberg levels have a negative polarizability and are repelled by the trap. Excitation of an atom to the repulsive Rydberg state during a gate cycle leads to heating and decoherence through entanglement of the spin and motional states[Saffman 05]. It is possible to equalize the polarizability of ground and Rydberg states with a red detuned light close to resonance, but there will be a high probability for the atom to decay out of the computational basis. So it is necessary to use a blue detuned trap. With a blue detuned optical dipole trap, we can have

- (4)less heating and less decoherence due to entanglement of the spin and motional states and escape out of the trap;
- (5)longer Rydberg lifetime due to less photoionization from the trap light.

In this thesis, we will demonstrate a single Cs atom qubit trapped in such a blue detuned dipole trap.

Chapter 2

Bottle Beam Trap

A blue detuned optical dipole trap is basically a hollow low intensity region surrounded by high intensity walls (bottle shaped).

Many groups have demonstrated trapping an ensemble of atoms in a blue detuned optical dipole trap formed by: sheets of laser light[Davidson 95], an evanescent wave and a confining cylindrical hollow beam along with the gravitational force[Ovchinnikov 97], a Laguerre-Gaussian doughnut beam closed by two additional plugging beams[Kuga 97], passing a collimated beam through a circular phase plate which imposes a π phase difference between the central and outer part of the beam[Ozeri 99], a rotating focused Gaussian beam[Friedman 00], a hollow beam formed by an axicon[Kulin 01], a dark toroid converted from a Gaussian beam with a spatial light modulator(SLM)[Olson 07], and destructively interfering two Gaussian beams with different waist sizes[Isenhower 09].

Because the atoms are confined at a point of low light intensity, long spin relaxation times[Ozeri 99, Olson 07], small differential AC Stark shifts and long coherence times of the ground state hyperfine superpositions of alkali atoms[Davidson 95, Sheng 12] have been observed in experiments. Blue detuned optical dipole traps provide ideal circumstances for precision measurements, with possible applications in atomic clocks[Davidson 95], the parity non-conservation measurements[Sheng 12], quantum information, etc.

Most of the methods mentioned above are not easily applicable to create a micro-sized trap to trap single atoms. The methods using sheets of laser beams or plugging beams impose a big challenge in beam alignment; the time averaged dynamic trap does not work on the time scale of quantum gates ($\sim \mu s$); the hollow beam formed by an axicon has complex interference structures. A modification of the π phase plate method using a SLM has demonstrated single atom trapping

recently[Xu 10]. But SLMs may not handle high power at large detunings. A blue detuned optical trap in a high finesse cavity is used to successfully trap single atoms[Puppe 07], but it is challenging to apply for scalable quantum computing. A 3-D array of single atoms has been trapped in a blue detuned optical lattice[Nelson 07], but the three dimensional structure makes it hard to address the atoms individually.

To accommodate the needs of our multi-qubit experiment, we have designed three types of such bottle beam traps (BBT): (1) Gaussian interference BBT; (2) crossed vortex BBT; (3) Gaussian lattice BBT[Zhang 11].

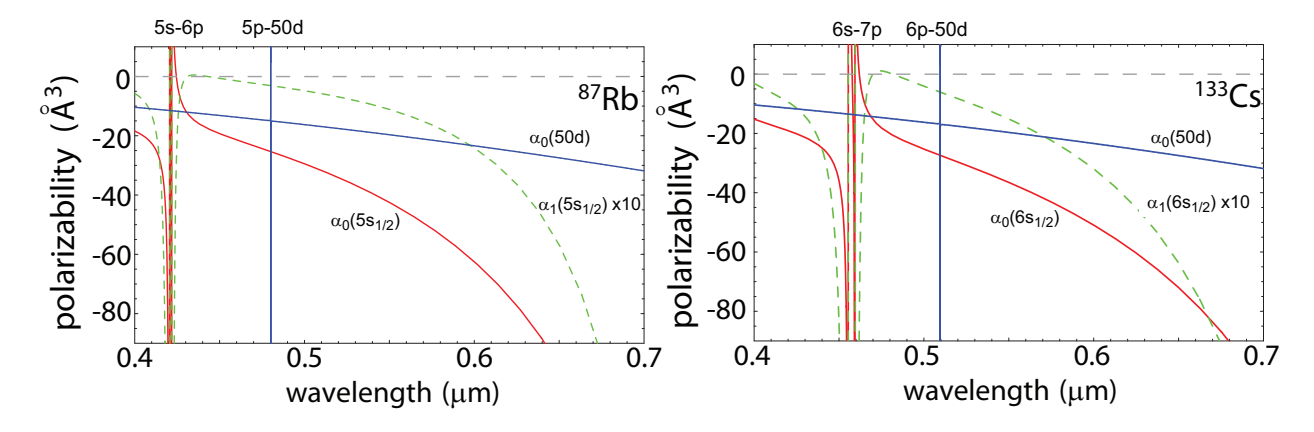


Figure 2.1 (color online) Scalar polarizability of ground and Rydberg states of Rb and Cs. The vector polarizability of the ground state is shown by the dashed lines.

First, we need to choose a proper wavelength. By inspecting Figure 2.1, it seems necessary to use a 490nm laser to match the polarizability of the ground and Rydberg state of Cs. But as will be shown in Chapter 3, matching of the polarizability does not necessarily mean matching of the AC Stark shift. As high power 532nm light is readily available by commercial solid state pumped diode lasers, we are using a 532nm laser (detuned by $2\pi \cdot 212$ THz for the Cs D2 line) in our single qubit experiment. And because of limited power of fiber coupled 532nm light, we will use a smaller detuning, 780nm (detuned by $2\pi \cdot 33$ THz for the Cs D2 line), for the multi qubit experiment.

2.1 Gaussian Interference Bottle Beam

The first type of blue dipole trap we have tried is the Gaussian interference bottle beam trap (Gaussian BBT). It basically makes use of the destructive interference between two Gaussian beams with different waist sizes [Isenhower 09].

2.1.1 Optical Setup

The optical setup is shown in Figure 2.2. A Gaussian input beam with waist w_0 goes into a Mach-Zehnder interferometer. The beam gets split at the first polarizing beam splitter. The resulting two beams go through the two arms of the interferometer, where telescope 1 of magnification M_1 and telescope 2 of magnification M_2 are located. When the two beams are recombined at the 50/50 beam splitter at the end, the waists become $w_1 = M_1 w_0$ and $w_2 = M_2 w_0$ respectively. The power ratio between the two beams is adjusted by the first $\lambda/2$ waveplate, and the polarization directions are set back to the same with the second $\lambda/2$ waveplate. One of the outputs goes to a photo detector to phase lock the optical path difference between the two arms. The other part is sent out to be used as the trap (see [Isenhower 09] for experimental details). Because each beam splitter introduces a phase shift of $\pi/2$, the two trap beams interfere destructively while the two feedback beams interfere constructively. To phase lock the optical path, a small amplitude dithering voltage of $\sim 10 \text{kHz}$ is applied to the piezo element on one of the reflection mirrors, then the photo diode signal goes in to the phase lock module, and the feedback output is sent back to the piezo element. Since the two beams have different waist sizes, if the peak intensities of them are equal, the intensity after interference would be zero only at the waist position, which becomes a bottle beam trap.

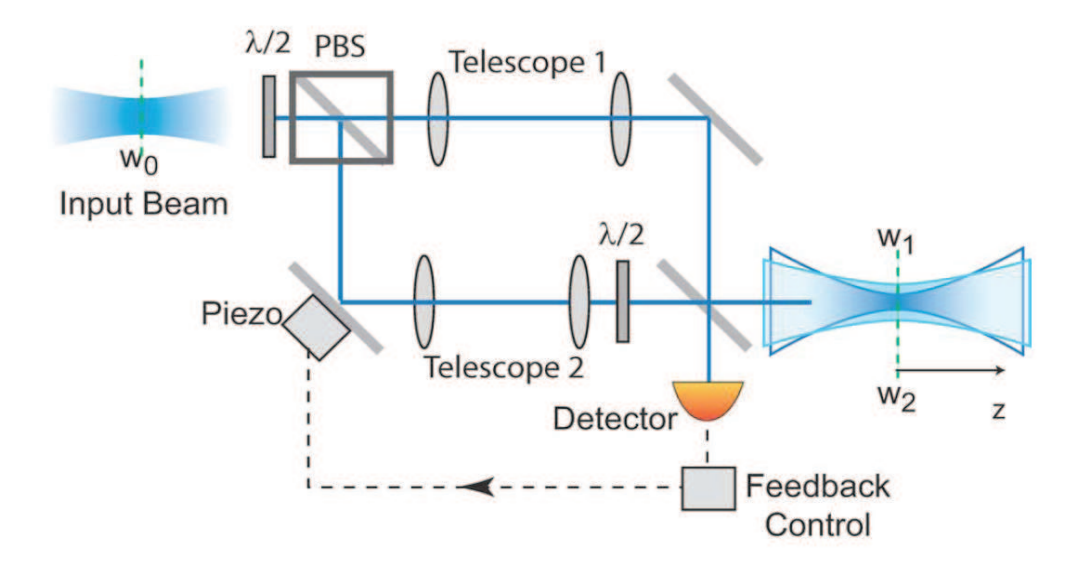


Figure 2.2 Optical setup of Gaussian BBT.

2.1.2 Trap Calculations

The light intensity can be calculated by

$$I(x,y,z) = \frac{1}{c\epsilon_0} |E_1 \frac{w_1}{w_1(z)} \exp(-\frac{r^2}{w_1^2(z)}) \exp(ikz + ik\frac{x^2 + y^2}{2R_1(z)} - i\zeta_1(z))$$

$$-E_2 \frac{w_2}{w_2(z)} \exp(-\frac{r^2}{w_2^2(z)}) \exp(ikz + ik\frac{x^2 + y^2}{2R_2(z)} - i\zeta_2(z))|^2.$$
(2.1)

From the properties of Gaussian beams, $z_R=\pi w_0^2/\lambda,\,w(z)=w_0\sqrt{1+(\frac{z}{z_R})^2}, R(z)=z+\frac{z_R^2}{z}, \zeta(z)=\arctan(\frac{z}{z_R}).$

By adjusting the relative intensities of the two beams by the half waveplate, we can make $E_1 = E_2$, so the two beams completely cancel each other at $\vec{r} = (0, 0, 0)$.

The expansion of the trapping potential around the center is

$$U(x,0,0) = -\frac{\alpha P_1(w_1^2 - w_2^2)^2}{c\epsilon_0 \pi w_1^6 w_2^4} x^4 + O(x^5)$$

$$U(0,0,z) = -\frac{\alpha \lambda^2 P_1(w_1^2 - w_2^2)^2}{c\epsilon_0 \pi^3 w_1^6 w_2^4} z^2 + O(z^2)$$

Keeping w_1 constant, the lowest order coefficients are maximized when $q = w_2/w_1 = \sqrt{(3 + \sqrt{17})/2} \simeq 1.89$. Figure 2.3 and Figure 2.4 show some plots of the theoretical trapping potential and intensity profiles for such a Gaussian interference BBT.

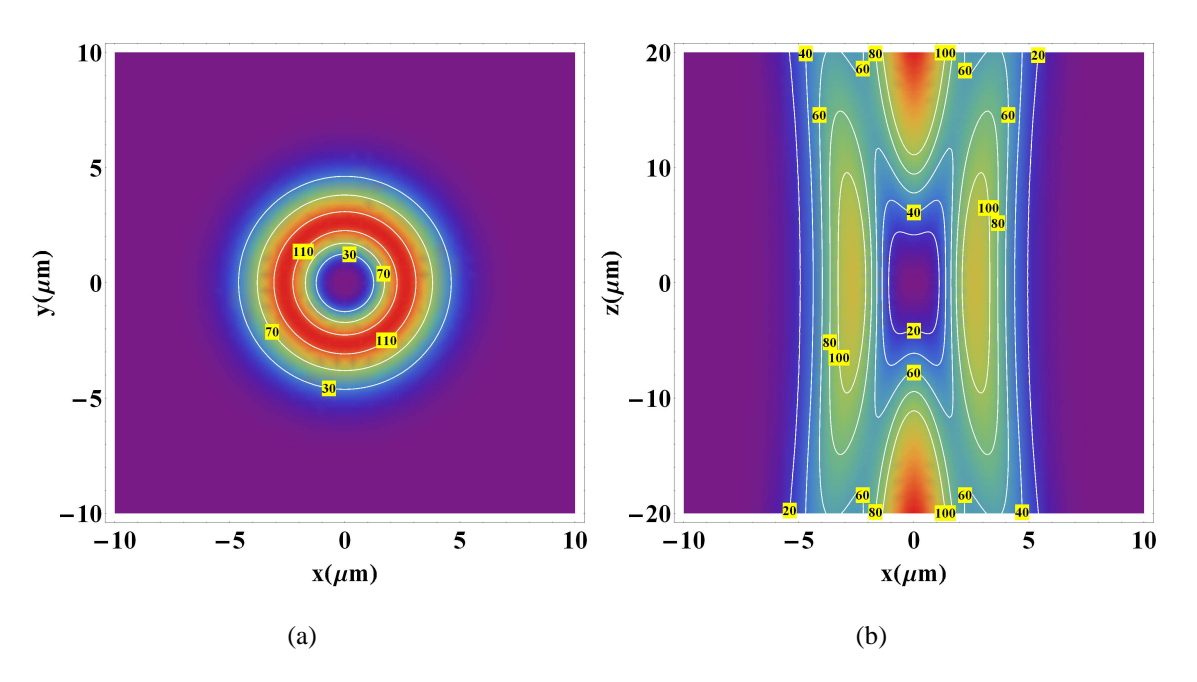


Figure 2.3 Trapping depth in the xy and xz plane for Gaussian interference BBT, λ =780nm, $w_1 = 2\mu\text{m}$, $w_2 = 3.78\mu\text{m}$, P=0.05W.

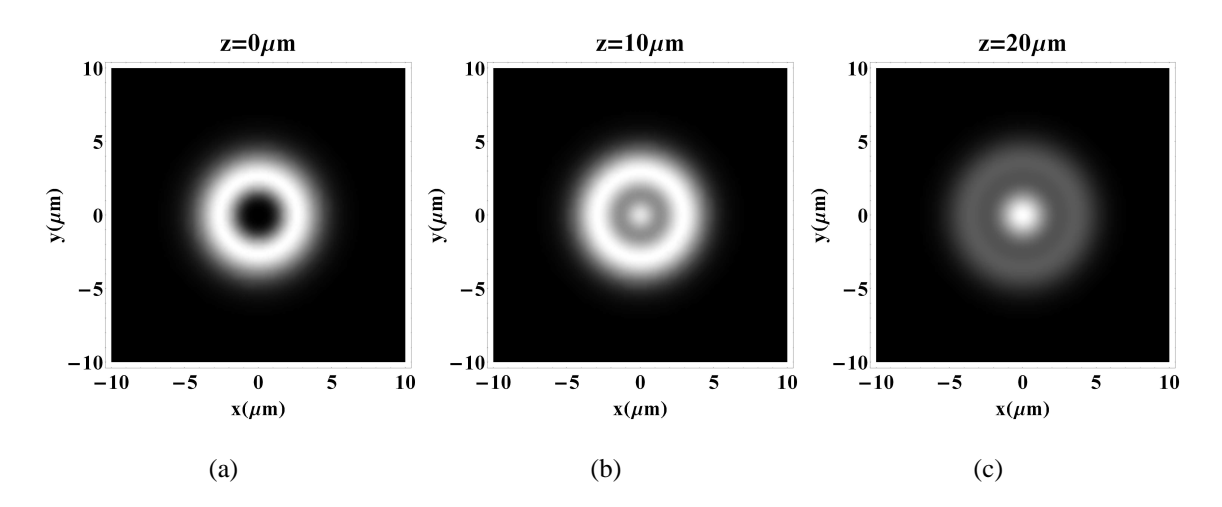


Figure 2.4 Intensity profile in different transverse planes for Gaussian interference BBT, λ =780nm, $w_1=2\mu\mathrm{m},\,w_2=3.78\mu\mathrm{m},\,\mathrm{P}$ =0.05W.

2.2 Vortex Bottle Beam

The second type of trap is a crossed vortex bottle beam trap(vortex BBT). An optical vortex is a zero of the optical field. Vortices are dark points in 2D fields and dark lines in 3D fields. The integral of the phase of the field around the optical axis is an integer multiple of 2π ($E \propto e^{im\phi}$, the integer m is called topological charge), so the fields interfere destructively at the axis, creating a vortex. Vortex beams have a helical wavefront like the one in Figure 2.5. They carry orbital angular momentum of $m\hbar$. Vortex beams have been widely used in creating optical tweezers to trap objects that would be repelled or damaged by conventional bright tweezers, or to actuate small particles to move around the optical axis[Grier 03]; they are of interest to the quantum computing community because of the infinite possibility of states with the topological charges as compared to the 0 and 1 states of conventional photonic qubits, so they can lead to faster data manipulation and broader communication bandwidth; the angular momentum of them has been studied in quantum entanglement[Dennis 09].

Vortex beams can be created by spiral phase plates, computer generated holograms, and conversion of Hermite-Gaussian modes. We are using a spiral phase plate in our experiment.

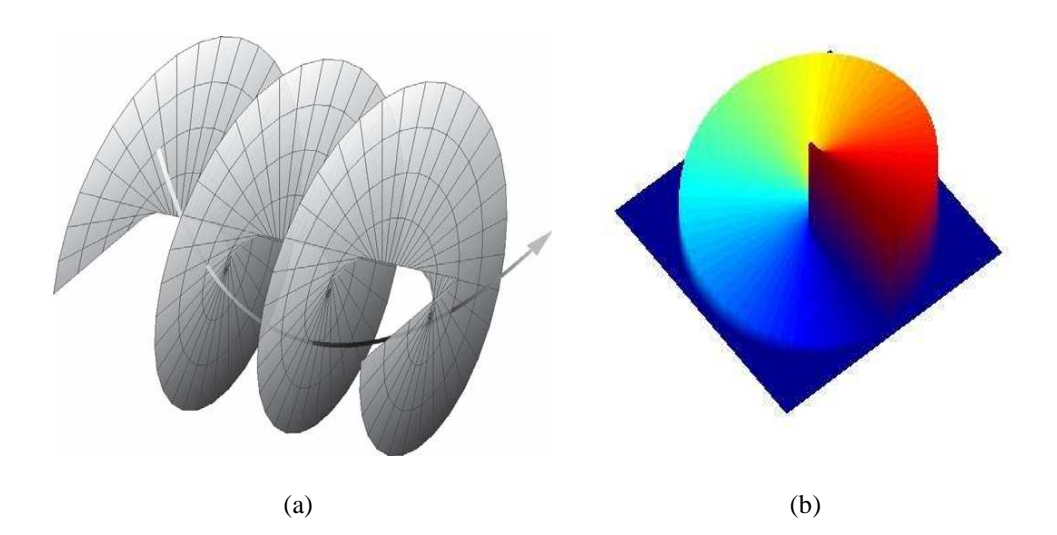


Figure 2.5 (a)A diagram showing a helical surface of equal phase with the Poynting vector indicated by a curved line[Dennis 09], (b) a spiral phase plate.

By crossing two vortex beams, we can create a bottle shaped blue detuned optical dipole trap. Such a blue crossed vortex trap was first used by the Fatemi group as an effective way to dynamically manipulate atomic clouds[Fatemi 07]. But their design requires precision alignment of the two vortex beams which would be hard on the μ m scale. So we modified the optical design to Figure 2.6(the detailed lens layout is in Sec.A.1.2 in the appendix). We split one vortex beam to

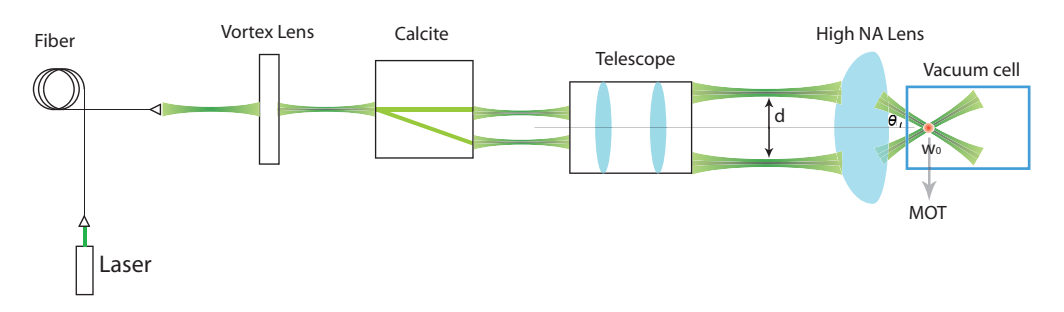


Figure 2.6 Creation of vortex BoB.

two identical parallel vortex beams by a beam displacer. Two parallel beams will naturally cross at the focal point of a focusing lens. By focusing two parallel vortex beams with a high numerical aperture aspheric lens, we get a μ m-sized crossed vortex bottle trap at the lens focus.

2.2.1 Laguerre-Gaussian Vortex Beam

Laguerre-Gaussian modes are one set of solutions to the paraxial Maxwell's equation. They can be approximately created by sending a Gaussian beam through a vortex lens (i.e. a phase plate). By passing a TEM_{00} mode laser beam through a spiral phase plate, the beam gets a phase modulation of $e^{i\phi}$, but no modulation of the intensity. So the output beam is not a pure Laguerre-Gaussian mode. But according to [Beijersbergen 94], 78.5% of the energy is in the LG_{01} mode. So we will use pure Laguerre-Gaussian mode field distributions for our theoretical treatment of the trap. More exact calculations of the field could be done by the Collins-Huygens diffraction integral method[Mawardi 11]. As shown in Sec. A.1.2, near the focus, the beam could very well be described by a pure LG_{01} mode with a proper waist size.

A Laguerre-Gaussian beam can be modeled by [Svelto 98]

$$E(r,\phi,z) = E_0 \frac{C_{lp}^{LG}}{w(z)} (\frac{\sqrt{2}r}{w(z)})^{|l|} \exp(-\frac{r^2}{w^2(z)}) L_p^{|l|} (\frac{2r^2}{w^2(z)}) \exp(ikz + ik\frac{r^2}{2R(z)} + il\phi - i(2p + |l| + 1)\zeta(z)).$$
(2.3)

The intensity

$$I(r,z) = I_0 \left(\frac{C_{lp}^{LG}}{w(z)}\right)^2 \left(\frac{2r^2}{w^2(z)}\right)^{|l|} \exp\left(-\frac{2r^2}{w^2(z)}\right) \left(L_p^{|l|} \left(\frac{2r^2}{w^2(z)}\right)\right)^2, \tag{2.4}$$

where
$$I_0 = \frac{P}{w_0^2}$$
, $C_{lp}^{LG} = \sqrt{\frac{2p!}{\pi(l+p)!}}$, $w(z) = w0\sqrt{1 + (\frac{z}{z_R})^2}$, $z_R = \frac{\pi w_0^2}{\lambda}$, $R(z) = z + \frac{z_R^2}{z}$, $\zeta(z) = \arctan(\frac{z}{z_R})$.

The vortex bottle beam is made by focusing two parallel $LG_{p=0}^{l=1}$ Laguerre-Gaussian beams to cross at the focus of a high numerical aperture lens. The two beams are separated by a distance d before focusing, with the same waist size w_1 . They have perpendicular polarizations, so there is no interference. After being focused by a lens with focal length f, the waist size becomes $w_0 = \frac{f\lambda}{\pi w_1}$, the beams are rotated by $\theta = \frac{d}{2f}$ clock and counter-clock wise. The intensity of the bottle beam can be calculated by

$$I(x,y,z) = I(r = \sqrt{y^2 + (x\cos\theta + z\sin\theta)^2}, z = -x\sin\theta +z\cos\theta) + I(r = \sqrt{y^2 + (x\cos\theta - z\sin\theta)^2}, z = x\sin\theta + z\cos\theta).$$
(2.5)

The expansion of trapping depth around the center is

$$U(x,0,0) = -\frac{2\alpha P \cos^2 \theta}{c\epsilon_0 \pi w_0^4} x^2 + O(x^4),$$

$$U(0,y,0) = -\frac{2\alpha P}{c\epsilon_0 \pi w_0^4} y^2 + O(y^4),$$

$$U(0,0,z) = -\frac{2\alpha P \sin^2 \theta}{c\epsilon_0 \pi w_0^4} z^2 + O(z^4).$$

Caculated trap profiles are show in Figure 2.7 and 2.8. Figure 2.9 is the corresponding measured trap profile of the vortex BBT we have constructed in the experiments. The parameters are chosen to be the values we use in the experiment. The difference between measured and theoretical profiles is due to experimental optics misalignment as explained in Sec. A.1.2. From Figure 2.11 we can see that the trap depth does not have a strong dependence on the tilt angle θ when $\tan \theta > 0.05$, which makes it relatively easier to make.

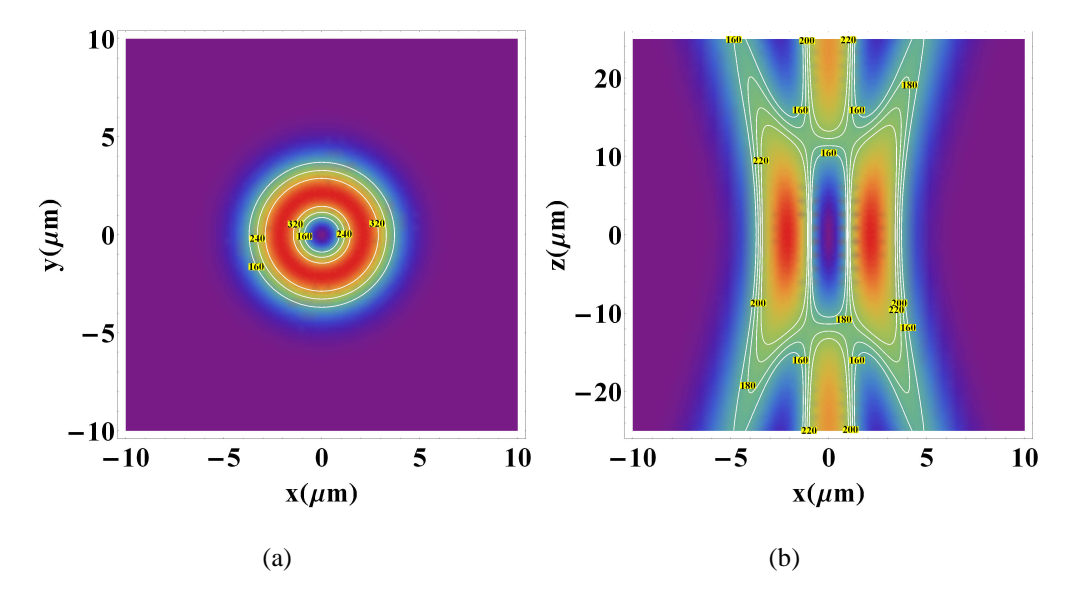


Figure 2.7 Trapping depth in the xy and xz plane for vortex BoB, λ =532nm, d=6mm, f=34mm, $w_0=3\mu\mathrm{m}$, P=0.3W, trapping depth $T_{trap}=192\mu\mathrm{K}$.

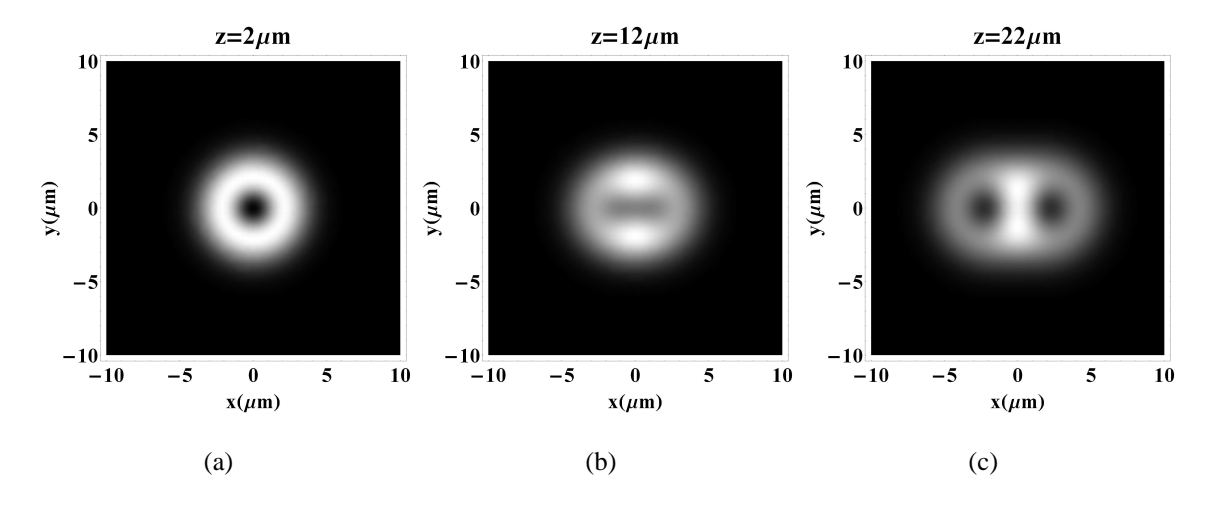


Figure 2.8 Intensity profile in different transverse planes for vortex BoB, λ =532nm, d=6mm, f=34mm, w_0 = 3 μ m, P=0.3W.

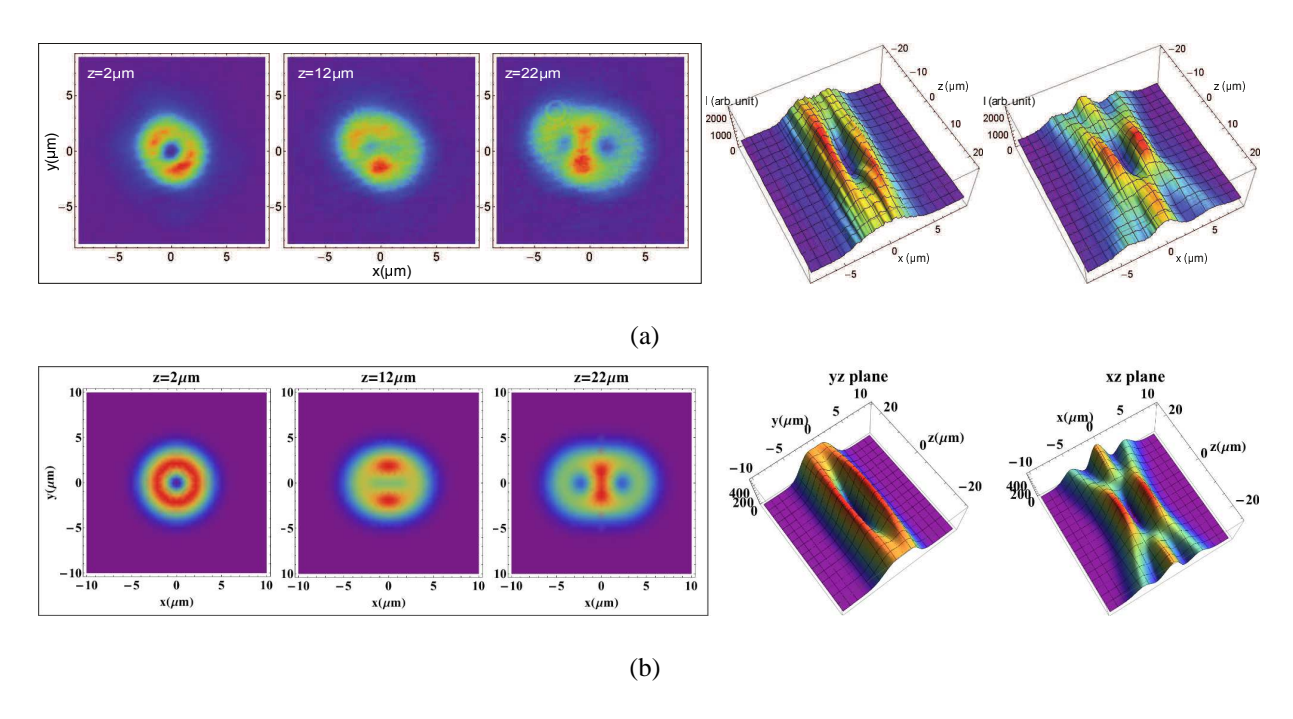


Figure 2.9 Measured(a) and theoretical(b) intensity profile in different transverse planes, and reconstructed 3D profile for vortex BoB, λ =532nm, d=6mm, f=34mm, $w_0 = 3\mu$ m, P=0.3W.

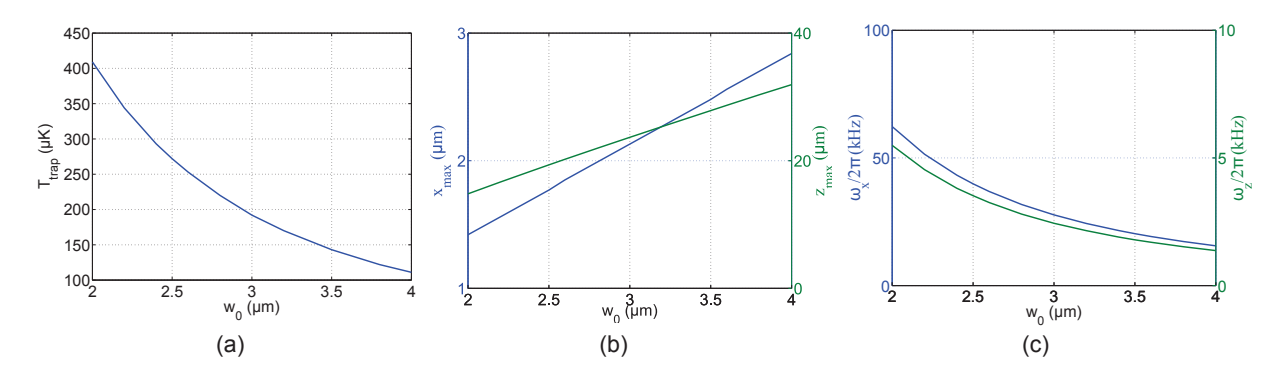


Figure 2.10 (a)Trap depths, (b)trap sizes, and (c)trap frequencies of crossed vortex BBT for different waist size with $\theta = 5\deg$ (tan $\theta = 0.088$), $\lambda = 532$ nm, P=0.3W.

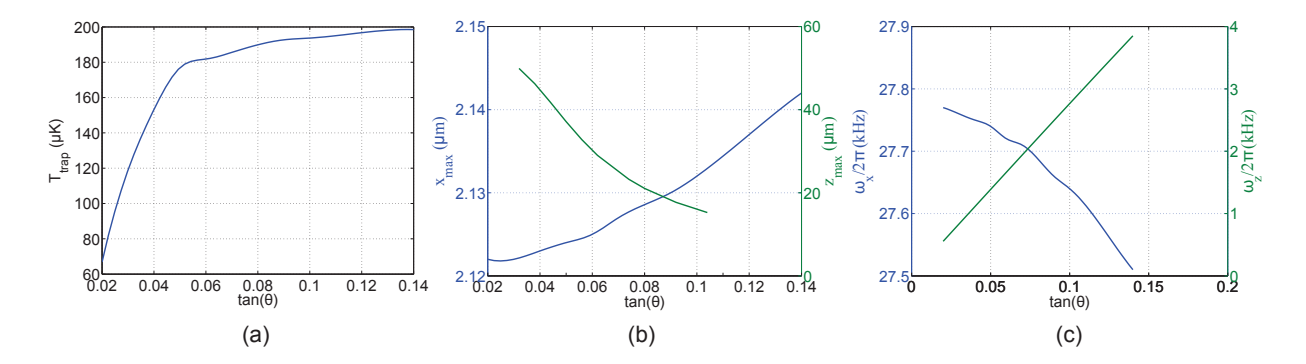


Figure 2.11 (a)Trap depths, (b)trap sizes, and (c)trap frequencies of crossed vortex BBT for different θ with $w_0 = 3\mu\text{m}$, λ =532nm, P=0.3W.

2.3 Gaussian Lattice Trap

The third type of blue detuned dipole trap we have used is the Gaussian lattice trap. Suppose there are four Gaussian beams propagating parallel to each other, with positions and polarizations as shown in Figure 2.12. Each beam has a waist size of several micrometers. Because of the small waist, they diverge very fast, thus eventually overlap in space, forming a potential barrier. With the

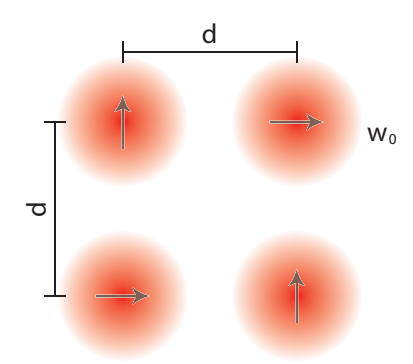


Figure 2.12 Optical setup of Gaussian lattice trap.

polarization configuration as in Figure 2.12, the light intensity can be calculated simply with the standard Gaussian beam formula.

$$E(x,y,z) = E_0 \frac{w_0}{w(z)} \exp(-\frac{r^2}{w^2(z)}) \exp(ikz + ik\frac{x^2 + y^2}{2R(z)} - i\zeta(z)),$$

$$I(x,y,z) = \frac{c\epsilon_0}{2} |E(x-d/2,y-d/2,z) + E(x+d/2,y+d/2,z)|^2 + |E(x+d/2,y-d/2,z) + E(x-d/2,y+d/2,z)|^2.$$

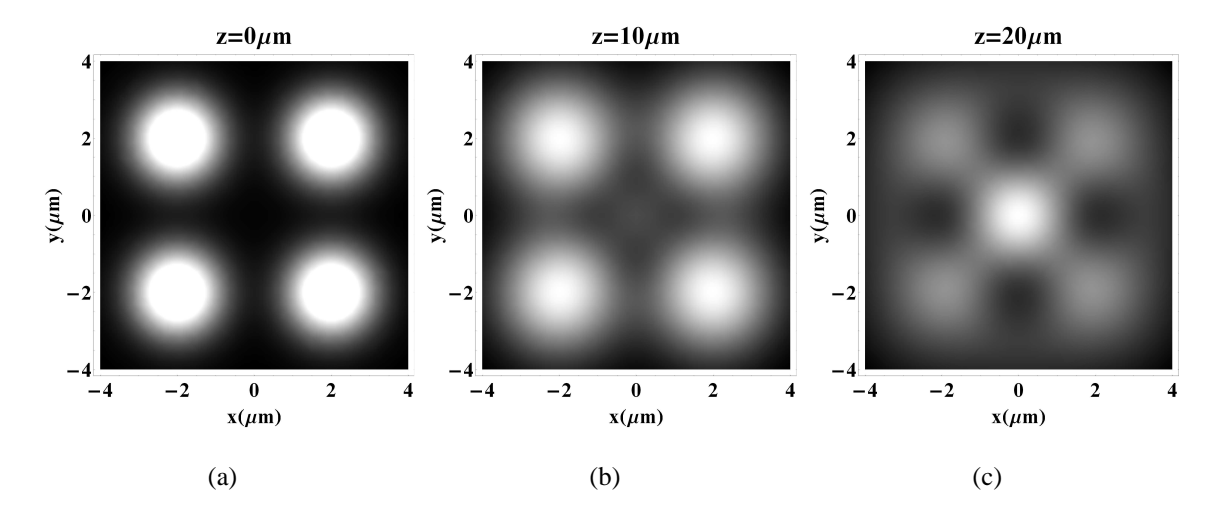


Figure 2.13 Intensity profile in different transverse planes for Gaussian lattice trap, λ =780nm, $d=4\mu\mathrm{m},\,w_0=1.56\mu\mathrm{m},\,\mathrm{P=50mW}.$

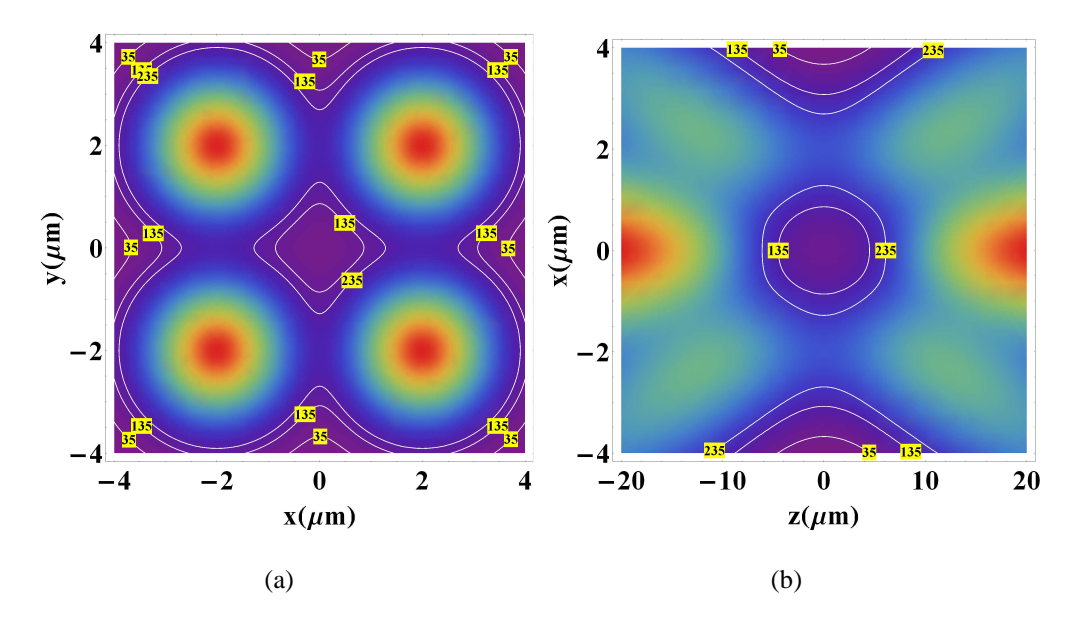


Figure 2.14 Trapping depth in the xy and xz plane for Gaussian lattice trap, λ =780nm, $d=4\mu\mathrm{m}$, $w_0=1.56\mu\mathrm{m}$, P=50mW.

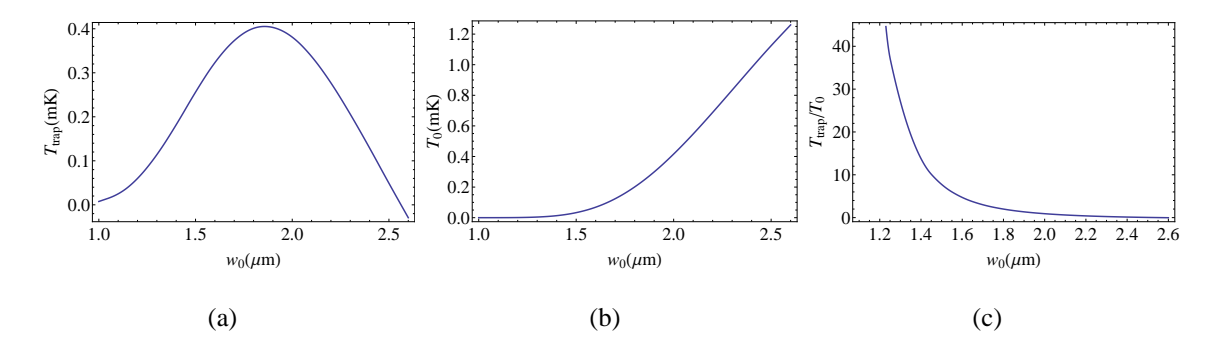


Figure 2.15 Gaussian lattice (a)trap depth, (b)potential at the trap center, and (c)the ratio between the two, with different Gaussian beam waist, λ =780nm, $d=4\mu m$, P=50mW.

The expansion of trapping depth around the center is

$$U(x,0,0) = -U_0 e^{-\frac{d^2}{w_0^2}} \left(1 - \frac{2w_0^2 - d^2}{w_0^4} x^2 \right) + O(x^3),$$

$$U(0,0,z) = -U_0 e^{-\frac{d^2}{w_0^2}} \left[1 - \frac{\lambda^2 (w_0^2 - d^2)}{\pi^2 w_0^6} z^2 \right] + O(z^3).$$
(2.6)

2.4 Comparison of Three Traps

To compare the three types of traps, trap frequencies along different axes and trap depths are listed in Table 2.1, all with the same laser power and some typical trap size.

Table 2.1 Trap Frequencies of the Dipole Traps for Cs 6s, $\lambda=780$ nm, power P=50 mW for a) Gaussian interference BBT $w_1=2~\mu\mathrm{m}$, $w_2=3.78~\mu\mathrm{m}$, b) crossed vortex BBT $w_0=3~\mu\mathrm{m}$, $\theta=8.6^o$, and c) Gaussian lattice trap $w_0=1.5~\mu\mathrm{m}$, $d=4~\mu\mathrm{m}$.

	$\omega_x/2\pi$ (kHz)	$\omega_y/2\pi~(\mathrm{kHz})$	$\omega_z/2\pi$ (kHz)	$U/k_B (\mu \mathrm{K})$
Gaussian Interference BBT	62.51	62.51	0.315	60
Vortex BBT	29.4	29.8	4.42	225
Gaussian Lattice	15.4	15.4	2.79	256

2.4.1 Gaussian Interference BBT

The Gaussian interference BBT has the strongest radial confinement and is the closest to a square well ($\sim \rho^4$ dependence to the lowest order). But it has the least axial confinement and the lowest trap depth with the same power. In addition, three of the main issues with Gaussian interference BBT are:

- 1) there needs to be a constant dithering of the piezo mirror for the phase lock, so the trap depth is fluctuating at a frequency of several kHz, this could heat up the atom. Although it is possible to make a lock without any modulation[Hansch 80, Bateman 10], this would add complexity to the system, and the trap stability depends very much on the environment such as air currents and vibrations.
- 2) we are losing a lot of the power to the photo detector. Taking into account the imperfect transmission of the lens system, we were getting at most 35% of the input power to the atom. So the power efficiency of the trap is very low.
- 3) the requirements on the overlap of the optical axes and the waist positions are strict. The final focused beam waist is about $2\mu m$, and the Rayleigh length is about $16\mu m$. A lot of time needs to be spent on making sure that each lens is added at the confocal position, and aligning the directions of the two beams very carefully before each experiment.

2.4.2 Vortex BBT

The vortex BBT has a relatively large tolerance on the beam size and beam separation, so it is relatively easy to construct and is more stable over time. But it uses two beams that are separated by more than 6mm for a lens of a diameter 20mm. This off-axis focusing could cause coma and other aberrations, and thus poses a relatively high requirement on the lens quality. The most important problem with it is that it is not easily scalable as explained in Section 2.5. So we will not use this type of trap to build our multi qubit Rydberg atom quantum computer.

2.4.3 Gaussian Lattice BBT

The most obvious disadvantage of this type of trap is the non-zero light intensity at the trap center. This could lead to decoherence between the two ground states of the atom because of different AC Stark shifts. But if the detuning is large enough, the differential AC Stark shift would be negligible. And as will be shown in Chapter 3, it is actually advantageous to have finite light intensity at the trap center to suppress the differential AC Stark shift between ground and Rydberg states.

Another issue comes from interference. In the setup shown in Figure 2.12, each diagonal beam pair have the same polarization, so they interfere. If we add a phase difference of ϕ_1 and ϕ_2 for each beam pair respectively, the trap potential curves change with phases as in Figure 2.16. The 2D potential map for the totally out of phase case is shown in Fig 2.17. We can see that

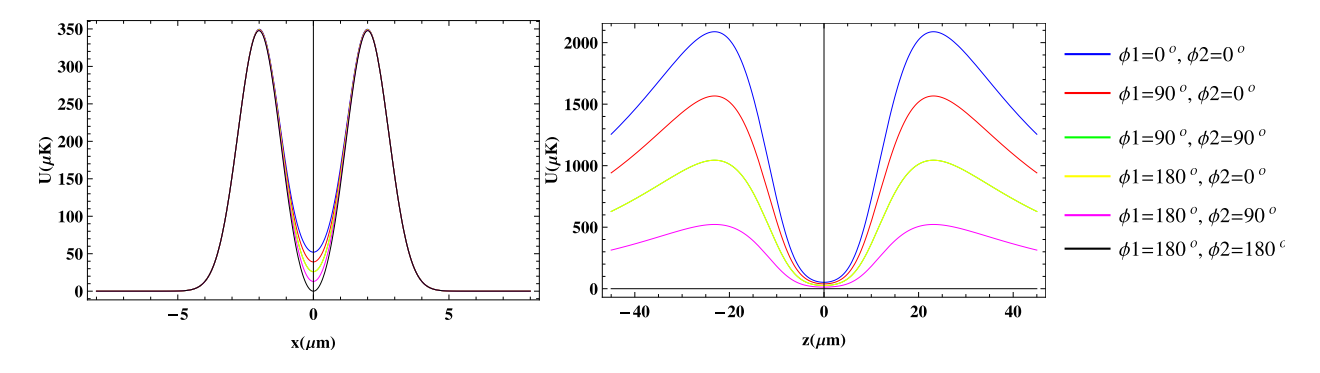


Figure 2.16 Trap potential with different phase differences for the Gaussian lattice BBT, λ =780nm, $d=4\mu\text{m}$, $w_0=1.56\mu\text{m}$, P=50mW.

the phase difference has little effect in the x and y directions. In the z direction, if the phase differences are close to the completely out-of-phase condition $\phi_1 = \pi$ and $\phi_2 = \pi$, the trap loses its confining property, and the atom could escape along the z axis, otherwise the trap depth is still limited by the intensity on the xy plane. Since all of the four beams go through the same optics, chances of them falling into the out-of-phase zone would be very small. Moreover, this issue could be completely resolved by adopting a slightly different design as shown in Figure 2.17.c [Saffman 12]. By combining two sets of beams with slightly different frequencies, the interference

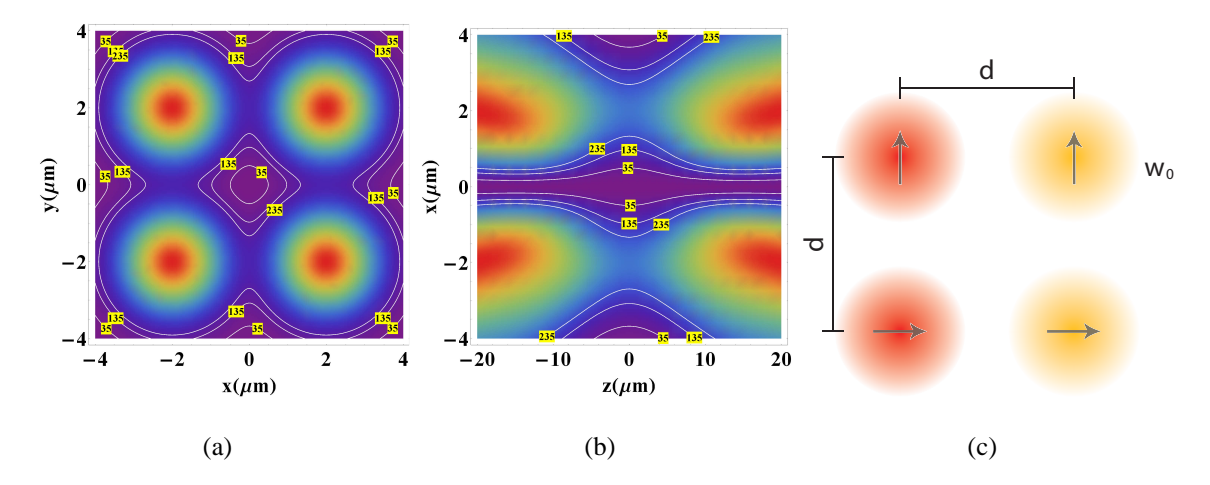


Figure 2.17 Trapping depth in the xy and xz plane for Gaussian lattice trap with $\phi_1=\pi,\phi_2=\pi,$ λ =780nm, $d=4\mu\mathrm{m},\,w_0=1.56\mu\mathrm{m},\,\mathrm{P=50mW},\,\mathrm{and}$ (c)optical setup of non-interfering Gaussian lattice trap.

could be eliminated. But special care needs to be devoted to the alignment of the two sets of beams in this scheme.

2.4.4 Summary

Table 2.2 summarizes the advantages and disadvantages of the three types of traps.

Table 2.2 Comparison of the Gaussian interference BBT, vortex BBT, and Gaussian lattice trap.

	pros	cons	
Gaussian	square well like radial confinement	weak axial confinement, low energy ef-	
Interference		ficiency, need lock, low tolerance on	
BBT		alignment precision	
Vortex BBT	easy to construct, stable	not scalable, off-axis focusing	
Gaussian Lat-	easily scalable, one wall between	non-zero intensity at trap center, hard	
tice	neighboring trap sites	to align, phase induced trap depth fluc-	
		tuation	

2.5 Scalability

If we use a diffractive beam splitter to duplicate the trap, there is a limitation of how small an aspect ratio d/w_f we can get (where d is the site to site separation, and w_f is the characteristic waist size of the trap). The reason is explained in the rest of this section.

The schematic of the diffractive beam splitter setup is shown in Figure 2.18. By inserting a

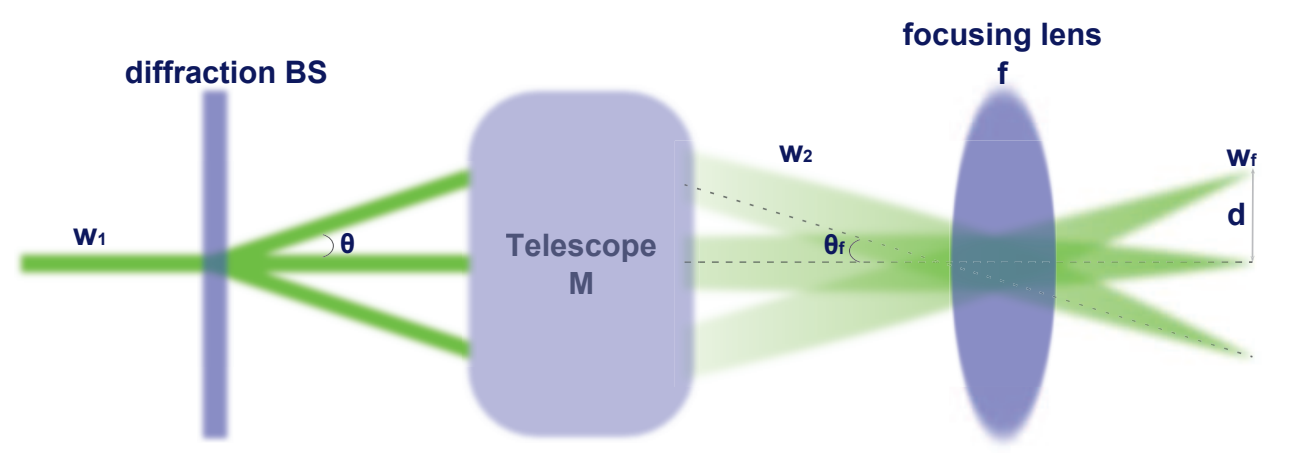


Figure 2.18 Schematic for creating a trap array with a diffraction beam splitter.

diffractive beam splitter on the Fourier plane of the image plane, the input beam with a waist size of w_1 is split with a separation angle of θ . The separation angle of a diffraction grating is $\theta = \lambda/l$, where l is the grating period. After passing through some telescope system with magnification M, the beam waist becomes $w_2 = Mw_1$, and the angle separation becomes $\theta_f = \theta/M$. With a final focusing lens of focal length f, the final waist size $w_f = f\lambda/(\pi w_2)$, and trap separation $d = f\theta_f$. Then, the aspect ratio becomes

$$\frac{d}{w_f} = \frac{f\theta/M}{f\lambda/(\pi M w_1)} = \frac{\pi w_1 \theta}{\lambda} = \frac{\pi w_1}{l}.$$
 (2.7)

If we need an aspect ratio of 3 for example, $w_1/l = 3/\pi$, which means the input beam of the diffractive beam splitter sees less than 2 periods of the grating. This would greatly reduce the beam quality of the output beams. Examples of the performance of the diffractive beam splitter for different beam sizes are shown in Figure 2.19 and Figure 2.19. We can clearly see a better beam quality when we move the grating very fast which means we are sampling more grating periods in

effect, and the vortex beam becomes noisy when the aspect ratio is about $\pi w_1/l = 4.15$. For a trap with a high requirement of the beam phase and shape, like the vortex and Gaussian interference BBTs, it would be impossible to get a small aspect ratio with a diffractive beam splitter. We will have to use computer generated holograms to create the vortex array. With the Gaussian lattice BBT, with less fine structures, the tolerance is larger, but the grating still could not go too far.

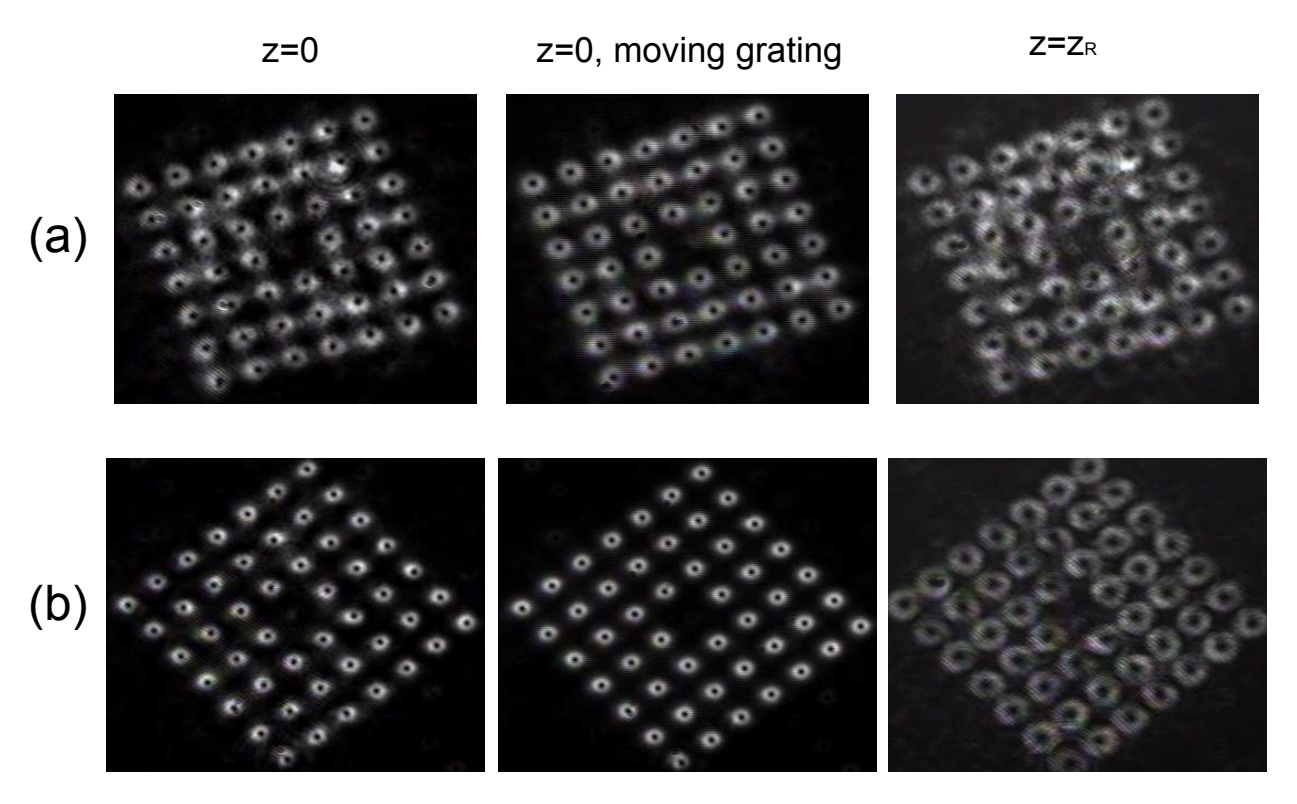


Figure 2.19 Beam quality of of vortex beam arrays for different aspect ratio, with the HOLO-OR MS-049-Q-Y-A beam splitter $l=87\mu\mathrm{m}$, $\lambda=532\mathrm{nm}$, (a) $w_1=115\mu\mathrm{m}$, (b) $w_1=154\mu\mathrm{m}$.

One way around the problem is to add some calcite beam displacers to double the beams on a conjugate plane of the image plane, as shown in Figure 2.21.

This strategy would not work well for the vortex BBT, because the two vortex crossing beams at each site would have the same polarization because of the additional calcites, causing phase fluctuation dependent interference problems. But this scheme is naturally favorable for the Gaussian lattice BBT design as shown in [Saffman 12]

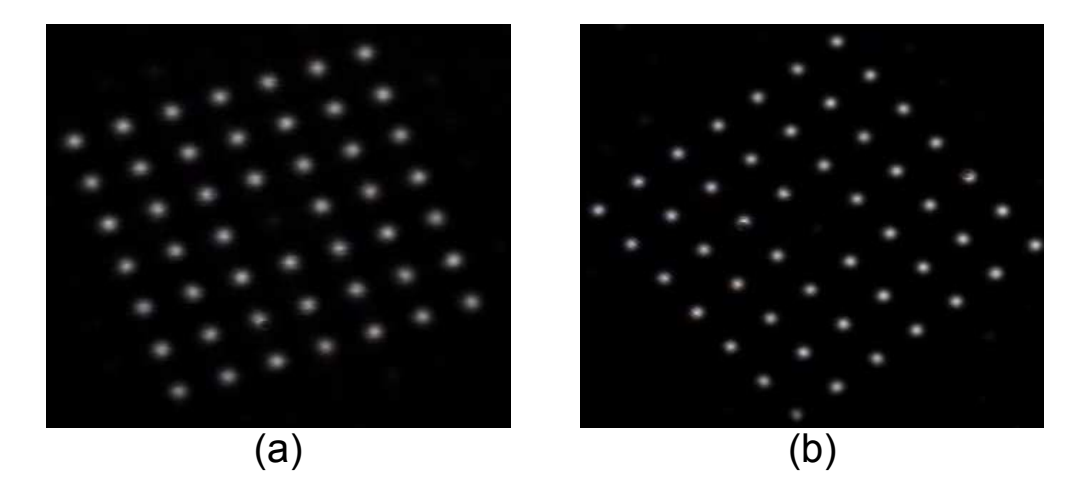


Figure 2.20 Beam quality of Gaussian beam arrays for different aspect ratio, with the HOLO-OR MS-049-Q-Y-A beam splitter $l=87\mu\mathrm{m}$, $\lambda=532\mathrm{nm}$, (a) $w_1=115\mu\mathrm{m}$, (b) $w_1=154\mu\mathrm{m}$.

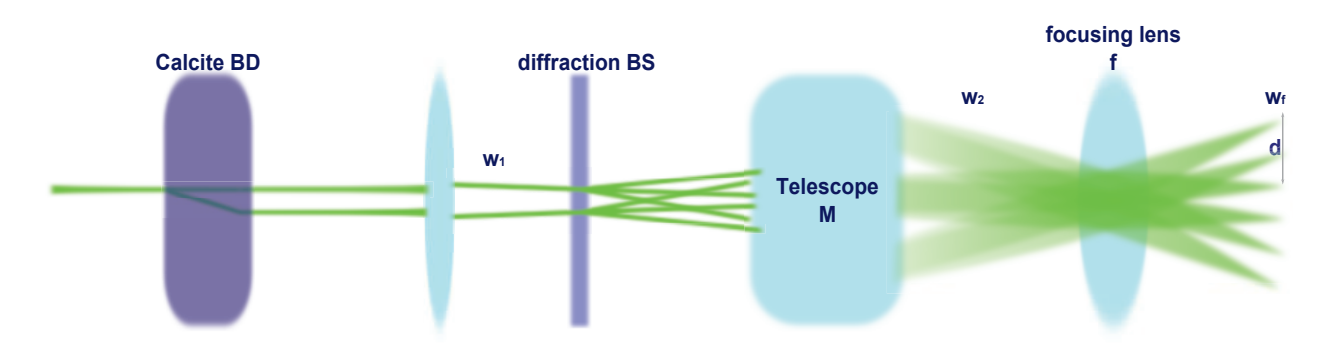


Figure 2.21 Schematic for creating a trap array with a calcite beam displacer and a diffraction beam splitter.

Chapter 3

Quasi-magic trapping of ground and Rydberg state atoms

The size of Rydberg atoms goes like n^2a_0 . Highly excited Rydberg atoms n 100 have sizes well on the order of our micron sized dipole trap. So the atom sees a light field with varying intensity instead of a single intensity. In the case of the blue detuned dark trap, the light shift of the Rydberg atom is not zero even when the atom stays still at the trap center. If there is intensity variation across the trap lattice, spatial variance of this energy shift could contribute to decoherence.

3.1 Ponderomotive Energy of Rydberg Atoms

The light shift of Rydberg atoms could be calculated by considering the ponderomotive energy of the electron.

The ponderomotive shift is the time averaged kinetic energy of a free electron in an oscillating electric field. For a field of the form $E\cos(\omega t)$, the ponderomotive energy is [Dutta 00]

$$U^{P} = \frac{e^{2}|E|^{2}}{4m_{e}\omega^{2}} \tag{3.1}$$

where -e and m_e are the electron charge and mass respectively.

Intensity of a light field is

$$I = \frac{cn\epsilon_0}{2}|E|^2 \tag{3.2}$$

where c and n are the speed of light and refractive index respectively.

So the ponderomotive energy of a free electron can be rewritten as

$$U^P = \frac{e^2}{2m_e c \epsilon_0 \omega^2} I \tag{3.3}$$

Then the Hamiltonian of a Rydberg atom in an oscillating electromagnetic field can be written as

$$\{H_F + U^P(\vec{R} + \vec{r})\}\psi(\vec{r}; \vec{R}) = E^R(\vec{R})\psi(\vec{r}; \vec{R}),$$
 (3.4)

where H_F is the atomic Hamiltonian free of external field, \vec{R} is the center of mass coordinate of the atom, and \vec{r} is the coordinate of the electron relative to the center of mass. Using the first order perturbation theory, and supposing there is no degeneracy involved, the energy shift of Rydberg atoms in state j is

$$\Delta E_j^R(\vec{R}) = \int d^3r U^P(\vec{R} + \vec{r}) |\psi_j^0(\vec{r}; \vec{R})|^2$$

$$= \frac{e^2}{2m_e c \epsilon_0 \omega^2} \int d^3r I(\vec{R} + \vec{r}) |\psi_j^0(\vec{r}; \vec{R})|^2$$
(3.5)

This expression is valid provided the ponderomotive potential varies over distance scales that are larger than the wavelength of the Rydberg electron. This is well satisfied for the potentials we consider. At n=150, the electron wavelength is about 50nm which is less than 10% of the wavelength of the light creating the trap.

In addition it is necessary that the ponderomotive shift is everywhere small compared to the energy spacing of Rydberg levels which scales as $1/n^3$, with n the principal quantum number. Even for the 150s state, which is the highest we consider below, the closest state is $146f_{7/2}$, which is 1.6 mK away. This is much larger than the trapping potentials of several hundred μK we are interested in.

3.2 Rydberg Wavefunction Calculation

The wavefunctions ψ_j^0 are calculated using a model pseudo potential method. The potential form adopted here is [Robicheaux 97]

$$V_l(r) = -\frac{Z_l(r)}{r} - \frac{\alpha_d}{2r^4} \left[1 - e^{-(r/r_c)^3} \right]^2 + \frac{l(l+1)}{2r^2}$$
(3.6)

where $Z_l(r) = 1 + (Z - 1)e^{-\alpha_l^{(1)}r} + \alpha_l^{(2)}re^{\alpha_l^{(3)}r}$. Z is the charge of the atomic nucleus, $\alpha_d = 15.81$, $r_c = 2.0$, and all the other parameters are listed in Table 3.1[communications with Francis Robicheaux][Johnson 83]. The radial part of the Schrodinger equation is

$$-\frac{\hbar^2}{2mr^2}\frac{\partial}{\partial r}\left(r^2\frac{\partial R(r)}{\partial r}\right) + \left(V(r) + \frac{l(l+1)\hbar^2}{2mr^2} - E\right)R(r) = 0$$

able 3.1 Tarameters for the Cs model potential (Equation 3						
	l	0	1	2	3	4+
	$\alpha_l^{(1)}$	3.49625	3.73801	3.45092	3.43592	3.43592
	$\alpha_l^{(2)}$	9.57499	9.56664	9.52285	9.54285	9.54285
	$\alpha_l^{(3)}$	1.41409	1.34016	1.58147	1.62147	1.62147

Table 3.1 Parameters for the Cs model potential (Equation 3.6).

Applying substitution $R(r)=\frac{u(r)}{r}$, and $V_{eff}(r)=V(r)+\frac{l(l+1)\hbar^2}{2mr^2}$, the equation becomes $\hbar^2 \ d^2u + (V_{eff}(r)-V_{eff}(r)) = 0$

$$-\frac{\hbar^2}{2m}\frac{d^2u}{dr^2} + (V_{eff}(r) - E)u = 0$$

Because the wavefunction varies very fast with r, we can smooth the variation by adopting the square root mesh $s=\sqrt{r}, r=s^2, dr=2sds, u(r)=v(s), \frac{du}{dr}=\frac{dv}{2sds}, \frac{d^2u}{dr^2}=\frac{d^2v}{4s^2ds^2}-\frac{1}{4s^3}\frac{dv}{ds}$.

The equation becomes (using atomic units)

$$-\frac{1}{8s^2}\frac{d^2v}{ds^2} + \frac{1}{8s^3}\frac{dv}{ds} + \left(V_{eff}(s^2) - E\right)v = 0$$
(3.7)

Using the inverse iteration method as in [Press 92] to find the eigenvalues E_k and eigenvectors \vec{v}_k after k iterations

$$\left(-\frac{1}{8s^2}\frac{d^2}{ds^2} + \frac{1}{8s^3}\frac{d}{ds} + V_{eff}(s^2)\right)_{discrete} \vec{v}_{k+1} - E_k \vec{v}_{k+1} = v_k \tag{3.8}$$

$$E_{k+1} = E_k + \frac{1}{\vec{v}_k \cdot \vec{v}_{k+1}} \tag{3.9}$$

Rewrite Eq 3.8 as

$$\frac{d^2v_{k+1}}{ds^2} - \frac{1}{s}\frac{dv_{k+1}}{ds} - 8s^2(V_{eff}(s^2) - E_k)v_{k+1} = -8s^2v_k$$
(3.10)

According to the appendix of [Robicheaux 96], in general the solution of a differential equation of the form

$$y''(x) - \frac{1}{x}y'(x) - A(x)y(x) = S(x)$$

can be propagated with a Numerov-type procedure

$$y(x+\Delta)\left(1-\frac{\Delta}{2x}\right)\left[1-\frac{\Delta^2}{12}A(x+\Delta)\right] - y(x)\left[2+\Delta^2A(x)\left(\frac{5}{6}-\frac{\Delta^2}{4x^2}\right)\right] + y(x-\Delta)\left(1+\frac{\Delta}{2x}\right)\left[1-\frac{\Delta^2}{12}A(x-\Delta)\right] = \Delta^2Q(x) + O(\Delta^5)$$

where

$$Q(x) = \frac{1}{12} \left(1 - \frac{\Delta}{2x} \right) S(x + \Delta) + \frac{1}{12} \left(1 + \frac{\Delta}{2x} \right) S(x - \Delta) + \left(\frac{5}{6} - \frac{\Delta^2}{4x^2} \right) S(x)$$

The initial guess of the eigenenergy E_0 is calculated from the quantum defect numbers [Lorenzen 84], and the initial eigenvector v_0 is an arbitrary non-zero vector. By solving Eq 3.10 iteratively, the results converge very fast to the real eigenvalues.

To verify our calculation of the wavefunctions, we reproduced the planewave photoionization cross sections for Rb listed in [Saffman 05]. The fine structure of Cs adds less than 0.1% correction to the ponderomotive energy shifts, so we ignore fine structure corrections in the following sections. Figure 3.1 shows some examples of the numerically calculated wavefunctions.

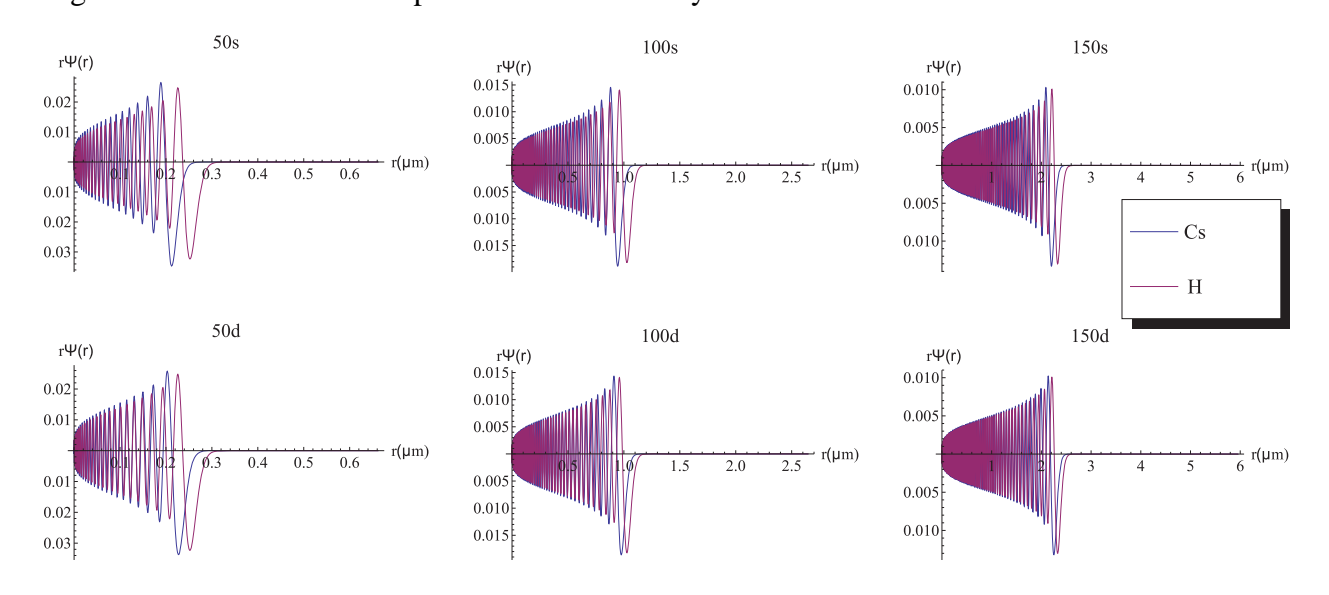


Figure 3.1 Wavefunctions of Cs Rydberg states calculated from the model potential method.

3.3 Ponderomotive Energy Shift in Bottle Beam Traps

Equation 3.5 is rewritten as

$$\Delta E_j^R(x, y, z) = \frac{e^2}{2m_e c\epsilon_0 \omega^2} \int r^2 dr \sin\theta d\theta d\phi I(x + r\sin\theta\cos\phi, y + r\sin\theta\sin\phi, z + r\cos\theta) |R(r)Y_{lm}(\theta, \phi)|^2$$
(3.11)

The 3D integral can be numerically calculated with the triplequad() function in MATLAB. To avoid oscillation problems, first the roots of the Hydrogen radial wavefunction are calculated,

 $x_{n,1}, x_{n,2}, ..., x_{n,i}, ...$, then the integrals are evaluated in each subinterval and added together in the end.

Figure 3.2 gives sample calculation results for ns Rydberg levels with n=100,125,150. We see that as n increases the effective trapping potential gets smaller and smaller. This is because the large electron wavefunction averages over the intensity distribution of the trap according to Eq. (3.5) which washes out the potential minimum. If the trap parameters are not chosen correctly, as is the case in Figure 3.2b), the trap could be repulsive for high n even though α_e is negative. Even when the trap is attractive for Rydberg states the ground to Rydberg trap shift for an atom at $\mathbf{R}=0$ is not negligible. This shift increases with n and is proportional to the light intensity. In an experiment with an array of traps this would imply that the Rydberg excitation energy would vary from site to site due to intensity variations across the array. To minimize this effect we seek trap parameters for which the $\mathbf{R}=0$ trap induced shift vanishes. We will refer to this in what follows as "quasi-magic" trapping. A quasi-magic trap will give an intensity independent excitation shift for atoms at the trap center (or for atoms in the motional ground state with slightly different compensation parameters) and only a small shift for sufficiently cold atoms.

3.4 Magic Condition for Zero Temperature Atoms

Inspection of Figure 2.1 shows that apart from wavelengths that are very close to the second resonance lines the magnitude of the ground state polarizability is larger than that of the Rydberg state. Conversely Figure 3.2 shows that the trapping potential at $\mathbf{R}=0$ is larger for Rydberg states than for ground states. This implies that we can balance the $\mathbf{R}=\mathbf{0}$ trap shifts by adding a constant background intensity that will shift the ground state potentials more than the Rydberg state potentials. With the correct background intensity $I_{\rm m}$ the differential shift will vanish. This is the quasi-magic trapping condition. Note that if we were to use the wavelengths in Figure 2.1 where the ground and Rydberg polarizabilities are equal ($\sim 510 \mathrm{nm}$), to compensate the ponderomotive potential shift, we would have to add a relatively large background intensity. At $\lambda=780~\mathrm{nm}$ the ground state polarizability α is about $5.4\times$ larger than that of the Rydberg state α_e which reduces the power requirement for the background beam by this factor. It is possible to work even

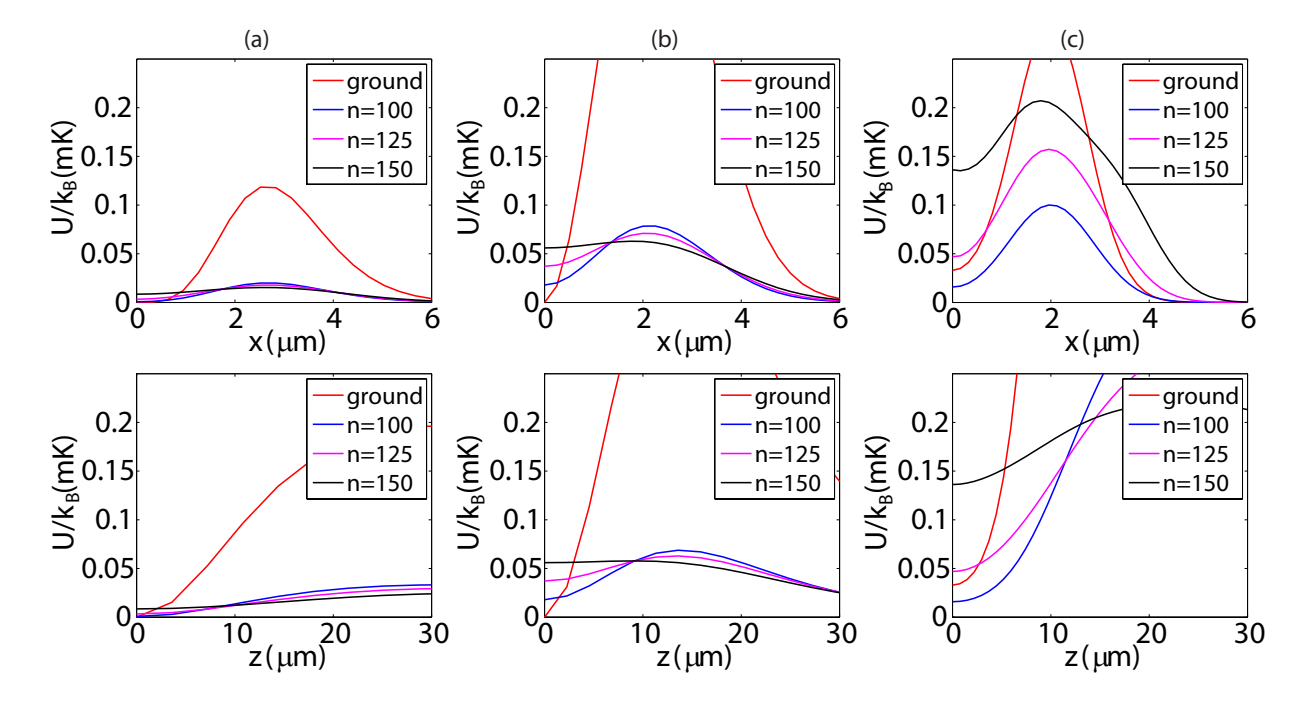


Figure 3.2 (color online) Potential energy of Cs ground and ns Rydberg states in a) Gaussian interference BoB, b) vortex BoB, and c) Gaussian lattice BoB. Trap parameters are: power $P=50~\mathrm{mW}$ for a) Gaussian interference BoB $w_1=2~\mu\mathrm{m},\,w_2=3.78~\mu\mathrm{m}$, b) crossed vortex BoB $w=3~\mu\mathrm{m},\,\theta=8.6^o$, and c) Gaussian lattice trap $w=1.5~\mu\mathrm{m},\,d=4~\mu\mathrm{m}$.

closer to the first resonance line where α/α_e is even larger, but decoherence rates associated with photon scattering and differential hyperfine shifts[Saffman 05, Kuhr 05] increase correspondingly. In addition, it is relatively easy to get a high power laser source of 780 nm (frequency doubled from an 1560 nm laser). We have therefore chosen 780 nm for Cs as a viable working wavelength.

Using the ground state light shift

$$\Delta U_g = -\frac{\alpha_g}{2\epsilon_0 c} [I_{\text{BoB}}(\vec{R}) + I_{\text{m}}(\vec{R})],$$

and the Rydberg state shift

$$\Delta U_R = \frac{e^2}{2\epsilon_0 c m_e \omega^2} \int d^3 r [I_{\text{BoB}}(\vec{R} + \vec{r}) + I_{\text{m}}(\vec{R} + \vec{r})] |\psi_j^0(\vec{r}; \vec{R})|^2$$

the quasi-magic condition is simply $\Delta U_g = \Delta U_R$. Figure 3.3 shows an example of such a magic condition for the crossed vortex BoB by adding a planewave compensation field.

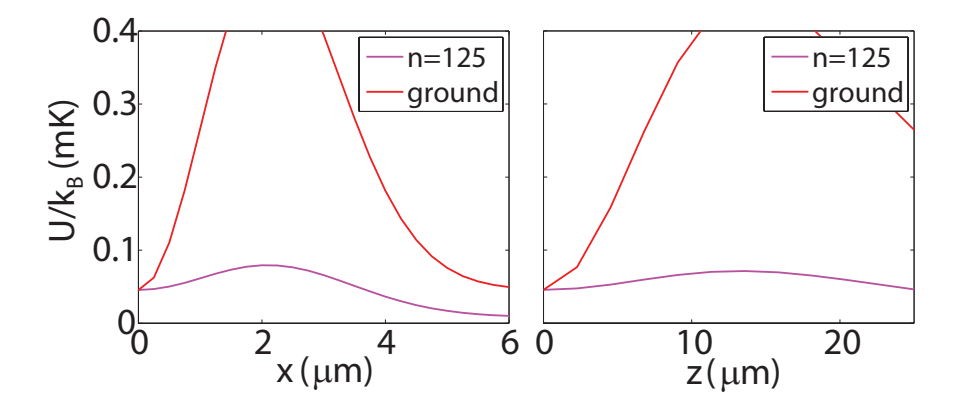


Figure 3.3 (color online) Energy shift compensation for the crossed vortex BoB with a planewave of intensity $I_m = 128 \ \mu \text{W}/\mu \text{m}^2$, $w = 3 \ \mu \text{m}$, $\theta = 8.6^{\circ}$, and $P = 50 \ \text{mW}$.

Although the additional power required for matching is small for a single site, the additional light requirement becomes substantial if we consider a 100×100 or $1000 \times 1000 \ \mu m^2$ array. The Gaussian lattice design presents an interesting alternative since the light intensity is naturally not zero at the trap center. The $\mathbf{R}=0$ intensity changes as we vary the waist size or separation of the beams, and by judicious choice of parameters we can achieve the matching condition without adding any additional plane wave. Note that the compensating intensity is in this case not uniform but is spatially varying. Figure 3.4 shows such a self magic condition for n=125. Figure 3.5 and Table 3.2 list the self magic conditions for different n's.

Table 3.2 Self-magic conditions for selected n states in a Gaussian lattice trap with $\lambda = 780~\mathrm{nm}$,

$d=4~\mu\mathrm{m}.$							
n	100 125 150						
$w_0(\mu\mathrm{m})$	1.3148	1.5575	1.73				

For a ground state atom with a low temperature, we can estimate the average trap induced shift between ground and Rydberg states by $\langle dU \rangle = \frac{1}{2} \sum_{i=x,y,z} dU_{ii}(0,0,0) \langle r_i^2 \rangle$, where the mean square position of the atom found from the Virial theorem is $\langle r_i^2 \rangle = \frac{k_B T}{2\partial_{ii} U_g}$, $dU_{ii} = \partial_{ii}(U_R - U_g)$ and U_g, U_R are the ground and Rydberg state trapping potentials. Figure 3.6 shows that the transition shift decreases nearly linearly with decreasing atom temperature. This shift would be below 0.2 MHz for an atom temperature of 10 μ K which is readily achieved using

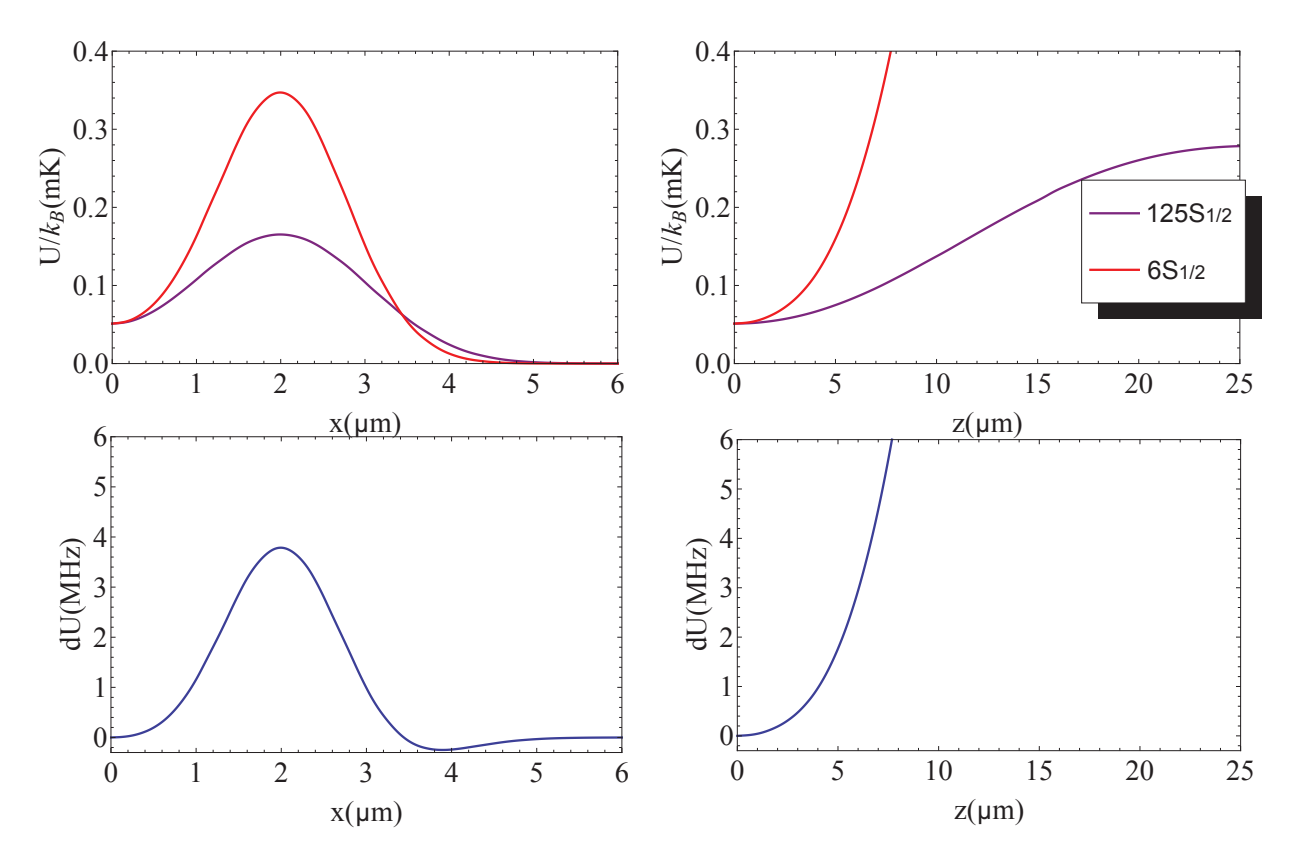


Figure 3.4 (color online) Trapping potential (top row) and shift difference (bottom row) between Cs 6s and 125s for a self-magic Gaussian lattice trap with $\lambda=780$ nm, d=4 μ m, w=1.56 μ m, and P=50 mW.

polarization gradient cooling of Cs. The trapping depth of the Gaussian lattice BBT with the self-magic condition is $304~\mu K$. In comparison, for the vortex BBT shown in Figure 3.2, with a trapping depth of $225\mu K$, the differential shift of 125s state is about 0.8 MHz for an atom temperature of 0K.

3.5 Photoionization Rate of Rydberg Atoms

The photoionization rate of an atom is proportional to the light intensity as

$$W = \sigma I/h\nu$$
.

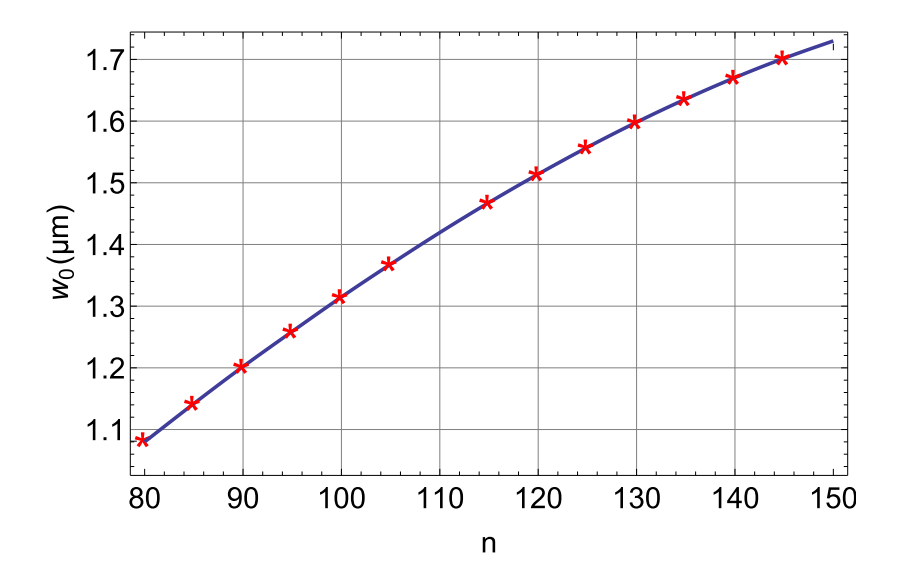


Figure 3.5 Self-magic conditions for different nS states in a Gaussian lattice trap with $\lambda=780$ nm, $d=4~\mu{\rm m}$.

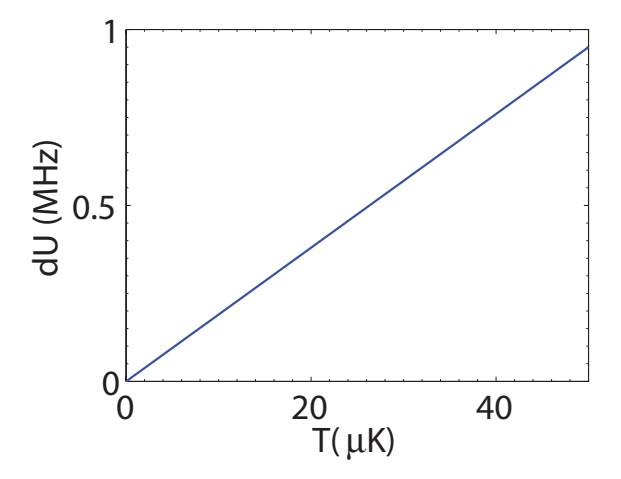


Figure 3.6 Average transition shift between ground and 125s states of Cs in Gaussian lattice trap with $d=4~\mu\mathrm{m}$, $w=1.57~\mu\mathrm{m}$, $P=50~\mathrm{mW}$, and $U_{\mathrm{trap}}=k_B\times300~\mu\mathrm{K}$.

For a uniform radiation field, the cross section can be calculated by [Saffman 05]

$$\sigma_{\omega} = \frac{4\pi^2 \omega}{3c(2L+1)} \sum_{L'=L\pm 1} L_{max} |\langle E_e, L'|r|nL\rangle|^2, \tag{3.12}$$

where E_e is the energy of the free electronic state.

3.5.1 Photoionization rate of Bottle Beam/Gaussian lattice

In a more general case, the cross section can be expressed as [Gallagher 94]

$$\sigma = 2\pi^2 \frac{\hbar^2}{m_e^2 c^2 \alpha} f_{if},$$

where α is the fine structure constant. The oscillator strength

$$f_{if} = \frac{2}{\hbar m\omega} \frac{1}{2l_i + 1} \sum_{m_i} \sum_{l_f, m_f} |\langle f | \vec{A} \cdot \vec{p} | i \rangle|^2$$
(3.13)

where initial state $|i\rangle=|n_i,l_i,m_i\rangle$ is a Rydberg state with principle quantum number n_i , final state $|f\rangle=|E_f,l_f,m_f\rangle$ is a continuum state with energy $E_f=E_{photon}+E_{Ryd}$, \vec{A} is the operator of magnetic vector potential, and \vec{p} is the momentum operator. The magnitude of A is normalized to a unit peak intensity. Free electrons do not absorb photons. So even though $kr\sim kn^2a_0\gg 1$ is large, we can ignore high terms of r in calculating the matrix element. The quadrupole term is included in case that the dipole term is vanishing at the center of a dark trap.

For a planewave field polarized in the x direction $\vec{A}=e^{i\vec{k}\cdot\vec{r}}\hat{x}$, Equation 3.13 can be approximated by

$$f_{if} \approx \frac{2\hbar}{m\omega} \frac{1}{2l_i + 1} \sum_{m_i} \sum_{l_f, m_f} |\langle f | (p_x + ik_x x p_x + ik_y y p_x + ik_z z p_x | i \rangle|^2$$

$$(3.14)$$

We can use the following relations to simplify the equation[Bethe 57].

$$\vec{p} = \frac{i\hbar}{m}[H, \vec{r}]$$

$$xp_x = \frac{im}{2\hbar}(Hxx - xxH) + \frac{1}{2}i\hbar$$

$$yp_x = \frac{1}{2}(p_xy + xp_y) + \frac{1}{2}(yp_x - xp_y) = \frac{im}{2\hbar}(Hxy - xyH) - \frac{1}{2}l_z$$

$$zp_x = \frac{1}{2}(p_xz + xp_z) + \frac{1}{2}(zp_x - xp_z) = \frac{im}{2\hbar}(Hxz - xzH) + \frac{1}{2}l_y.$$
(3.15)

If we ignore the magnetic dipole term, Equation 3.14 becomes

$$f_{if} \approx \frac{2m\omega}{\hbar} \frac{1}{2l_i + 1} \sum_{m_i} \sum_{l_f, m_f} |\langle f | (x + \frac{ik_x}{2}x^2 + \frac{ik_y}{2}xy + \frac{ik_z}{2}xz) | i \rangle|^2.$$

For a complex field like the Gaussian lattice dipole field, we can decompose it into planewaves

$$A(\vec{r}) = \frac{1}{(2\pi)^3} \int d^3 \vec{k} \, g_{\vec{k}} e^{i\vec{k}\cdot\vec{r}}$$

$$g_{\vec{k}} = \int d^3 \vec{r} A(\vec{r}) e^{-i\vec{k}\cdot\vec{r}}.$$

The oscillator strength can then be written as

$$f_{if} \approx \frac{2m\omega}{\hbar} \frac{1}{2l_i + 1} \sum_{m_i} \sum_{l_f, m_f} \left| \frac{1}{(2\pi)^3} \int d^3 \vec{k} \, g_{\vec{k}} \left(\langle x \rangle + \frac{ik_x}{2} \langle xx \rangle + \frac{ik_y}{2} \langle xy \rangle + \frac{ik_z}{2} \langle xz \rangle \right) \right|^2.$$

Figure 3.7 shows the photoionization rate for a 125s state Cs atom in a Gaussian lattice trap which satisfies the self magic condition. In the Fourier expansion, the continuous \vec{k} is discretized to a $30 \times 30 \times 30$ grid, and the fidelity of the discretization can be verified by the reconstruction of the light field in Figure 3.8. The quadrupole term is making less than 3% correction to the final result in the plot due to the non-zero light intensity at the trap center. The wavefunctions are calculated with the same method as in Section 3.2. The radial part of the continuum state is normalized to

$$\phi_{E_f,l_f} \to \sqrt{\frac{2m}{\pi \hbar^2 k_e}} \sin(k_e r + \delta), \text{ as } r \to \infty.$$

where k_e is the wavenumber of the free electron.

For comparison a Cs atom in a 1064 nm far off resonance trap created by a Gaussian beam with the same trapping depth 300 μ K, $I_0 = 5.8 \times 10^8$ W/m², would have a photoionization rate of about 2.4 s⁻¹. So if the atom stays at the center of the Gaussian lattice trap, the photoionization rate is almost an order of magnitude smaller than that in an equal depth red detuned trap.

3.5.2 Blackbody Radiation Photoionization

While the Stark shift of blackbody radiation(BBR) adds a uniform offset to the Rydberg frequency, the photoionization induced by BBR could be large due to the small binding energy of

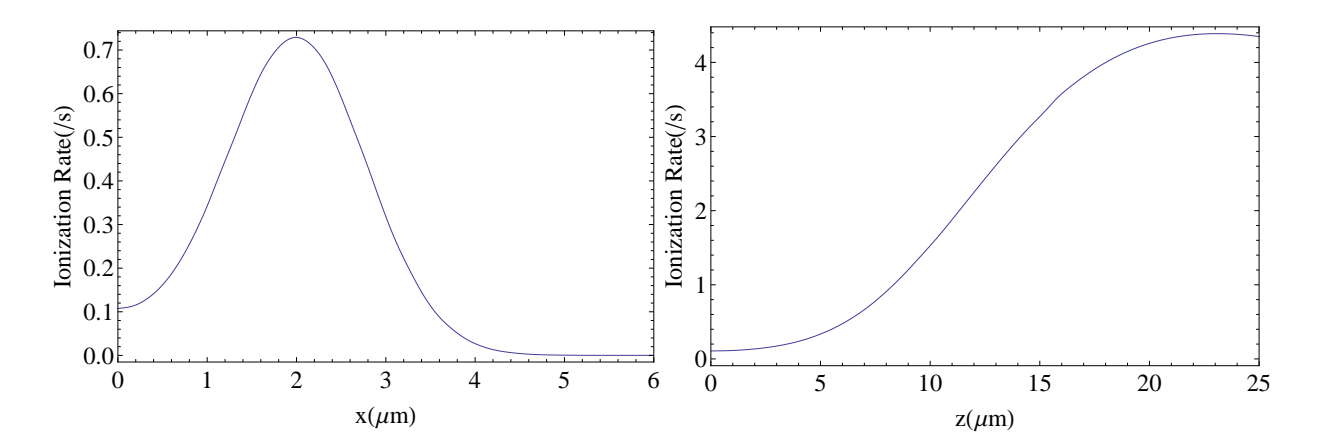


Figure 3.7 Photoionization rate for 125s Cs in a 780nm self-magic Gaussian lattice dipole trap, $w_0=1.56~\mu\mathrm{m},\,d=4~\mu\mathrm{m},\,P=50~\mathrm{mW},\,\mathrm{and}~U_{\mathrm{trap}}=k_B\times300~\mu\mathrm{K}.$

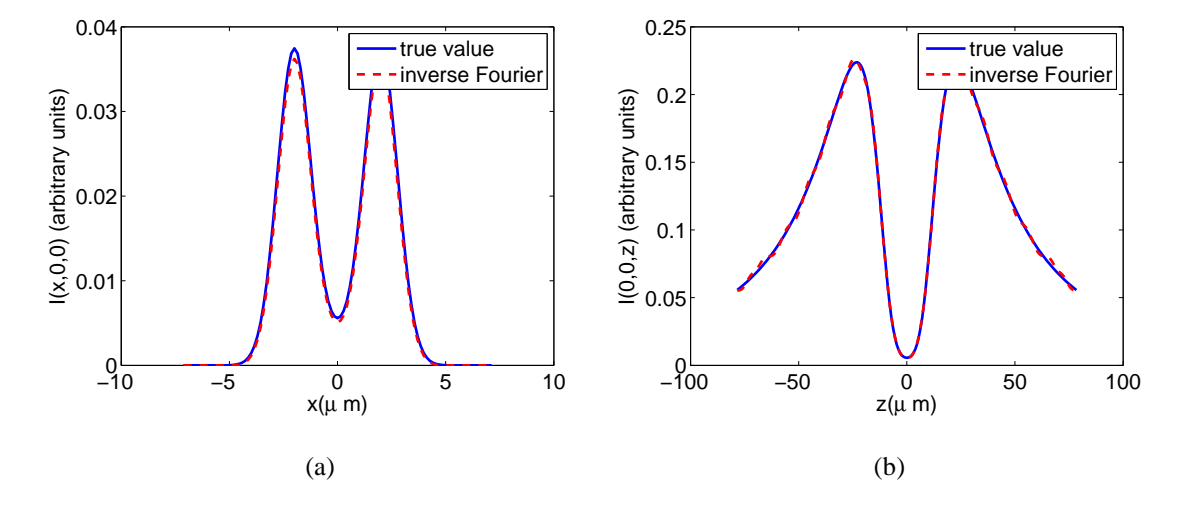


Figure 3.8 (color online) Reconstructed field intensity by inverse Fourier transformation from discretized Fourier components for a Gaussian lattice dipole trap, $\lambda=780 \,\mathrm{nm}, w_0=1.56 \,\mu\mathrm{m},$ $d=4 \,\mu\mathrm{m}.$

Rydberg atoms. Besides directly photoionizing the Rydberg atoms, BBR could also cause the Rydberg level to redistribute before the ionization, which will be calculated for the decay of Rydberg states in Chapter 7. So for now we are only considering the direct photoionization.

The BBR photoionization rate can be calculated by

$$W_{BBR} = c \int_{\nu_0}^{\infty} \rho(\nu, T) \sigma(\nu) d\nu$$
 (3.16)

where ν_0 is the threshold frequency, $\sigma(\nu)$ is the photoionization cross section at frequency ν calculated by Equation 3.12. $\rho(\nu)$ is the planck distribution of photon number density $\rho(\nu,T)=\frac{8\pi\nu^2}{c^3}\frac{1}{e^{h\nu/k_BT}-1}$. The results are shown in Figure 3.9. The integration is done numerically from threshold frequency to $\nu_{max}=1.5T\times58.8\mathrm{GHz/K}$, with 100 evenly spaced intervals. We can conclude that the photoionization rate $W_{trap}\ll W_{BBR}\ll \Gamma_R$, where Γ_R is the radiative decay time of Rydberg states. There is no need to worry about the photoionization induced by trap light.

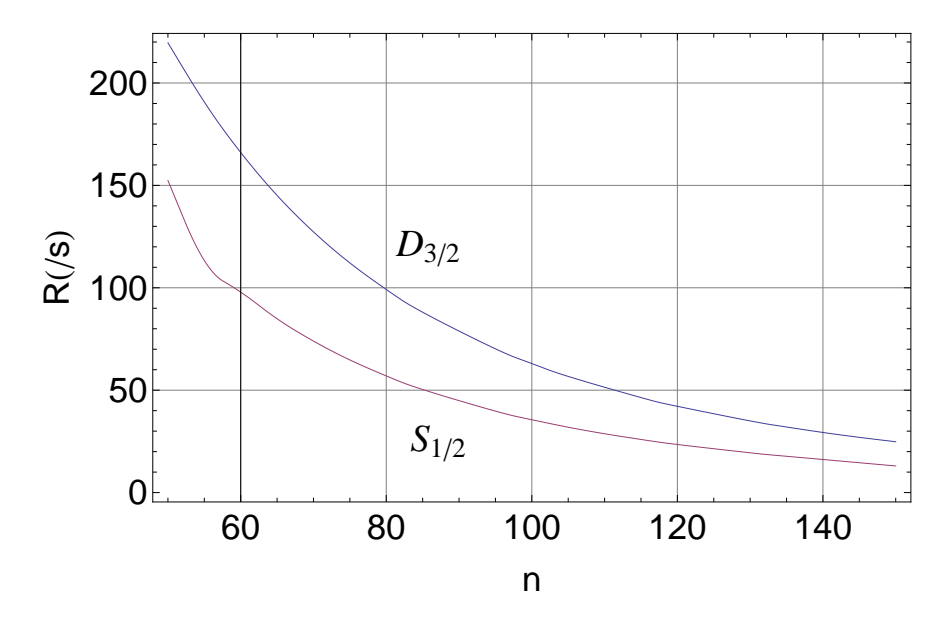


Figure 3.9 Blackbody radiation induced photoionization rate for Cs Rydberg states.

Chapter 4

Experimental Setup

4.1 Magneto Optical Trap

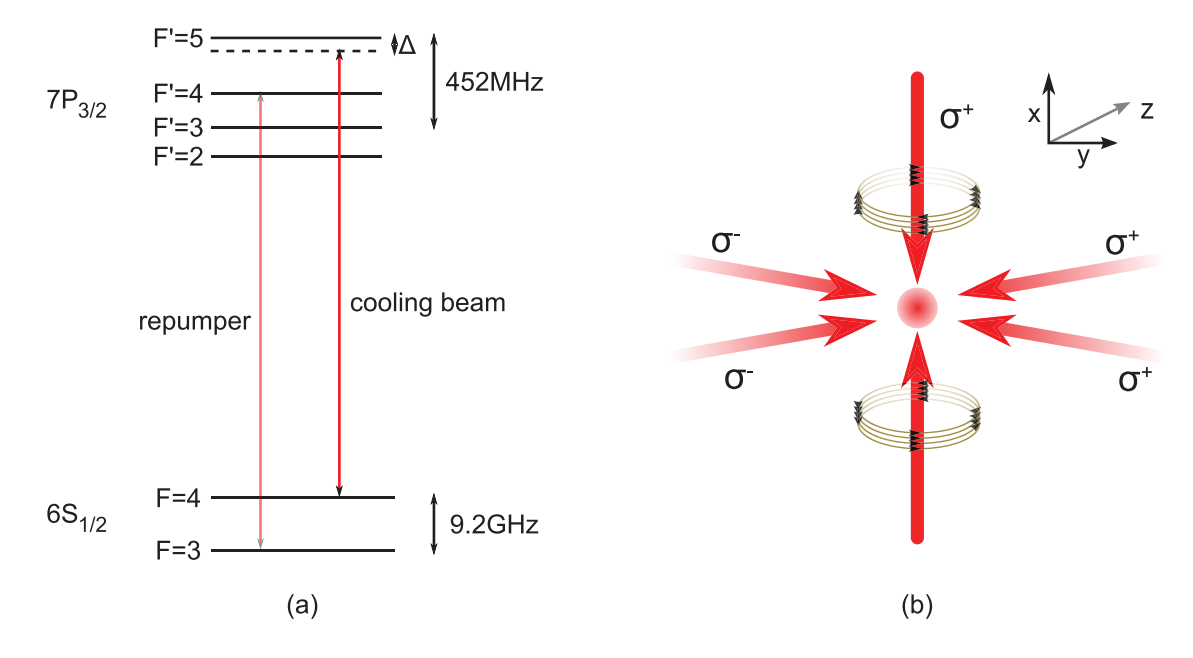


Figure 4.1 (a)D2 line transition of Cesium and (b) setup of the magneto optical trap (MOT).

Figure 4.1 shows the setup of the Cs MOT. The cooling laser is locked to the D2 $F=4 \rightarrow F'=3$ and $F=4 \rightarrow F'=5$ cross-over line, which is -226MHz from the $F4 \rightarrow F'=5$ resonance. We then use a double pass AOM to shift the frequency closer to the cycling $F=4 \rightarrow F'=5$ transition resonance. The double pass AOM path is after the cat-eye configuration as in [Donley 05]. During the MOT loading phase, the cooling laser is detuning by -10MHz, by setting the AOM to 108MHz. During the polarization gradient cooling (PGC) phase, the cooling laser is detuning by -30MHz or

-50MHz, by setting the AOM to 98MHz or 88 MHz.

The MOT is in a rectangular vacuum glass cell. The cell is made of 3mm thick pyrex glass. The vertical beam has a beam waist about 2.3mm, with 1.5mW power during MOT loading phase. The two horizontal beams have beam waists about 1.7mm with 0.7mW power in each beam during MOT loading phase. So the total intensity is about $I_t = 24 \text{mW/cm}^2$. Using the isotropic Cesium D2 $F = 4 \rightarrow F' = 5$ saturation intensity $I_{sat} = 2.7 \text{mW/cm}^2$, the saturation parameter of the MOT is about $I_t/I_s = 8.9$. The field gradient is about 20 G/cm in the vertical direction.

4.1.1 MOT Temperature

We use the free expansion method to measure the MOT temperature. The procedure is as follows: both the magnetic field gradient and laser beams are turned off for a varying amount of time t, and the atom cloud freely expands. The beams are then turned back on to take a snapshot of the atom cloud (exposure time 1ms). The picture is fitted with a Gaussian profile. The assumption is that the initial atom distribution follows the Gaussian shape of the trapping beams. The cloud waist expands with time following the equation [Williams 09]

$$w_{x,y}(t) = w_0 \sqrt{1 + \frac{4k_B T_{x,y}}{m w_0^2} t^2}$$
(4.1)

The pictures are taken with a Andor Luca camera, whose pixel size is $8\mu m$. The magnification of the imaging system(AC254-100,LA1484 f300, Edmund NT49-386 f300 achromat, Figure 4.2) is calibrated with the ASAF chart to be 3.73.

The Doppler temperature of Cs is $T_D = 125 \mu \text{K}$. Then atom cloud temperature after the loading phase ($\Delta = -10 \text{MHz}$) is about $157 \mu \text{K}$. Then we use PGC to cool the atoms to sub-Doppler temperature [Dalibard 89]. Although PGC with a high magnetic field gradient is possible, low temperatures are only possible if the atom density is low[Drewsen 94]. We need a high atom density to load the bottle, so we use the optical molasses without the gradient field to do the PGC cooling[Jersblad 00]. The timing sequence is as follows:

The MOT is loaded for about 1s with -10 MHz detuning. Then the magnetic field gradient is

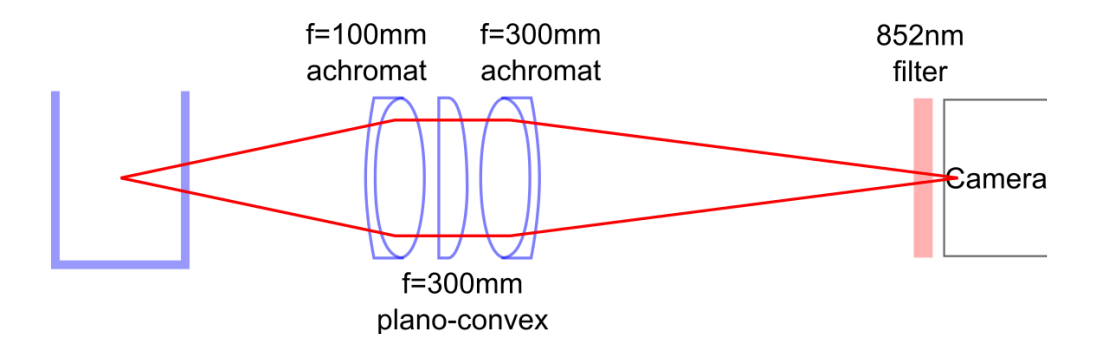


Figure 4.2 MOT imaging optics.

turned off, the laser detuning is switched to -30MHz, and laser intensity is decreased to do a first stage PGC for 5ms. After this phase, the atom temperature is about $30\mu K$.

If needed, a second stage PGC could be applied with the detuning -50MHz and lower intensity. We can get atom cloud temperature as low as $4\mu\mathrm{K}$ after the two-stage PGC.

4.1.2 Loading Time and Atom Density Measurements

Figure 4.3 shows a measurement of the MOT loading time at a pressure about 1×10^{-9} Torr. The measured loading time is 1.7s. Usually we use a loading time of 700ms in our single atom experiment. It means the atom density is 66% of the peak density we can get, which is dense enough to give us 50% loading probability and a 1s cycle time.

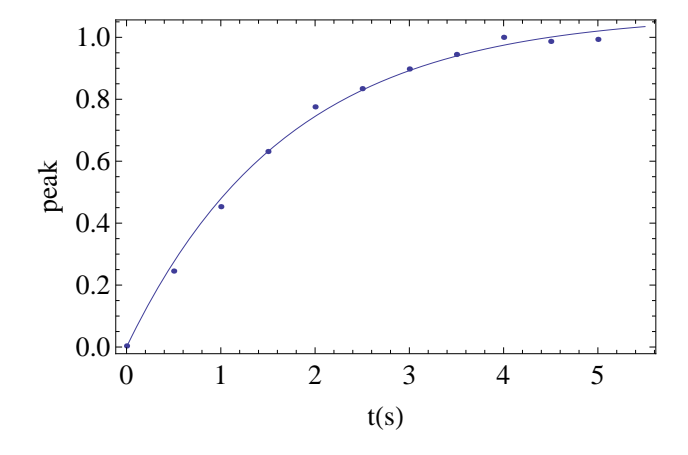


Figure 4.3 MOT loading time measurement, $\tau = 1.7$ s.

Table 4.1 Calibration of Andor Luca camera (camera quantum efficiency @852nm taken into account).

gain	1	10	50	100	200
count per 852nm photon	0.177	1.49	6.40	7.94	10.4

To estimate the atomic density of the MOT, the counts to photon number conversion of the Luca camera is calibrated with a femto-watt photodetector. Results are shown in Tab. 4.1. Transmission of the pyrex vacuum cell glass is measured to be T(852nm)=0.92, T(532nm)=0.87. Using these calibrations, we estimate the atom density of the MOT after the PGC is about $1\times 10^9\sim 1\times 10^{10}/{\rm cm}^3$. If we approximate the trap volume by $\frac{4}{3}\pi r_t^2 r_z$, where the transverse radius $r_t=2\mu{\rm m}$, and axial radius $r_z=10\mu{\rm m}$, $0.17\sim 1.7$ atoms can be captured in the trap on average.

4.2 Optical Setup of the BoB Module

Figure 4.4 shows the layout of the crossed vortex bottle beam setup. The parts in the green dashed box are the optics to create the crossed vortex bottle beam trap. The parts in the red box are the optics of atom detection using a single photon counting module. The parts in the blue box are the optics for coupling the ground state Raman 457nm or Rydberg 459nm and 1038nm laser beams. All these optics are integrated to a single cage system, and mounted on a 3D translational stage. The final waist size of the 457/459nm beam is about 5.9μ m, and the waist size of the 1038nm Rydberg beam is about 2.8μ m.

To align the different beams, we first move the cage away from the vacuum cell, and look at the beams magnified by a microscope on a Sony camera. To align the atom detection module to the bottle trap, an 852nm beam is sent backward through the photon collecting 1550nm single mode fiber. Then the focus of this beam along with the focal spots of the 457/459nm and the 1038nm beams is adjusted to overlap with the center of the bottle. To overlap the bottle trap with the atomic cloud, we also make use of the backward 852nm light from the photon collecting fiber. First, the

position of the MOT is pinned down on the Andor Luca camera screen. Then, the 852nm alignment beam is turned on, and the MOT beams are turned off, the Luca camera is exposed for about 1s to look at the alignment beam fluorescence. The 3D stage of the cage system is then adjusted to move the focus of the 852nm beam to where the MOT is, and this way the bottle trap is aligned with MOT on the viewing plane of the camera. To overlap the bottle with the MOT on the third direction, the MOT is turned back on and we use the alignment beam to blow away the MOT. The fluorescence and blowaway steps are repeated until there is a good overlap.

4.3 Filtering Test

The 532nm dipole trap light is very strong with a power of up to 0.5W at the atom. The signal from a single atom is on the order of 100 photons. Although the trap light and the single atom fluorescence are going in opposite directions, there could still be strong background from the trap light. So special care is needed to filter out the green light from the Cs atom fluorescence light. Table 4.2 lists several filter sets we have tested. The tests were done in the optical setup of Figure 4.4 with the tested filter set as the 852nm filter in the diagram. The photon counter used in the experiments was the SPCM-AQR-13 single photon counter module, and the photon collection fiber was a multimode fiber instead of the 1550nm SM shown in the diagram.

In Table 4.2, IF stands for the interference filter (part number Semrock FF01-832/37-25), the

Table 4.2 Performance of different filter combinations to filter out background light from the 532nm light in the atom detection path with 0.2W of 532nm light out of Verdi.

filter set	no filter	1 IF	2 IFs	1 CG	1 CG and 1 IF	2 IFs and a prism
photon count frequency(kHz)	500	10	4	65	5	3

transmission of which at 532nm is measured to be $T(532\mathrm{nm})2.5 \times 10^{-6}$; CG stands for the color glass filter (part number Newport FSR-RG610), the transmission of which at 532nm is measured to be $T(532\mathrm{nm})3 \times 10^{-4}$. If the background light due to the trap light is purely 532nm light, we would expect the detected photon numbers to scale as $1:T:T^2$. But the testing results show

that after adding the first filter, the background falls by a factor of 50, and additional filtering has a small effect on the final photon counts. This suggests that there may be long wavelength light as a result of turning on the green light.

The Verdi is pumped by 808nm light, so there could be some 852nm light mixed in the green light. So we added a Semrock FF01-510/84-25 interference filter in front of the green fiber to filter out any 852nm light from the Verdi. We also tried using a prism in front of the green fiber to spectrally separate any 852nm light from the green. These had little effect on the background. So one explanation could be that 532nm light induces fluorescence in the 852nm range from the vacuum cell or pollutants inside the vacuum.

4.4 Optical Pumping

An 894nm Vescent laser is used to optically pump the Cs atom to the m=0 clock state. The transition involved is shown in Figure 4.5. The 894nm laser is tuned on resonance with the $F=4 \rightarrow F'=4$ D1 transition of Cs, and π polarized. In a bias field perpendicular to the 894nm beam, combined with the repumper beam, the atoms are pumped to the $|F=4,m_F=0\rangle$ ground clock state.

4.4.1 Bias Magnetic Field

The two bias B field coils have a diameter of 70mm, and 13 turns each. They are separated by 85mm. With 1A of current, the calculated bias field would be 1.2 Gauss. In our experiments the bias field is typically from 0.5 to 0.7 Gauss (0.75V to 1.00V controlling voltage).

4.5 State Detection

The ground state hyperfine levels are detected by an 852nm beam in resonant with the $|6S_{1/2}, F = 4\rangle \rightarrow |6P_{3/2}, F = 5\rangle$ transition. The 852nm will blow away the atoms in the $|6S_{1/2}, F = 4\rangle$ from the trap without affecting the atoms in the $|6S_{1/2}, F = 3\rangle$ state. The waist size of the blowaway

beam is 0.5mm and the beam power is 0.3mW. It can blow away the $|F=4\rangle$ within $5\mu s$. If the numerical aperture of the asphere is large enough, the states can also be detected non-destructively by collecting scattered photons[Gibbons 11, Fuhrmanek 11], and measuring the absorption and phase shift of a weak strongly focused probe beam (see Appendix B for details).

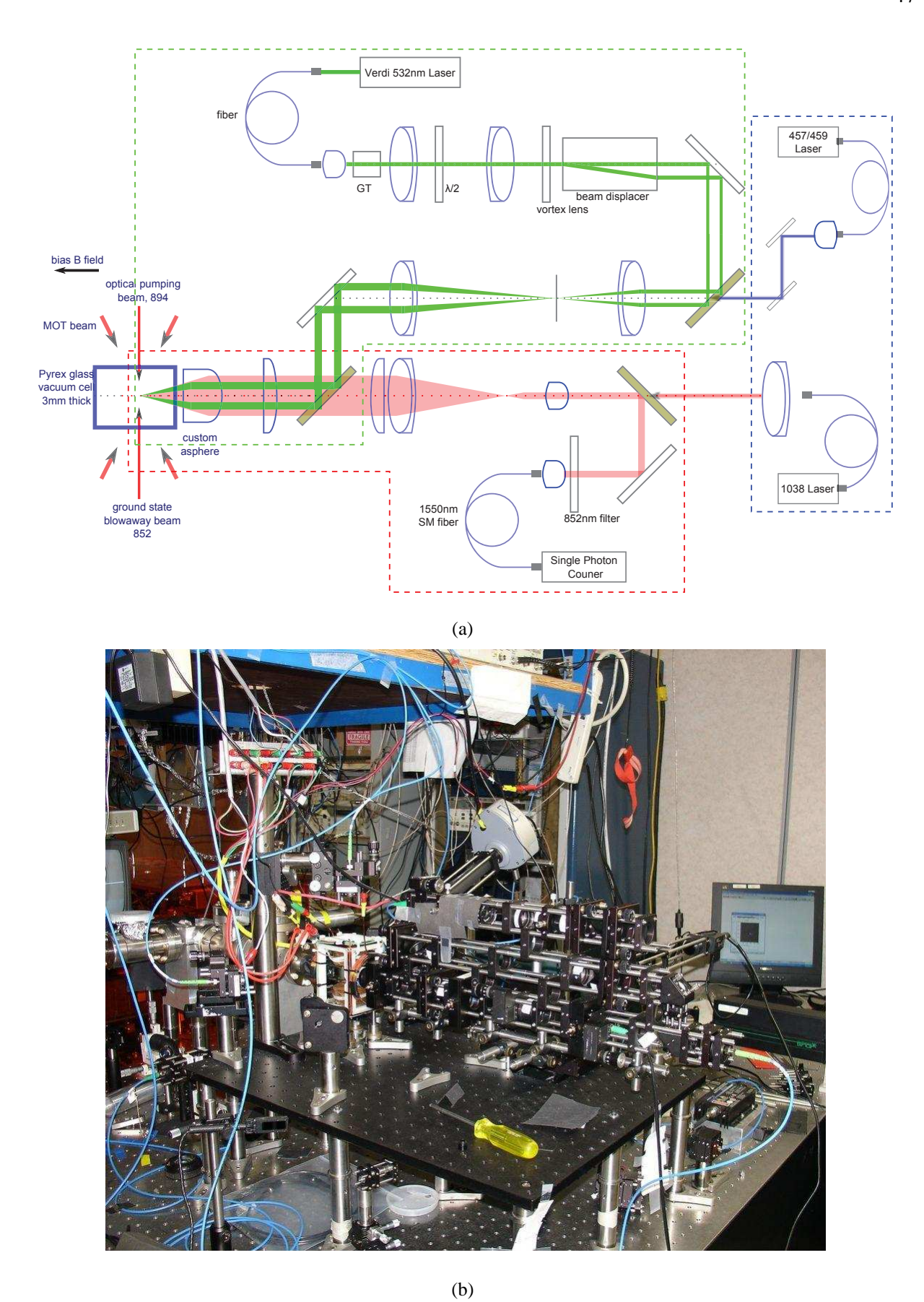


Figure 4.4 (a)Optical layout and (b)picture of the green crossed vortex bottle beam setup

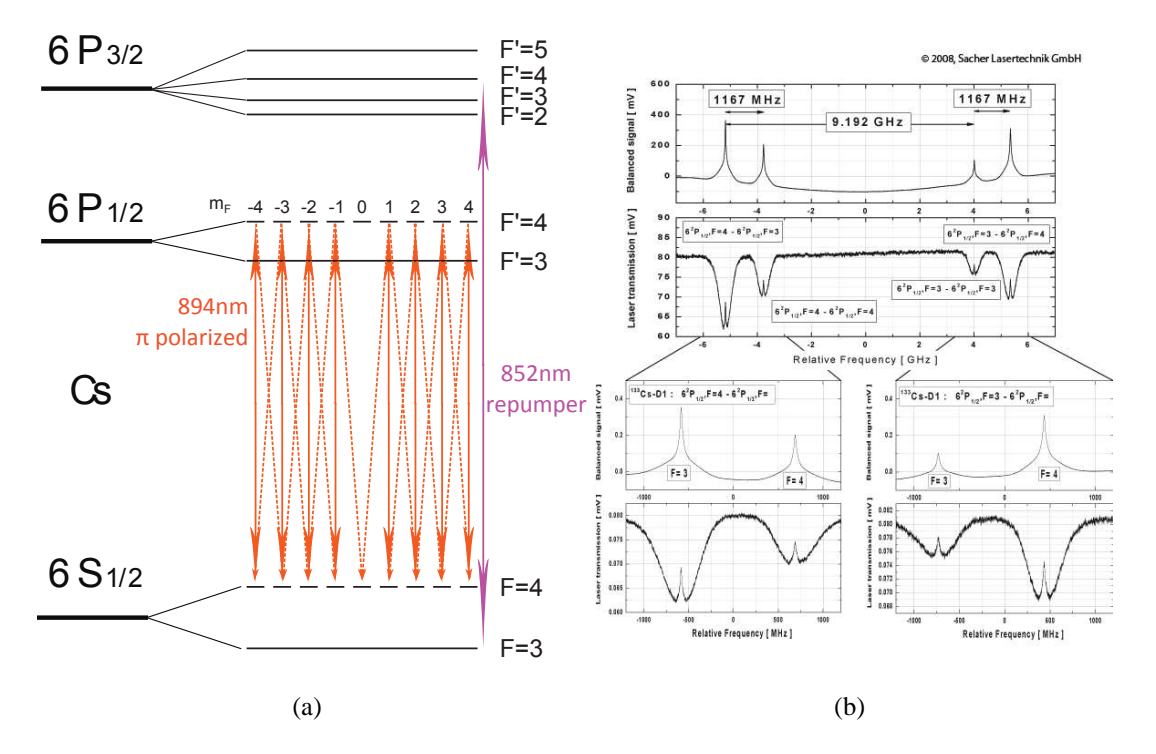


Figure 4.5 (a)Cesium transition line and (b) saturated absorption spectrum [Sacher] of the 894nm optical pumping laser for the clock state.

Chapter 5

Single Atom Loading

5.1 Timing Sequence

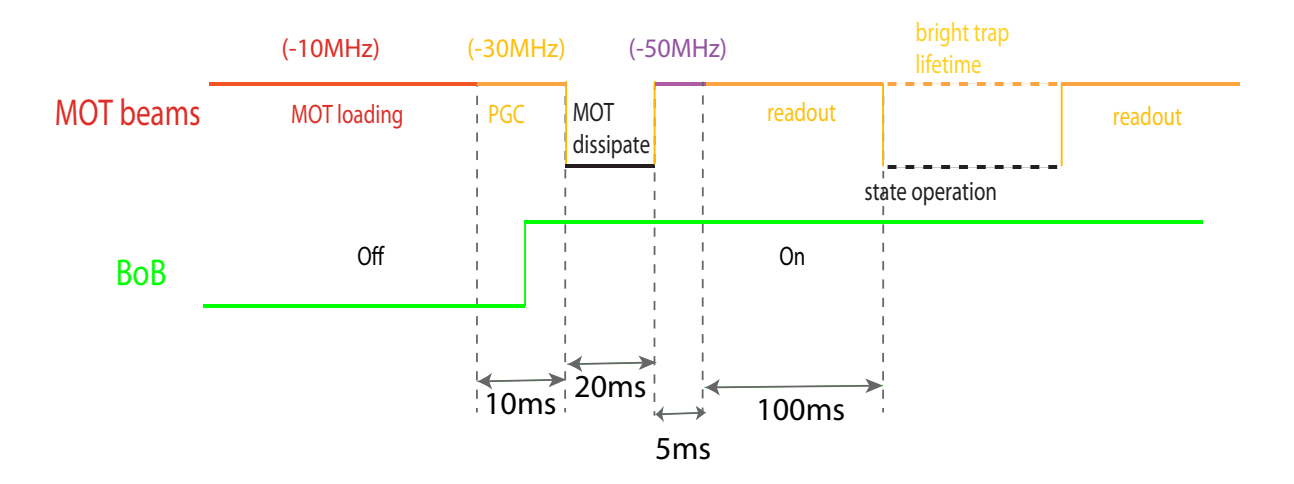


Figure 5.1 Timing sequence for single atom experiments in a vortex BoB.

Figure 5.1 is the timing sequence for a typical single atom loading experiment. For each cycle, the MOT is loaded for 0.7 to 1 seconds with a MOT beam detuning of -10MHz. Then the MOT gradient magnetic field is turned off, and the cooling laser frequency is switched to a larger detuning and smaller intensity to do polarization gradient cooling (PGC). The lager the detuning, the colder the atoms, but the lower the atom density. We typically use a detuning of 30MHz which cools the atom down to about 20 μ K with a moderate atom density for BoB loading. After 5ms of PGC, the BoB beam is turned on, and overlaps with the MOT for 20ms to capture the atom. If we leave the BoB always on, the atom would need to climb over a potential barrier to get into the trap, which lowers the loading probability. Then the MOT beams are switched off for 20ms for the

residual MOT to dissipate. After this, the photon counter is turned on for the first loading readout, with the PGC cooling beams and the repumper. Experimental pulses, for example state operation with the MOT beams off, and bright trap lifetime measurement with the MOT beams on, follows the readout. Then a second atom readout is applied to see if there is any atom left in the trap.

5.2 Results

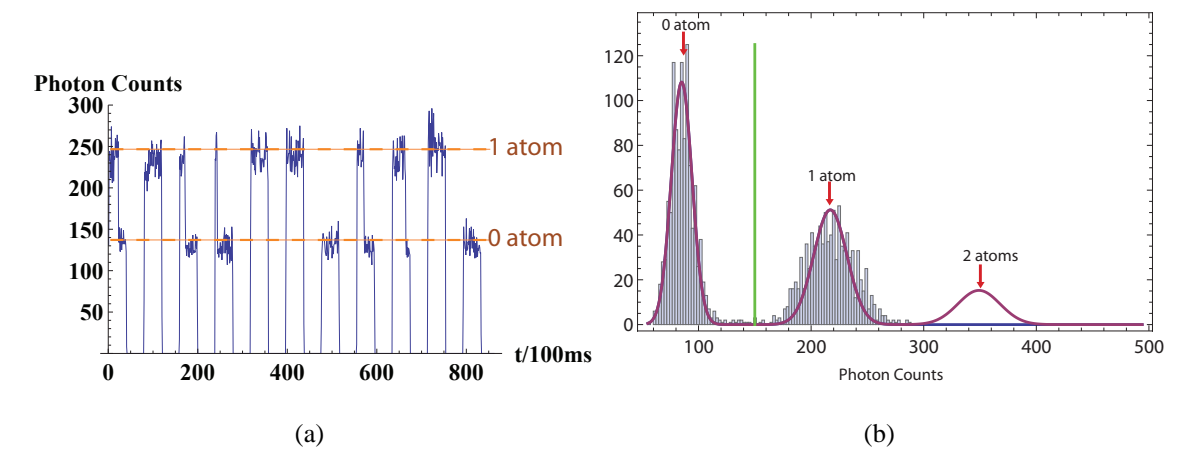


Figure 5.2 (a)Typical photon counter data for a lifetime measurement with cooling light on, and continuous readout.(b)Histogram of photon counts for atom loading, integrated for 100ms, loading probability=47%.

Typical photon counter data for a lifetime measurement on the bright BoB is shown in Figure 5.2(a)[Li 12], where a clear step between 1 atom signal and the background can be seen. Figure 5.2(b) is a typical histogram of atom loading in the crossed vortex BoBs. The photon counter is integrated for 100ms for each data point. A maximum loading probability of 50% has been observed when there is a good overlap between the MOT peak and BoB and a high atom density. For a stochastic loading following Poisson distribution $P(k) = \frac{N^k e^{-N}}{k!}$, the probability of loading one atom is $P(1) \leq 36.8\%$. It is obvious we have a sub-Poissonian atom loading.

The loading histogram is fitted with a quasi-Poisson distribution over atom and photon numbers.

$$f(n) = A \sum_{k=0}^{k=1} \frac{N^k e^{-N}}{k!} \frac{1}{\sqrt{2\pi (n_{bg} + k n_{1atom})}} \exp(-\frac{(n - (n_{bg} + k n_{1atom}))^2}{2(n_{bg} + k n_{1atom})}),$$
 (5.1)

where f(n) is the number of events of getting n counts on the photon counter. The fitting result is: $N=0.76, n_{bq}=85, n_{1atom}=132.$

We have not seen any two atom loading events. This could be understood by the collisional blockade[Schlosser 01]. The Poisson distribution tells us that the atom number should be distributed as $P_k = \frac{N^k e^{-N}}{k!}$. By photon assisted collisional blockade, atoms will be lost from the trap in pairs. So we are left with one atom only if there are odd number of atoms in the trap originally. $\sum_{k=odd}^{\infty} \frac{N^k e^{-N}}{k!} = \frac{1}{2}$. We could load one atom half the time at most. This blockade effect could be strong in the BoB, and it could have happened during the first 20ms when MOT and BoB overlaps, so we do not see this process in the photon counter signal.

The number of photons counted by the photon counter for one atom in 100ms is typically $100 \sim 200$. With the readout beam intensity $I = 2I_{sat}$ and detuning $\Delta = -6\Gamma$, the scattering rate is about 20000/100ms. So the photon collection efficiency is about $0.5\% \sim 1\%$. The asphere has an effective focal length f = 34mm, and the aperture is about 24mm, so the collection angle is about $\Omega/4\pi = 2.8\%$. Total transmission of the photon collecting optics is about 50%, and the quantum efficiency of the photon counter at 852nm is about 50%. So we are expecting a photon collection efficiency of about 0.7%.

Contributions to the background counts from different light sources are accounted for in Table 5.1. The main source of background is the 852nm light scattered by background thermal Cs atoms, and that is the main reason why the background counts do not stay constant from day to day in our experiments.

Table 5.1 Photon sources for the background counts in the single atom readout signal. With integration time t = 100 ms, $n_{bg} \approx 85$.

background Cs atom	532nm trap	cell glass scattering	environmental light and
fluorescence	laser(0.4W)		counter dark count
43	19	3	30

5.3 Atom Temperature

We use the drop and recapture method to measure the atom temperature inside the trap. We run a Monte-Carlo simulation to fit the recapture probability with experimental data.

Suppose the initial velocity of the atom obeys Maxwell-Boltzmann distribution of temperature T_0 , $v_i = \sqrt{\frac{1}{2\pi m k_B T_0}} \exp(-m v_i^2/2k_B T_0)$, where i=x,y,z. During the drop process, we turn off the dipole trap, the MOT beams and magnetic field for a time of t, then the atom undergoes a free motion with the force of gravity alone. The final velocity is calculated to be v_f , and the final position is (x_f,y_f,z_f) . Finally we turn the trap back on to recapture the atom, and the MOT beams to see if the atom is still present in the trap. If the mechanical energy $\frac{1}{2}mv_f^2 + U(x_f,y_f,z_f)$ is greater than the trap depth, or the atom has moved out of the trap region confined by the range, if any one of the following equations is satisfied.

$$|x_f| > x_{max}, |y_f| > y_{max}, |z_f| > z_{max}$$

$$\frac{\partial U(x_f, y_f, z_f)}{\partial x} x_f < 0, \frac{\partial U(x_f, y_f, z_f)}{\partial y} y_f < 0, \frac{\partial U(x_f, y_f, z_f)}{\partial z} z_f < 0$$
(5.2)

where $x_{max}, y_{max}, z_{max}$ are pre-assigned trap sizes.

Figure 5.3 shows some drop-and-recapture temperature measurements. With one stage PGC (-30MHz detuning), the atom temperature in the trap is about $10\mu\text{K}$, and by adding a second stage PGC (-50MHz detuning) the atom temperature drops down to about $4\mu\text{K}$.

5.4 Lifetime Measurement

The lifetime of an atom in the dark trap is measured with all the lasers off except the green trap laser between two readout pulses. The lifetime in the bright trap is measured with the PGC light on between two readout pulses. Figure 5.4 shows some typical lifetime measurement curves. The decaying time constant for different trap depth is summarized in Figure 5.5.

We can see that the lifetime in a 100 μ K bright trap is low. But as the trapping depth increases to over 200 μ K, the lifetime stays about the same, and the lifetime with the cooling beams on is smaller than that with the cooling beams off. This is probably because the temperature of the atom is so small ($\sim 20\mu$ K) compared with the trap depth that thermal escape is not the main contributor

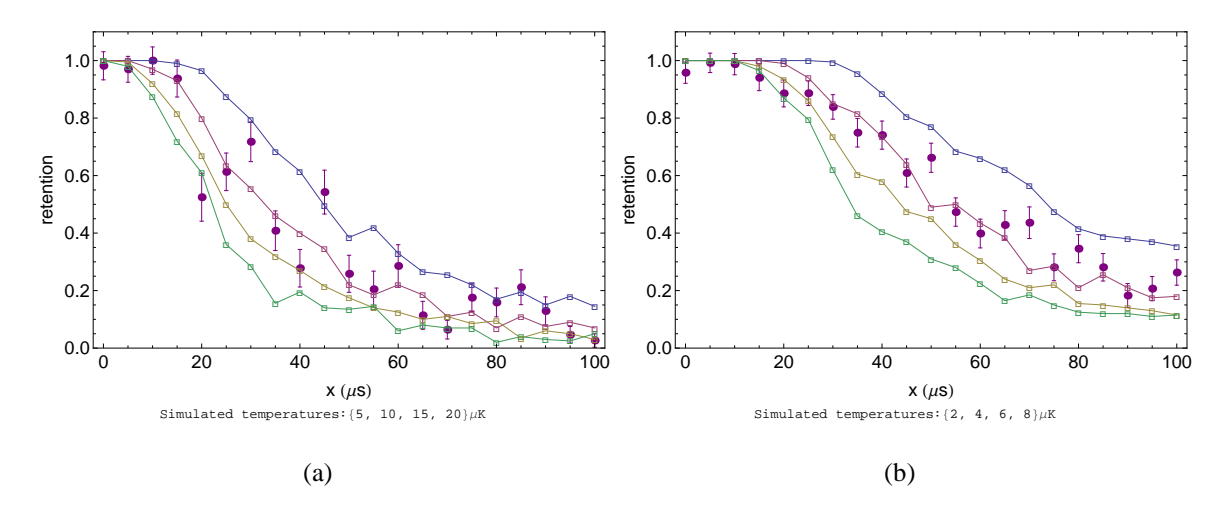


Figure 5.3 Temperature measurements of a single atom in a 200 μ K vortex BoB, (a) with one stage PGC at detuning -6Γ , (b) with two stage PGC at detuning -6Γ and -10Γ .

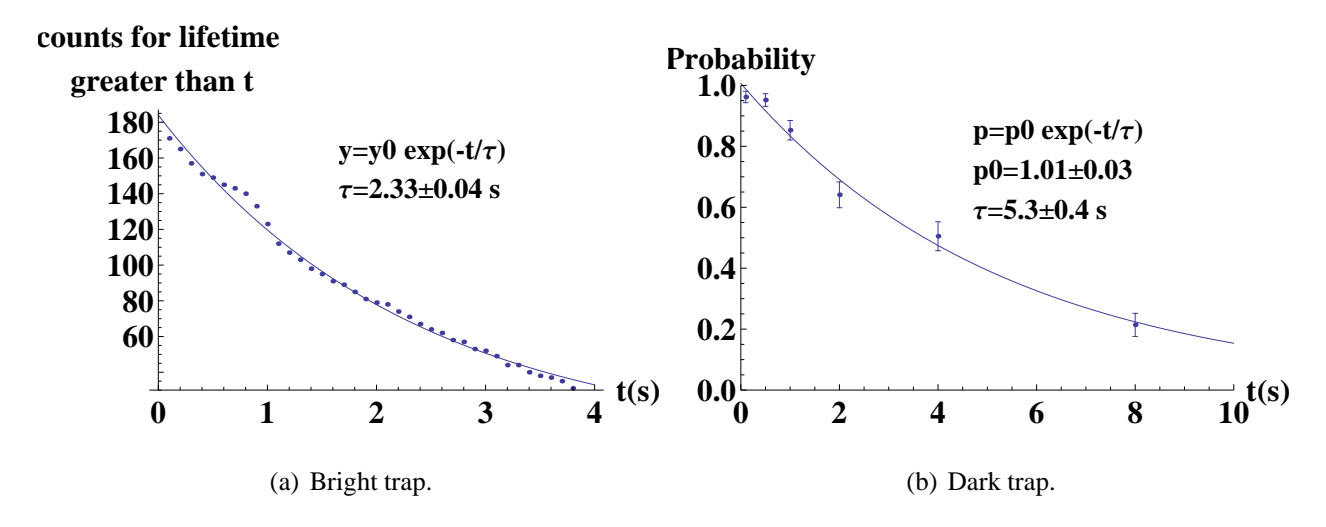


Figure 5.4 Lifetime of a single atom in a 380 μ K vortex BoB.

to the atom loss. As we will explain in the next section, the atom loss is mainly from collisions with the background gas. If we turn off the cooling beams, there would be little possibility for the atom to stay at the excited state. Ground state atoms have a smaller collisional cross section than the excited state atoms, so the atom could stay in the trap longer. We can also infer that there is little heating from the BoB laser, a main advantage of the bottle trap.

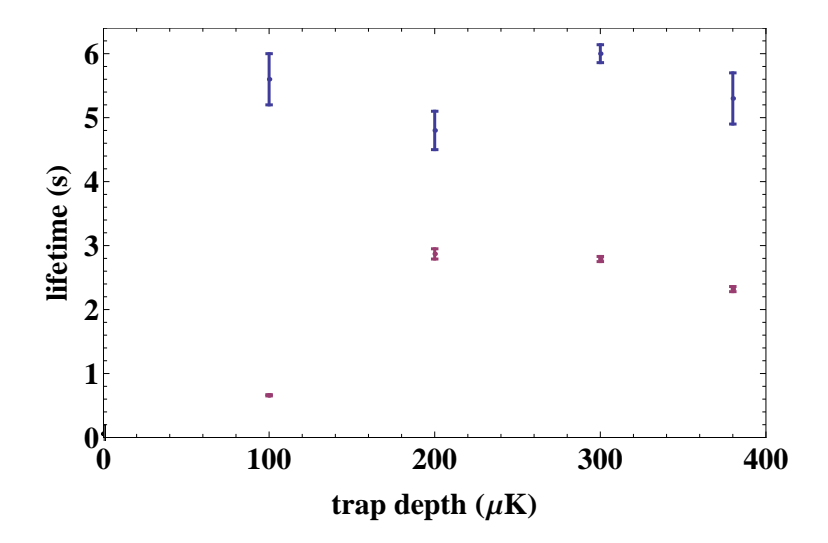


Figure 5.5 Lifetime of a single atom in a vortex BoB for different trapping depth.

5.5 Collisional Atom Loss

The difference in lifetime in bright and dark traps can be explained by the different collisional cross section of ground and excited state atoms.

The ground state atom interact with the background hot atoms (in ground state) via Van der Waals potential with a Lennard-Jones form:

$$V(r) = -\frac{C_6}{r^6} + \frac{C_{12}}{r^{12}} \tag{5.3}$$

when r is large compared with atom size, the higher order term could be ignored.

Due to the resonant interchange interaction between s-p states, the atom in the $6p_{3/2}$ state interact with the hot atoms via potential

$$V(r) = -\frac{C_3}{r^3} (5.4)$$

to the lowest order.

To get the collisional loss rate, we consider the following process[Bjorkholm 88].

Because the trapping potential is very small ($200\mu\text{K}$) compared to the kinetic energy of the hot atom, we can assume the atom inside the trap to be at rest, and the interaction does not change the trajectory of the hot atom. The collision only changes the transverse momentum of the hot atom, thus transferring the same momentum to the trapped atom due to the conservation of momentum.

Suppose the hot atom has a velocity of $v\hat{z}$, and the impact parameter is b in the y direction, then the momentum transferred to the trapped atom is

$$\Delta p_y = \int F_y dt = \int \frac{\partial V(x=0, y=b, z)}{\partial y} \frac{dz}{v}$$
$$= \frac{1}{v} \int_{-\infty}^{+\infty} \frac{\partial V(x=0, y=b, z)}{\partial y} dz$$

The potential is of the form

$$V(r) = -\frac{C_n}{r^n}$$

$$\frac{\partial V}{\partial y} = \frac{nC_n}{r^{n+2}}y$$
(5.5)

so the momentum change can be calculated by

$$\Delta p_y = \frac{nC_n b}{v} \int_{-\infty}^{+\infty} \frac{1}{b^2 + z^2} dz$$

$$= \frac{nC_n}{vb^n} \int_{-\infty}^{+\infty} (1 + z^2)^{-(n+2)/2} dz$$

$$= \frac{nC_n a_n}{vb^n}$$
(5.6)

where $a_n = \int_{-\infty}^{+\infty} (1+z^2)^{-(n+2)/2} dz$.

If this momentum change is larger than a critical value $p_c = \sqrt{2U_{max}m}$, where U_{max} is the trap depth, the atom is lost from the trap. From this we can get a critical impact parameter

$$b_c = \left(\frac{nC_n a_n}{v p_c}\right)^{\frac{1}{n}} \tag{5.7}$$

The cross section of loss is $\pi b_c^2(v)$. And the total loss rate is

$$R_n = \pi N \int_0^\infty v b_c^2 f(v) dv \tag{5.8}$$

where $N=P/k_bT$ is the atom density of background Cs, and the thermal velocity distribution $f(v)=\sqrt{\frac{2}{\pi}(\frac{m}{k_bT})^3}v^2\exp(-\frac{mv^2}{2k_bT}).$

Using $C_6=6330$ and $C_3=13.22$ [Niemax 75] in atomic units, $P=1.0\times 10^{-9}$ Torr, T=300K, assuming the fraction of the atom on the excited state is 1.5%, which is estimated by $\frac{R_{counter}}{QE\times\Gamma}$, with photon counts per second $R_{counter}=1500$, quantum efficiency of the photon collection system

QE=0.1%, and $\Gamma=2\pi5.2\times10^6/\mathrm{s}$, we get a lifetime estimate as follows. The data do not follow the curve perfectly probably because the vacuum pressure is not very stable.

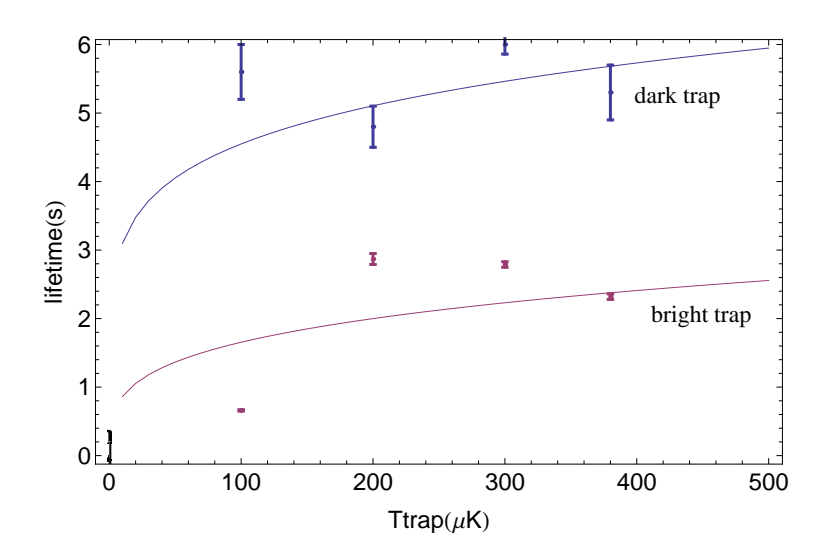


Figure 5.6 Calculated collisional atom lifetime in the trap with the cooling light on (bright) and off (dark), along with experimental lifetime data represented by error bar data points.

In our experiments, we usually use a $80 \sim 100 \mathrm{ms}$ gap time (for atom state manipulations) between two atom $100 \mathrm{ms}$ fluorescence reading pulses, in a $200 \sim 300 \mu \mathrm{K}$ trap. So the retention at the end should be about $\exp(-0.1/5 - 0.1/3 - 0.1/3) = 93\%$. If the background pressure is doubled, the retention is reduced to 84%. The retention we measured is usually in the range of $80 \sim 90\%$. But if we can shorten the time of each section to 10ms, the retention would only change from 99% to 98% when the pressure is doubled. So increasing the overall speed is vital for increasing the retention stability.

Chapter 6

Ground State Rabi

The qubits we are using are the ground state hyperfine manifolds of Cs. The rotations of the qubits can be coherently driven by the direct transition between the hyperfine levels with microwaves, or through higher order processes such as two photon Raman transitions. For the microwave method, in order to have single site addressability in a qubit array, additional optical or gradient electric/magnetic fields need to be applied to the system to differentially shift the energies of atoms at different positions[Weitenberg 11]. In our experiments, we are using a two-photon Raman process via a third excited level (7P of Cs in this case) as shown in Figure. 6.1. To minimize the error due to the spontaneous emissions from the excited level, the detuning Δ is set to be large (\sim 50GHz).

For a coherent Raman Rabi flopping, the populations of state $|1\rangle = |6S_{1/2}, F = 4\rangle$ and state $|0\rangle = |6S_{1/2}, F = 3\rangle$ evolve as $c_1(t)|1\rangle + c_2t|0\rangle$. $c_1(t)$ and $c_2(t)$ are given by

$$(c_1(t), c_2(t))^T = U(t) (c_1(0), c_2(0))^T$$
(6.1)

$$U(t) = e^{-i\frac{|\Omega_1|^2 + |\Omega_2|^2}{4\delta}t} \begin{pmatrix} e^{i\frac{\Delta_{12}t}{2}} \left(\cos(\frac{\Omega't}{2}) - i\frac{\Delta'}{\Omega'}\sin(\frac{\Omega't}{2})\right) & -ie^{i\frac{\Delta_{12}t}{2}} \frac{\Omega_R^*}{\Omega'}\sin(\frac{\Omega't}{2}) \\ -ie^{-i\frac{\Delta_{12}t}{2}} \frac{\Omega_R}{\Omega'}\sin(\frac{\Omega't}{2}) & e^{-i\frac{\Delta_{12}t}{2}} \left(\cos(\frac{\Omega't}{2}) + i\frac{\Delta'}{\Omega'}\sin(\frac{\Omega't}{2})\right) \end{pmatrix}$$
(6.2)

where Ω_1 and Ω_2 are the single photon Rabi frequencies, $\delta = \Delta_1 + \Delta_2$, the effective two photon Rabi frequency $\Omega_R = \frac{\Omega_1 \Omega_2^*}{\delta}$, $\Delta_{12} = \Delta_1 - \Delta_2$ is the two photon detuning when ignoring any AC Stark shifts, $\Delta' = \Delta_{12} + \frac{|\Omega_1|^2 - |\Omega_2|^2}{\delta}$ is the two photon detuning taking into account AC Stark shift, and $\Omega' = \sqrt{\Delta'^2 + |\Omega_R|^2}$.

The calculations of the Rabi frequencies need to be treated with great care. The following section summarizes some relevant formulas.

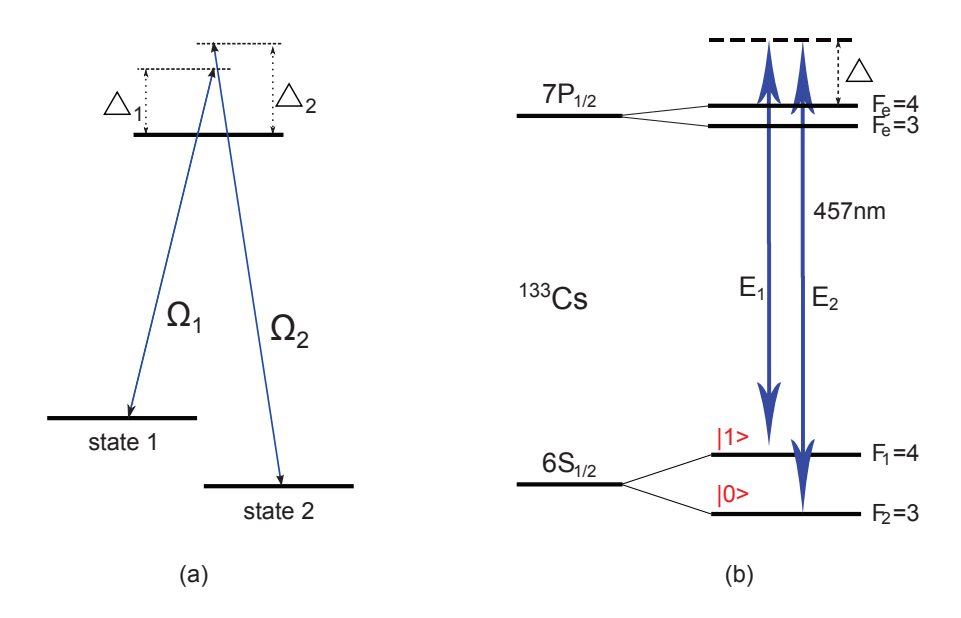


Figure 6.1 (a)Two photon Raman transition, (b)Raman transition of the Cs ground hyperfine states.

6.1 Rabi Frequency Calculation

Effective Rabi frequency

$$\Omega_R = \Omega_1 \Omega_2^* / 2\Delta_0 \tag{6.3}$$

Suppose state 1, 2 are coupled through state e,

$$\Omega_{1,2} = e \langle e | E_{1,2} \vec{\epsilon}_{1,2} \cdot \vec{r} | 1, 2 \rangle / \hbar \tag{6.4}$$

The field amplitudes are $E_{1,2}=\sqrt{\frac{4P_{1,2}}{\pi\epsilon_0cw_xw_y}}$. For particular hyperfine states $|1\rangle=|F_1,m_1\rangle$, $|2\rangle=|F_2,m_2\rangle$, $|e\rangle=|F_e,m_e\rangle$, the dipole matrix element could be reduced by Wigner-Eckart theorem on a spherical tensor basis.

$$\langle F', m'|r_q|F, m\rangle = \langle F'||r||F\rangle(-1)^{F'-m'} \begin{pmatrix} F' & 1 & F \\ -m' & q & m \end{pmatrix}$$

$$(6.5)$$

the rank 1 tensors are $r_{\pm 1} = \mp (x \pm iy)/\sqrt{2}$, $r_0 = z$. We can further reduce the matrix element by [Sobelman 92]

$$\langle J_1 J_2 J || T_k || J_1' J_2 J' \rangle = (-1)^{J_1 + J_2 + J' + k} \sqrt{(2J+1)(2J'+1)} \langle J_1 || T_k || J_1' \rangle \left\{ \begin{array}{cc} J_1 & J & J_2 \\ J' & J_1' & k \end{array} \right\}$$
 (6.6)

SO

$$\langle F'||r||F\rangle = \langle J'||r||J\rangle(-1)^{F+J'+1+I}\sqrt{(2F+1)(2F'+1)} \begin{cases} J' & F' & I \\ F & J & 1 \end{cases}$$

$$= \langle L'||r||L\rangle(-1)^{F+J+J'+L'+S+I}\sqrt{(2F+1)(2J+1)(2F'+1)(2J'+1)}$$

$$\begin{cases} L' & J' & S \\ J & L & 1 \end{cases} \begin{cases} J' & F' & I \\ F & J & 1 \end{cases}$$
(6.7)

where
$$\left\{ \begin{array}{ccc} J_1 & J_2 & J_3 \\ J_4 & J_5 & J_6 \end{array} \right\}$$
 is the Wigner's 6-J symbol.

In summary, in the L, S, J, m_J basis,

$$\langle L'S'J'm'_{J}||r_{q}||LSJm_{J}\rangle = \langle L'||r||L\rangle c_{fs}(L,S,J,m_{J};L',S',J',m'_{J};q)$$

$$c_{fs}(L,S,J,m_{J};L',S',J',m'_{J};q) = (-1)^{J'-m'_{J}+L'+S+J+1}\sqrt{(2J+1)(2J'+1)}$$

$$\begin{pmatrix} J' & 1 & J \\ -m'_{J} & q & m_{J} \end{pmatrix} \begin{cases} L' & J' & S \\ J & L & 1 \end{cases}$$
(6.8)

in the J, I, F, m_F basis,

$$\langle J'IF'm'_{F}||r_{q}||JIFm_{F}\rangle = \langle L'||r||L\rangle c_{hf}(J,I,F,m_{F};J',I,F',m'_{F};q)$$

$$c_{hf}(J,I,F,m_{F};J',I,F',m'_{F};q) = (-1)^{F'-m'_{F}+F+J+J'+L'+S+I}\sqrt{(2F+1)(2F'+1)(2J+1)(2J'+1)}$$

$$\begin{pmatrix} F' & 1 & F \\ -m'_{F} & q & m_{F} \end{pmatrix} \begin{cases} L' & J' & S \\ J & L & 1 \end{cases} \begin{cases} J' & F' & I \\ F & J & 1 \end{cases}$$

$$(6.9)$$

The reduced matrix element

$$\langle L'||r||L\rangle = (-1)^{L'}\sqrt{(2L+1)(2L'+1)}\begin{pmatrix} L' & 1 & L \\ 0 & 0 & 0 \end{pmatrix}\langle L'|r|L\rangle$$
 (6.10)

where $\langle L'|r|L\rangle = \int r^3 dr R_{L'}(r) R_L(r)$ The transformation from the hyperfine structure basis to the fine structure basis can be done using the Clebsch-Gordan coefficients

$$|JIFm_F\rangle = \sum_{m_J} C_{J,m_J;I,m_F-m_J}^{Fm_F} |J,m_J;I,m_F-m_J\rangle$$
 (6.11)

Specifically for the ground state Raman, the Rabi frequency can be calculated as follows. The transitions involved are shown in Figure 6.1. Suppose the polarization state of the driving fields E_1 , E_2 can be written as

$$\vec{\epsilon}_j = a_{j,0}\vec{e}_0 + a_{j,1}\vec{e}_1 + a_{j,-1}\vec{e}_{-1} \tag{6.12}$$

where $\vec{e}_0 = \hat{z}$, $\vec{e}_1 = -\frac{1}{\sqrt{2}}(\hat{x}+i\hat{y})$, and $\vec{e}_{-1} = \frac{1}{\sqrt{2}}(\hat{x}-i\hat{y})$. E_1 corresponds to the transition $|6S_{1/2},F_1|=4,m_{F_1}\rangle \to |7P_{1/2},F_e,m_{F_e}\rangle$, and E_2 corresponds to the transition $|6S_{1/2},F_2|=1$

 $3,m_{F_2}
angle
ightarrow |7P_{1/2},F_e,m_{F_e}
angle$. The Rabi frequency is

$$\begin{split} \Omega_{R} = & \frac{e^{2}E_{1}E_{2}^{*}}{\hbar^{2}} \sum_{p,q,F_{e}} \frac{a_{1,p}a_{2,q}^{*}\delta_{m_{F_{1}}+p,m_{F_{2}}+q}\langle 7P_{1/2},F_{e},m_{F_{e}}=m_{F_{1}}+p|r_{p}|6S_{1/2},F=4,m_{F_{1}}\rangle\langle 6S_{1/2},F=3,m_{F_{2}}|r_{-q}|7P_{1/2},F_{e},m_{F_{e}}=m_{F_{1}}+p\rangle}{2\Delta_{F_{e}}} \\ = & \frac{\Omega_{1,0}\Omega_{2,0}^{*}}{2\Delta} \left(\frac{\Delta}{\Delta+\Delta_{hf,7}P_{1/2}}c_{3}+c_{4}\right) \end{split} \tag{6.13}$$

where $\Omega_{j,0}=ea_0E_j\langle 7P_{1/2}||r||6S_{1/2}\rangle/\hbar$, $\Delta_{hf,7P_{1/2}}=2\pi\times377.4\mathrm{MHz}$ is the hyperfine splitting of $7P_{1/2}$. The radial matrix element $\langle 7P_{1/2}|r|6S_{1/2}\rangle=0.338$ [Vasilyev 02].

$$c_{F_e} = \sum_{p,q=-1,0,1} \sum_{m_{F_e}} a_{1,p} a_{2,q}^* c_{hf}(J_1, I, F_1, m_{F_1}; J_e, I, F_e, m_{F_e}; p) c_{hf}(J_e, I, F_e, m_{F_e}; J_2, I, F_2, m_{F_2}; -q)$$

$$(6.14)$$

We are using two beams with the same polarization, $m_{F_1} = m_{F_2}$.

6.2 AC Stark shift

Since the hyperfine splitting of Cs ground states, 9.2 GHz, is on the same order of the detuning. When calculating the AC Stark shift ,we should also consider the coupling of $7P_{1/2}$ to $6S_{1/2}$, F=4 via E_2 , and $7P_{1/2}$ to $6S_{1/2}$, F=3 via E_1 . The AC Stark shift can be calculated by

$$\Delta_{ac} = \sum_{j,p,F_e} \frac{e^2 E_j^2 a_{j,p}^2}{4\hbar^2 \Delta_{F_e}} |\langle 7P_{1/2}, F_e, m_{F_e} = m_{F_1} + p | r_p | 6S_{1/2}, F_1, m_{F_1} \rangle|^2 - \sum_{j,p,F_e} \frac{e^2 E_j^2 a_{j,p}^2}{4\hbar^2 \Delta_{F_e}} |\langle 7P_{1/2}, F_e, m_{F_e} = m_{F_1} + p | r_p | 6S_{1/2}, F_2, m_{F_2} \rangle|^2$$

$$= \sum_{j,p,F_e} |a_{j,p}|^2 \Omega_{j,0}^2 \frac{|c_{hf}(J_1, I, F_1, m_{F_1}; J_e, I, F_e, m_{F_e} = m_{F_1} + p; p)|^2}{4\Delta_j (7P_{1/2}, F_e; 6S_{1/2}, F_1)} - \sum_{j,p,F_e} |a_{j,p}|^2 \Omega_{j,0}^2 \frac{|c_{hf}(J_2, I, F_2, m_{F_2}; J_e, I, F_e, m_{F_e} = m_{F_2} + p; p)|^2}{4\Delta_j (7P_{1/2}, F_e; 6S_{1/2}, F_1)}$$
(6.15)

Figure 6.2(b) shows some sample calculations of the AC Stark shifts.

6.3 Raman Laser Setup

The laser setup for the Raman transition is shown in Figure 6.3. For each laser, the laser source is a 914nm ECDL. The frequency of the laser is locked by the Pound-Drever-Hall technique to a reference high finesse cavity ($\mathcal{F} \sim 1500$). Then most of the light is sent to a tapered amplifier (TA) after which we get up to 400mW of 914 light. The optimum input power for the TA is about 45mW. The output of the TA is collimated and reshaped to obtain a beam closer to circular and then matched into a bow-tie cavity used for second-harmonic generation (SHG). The SHG cavity has four mirrors and a 2cm PPKTP crystal. The SHG gives us about 35mW of blue power. An

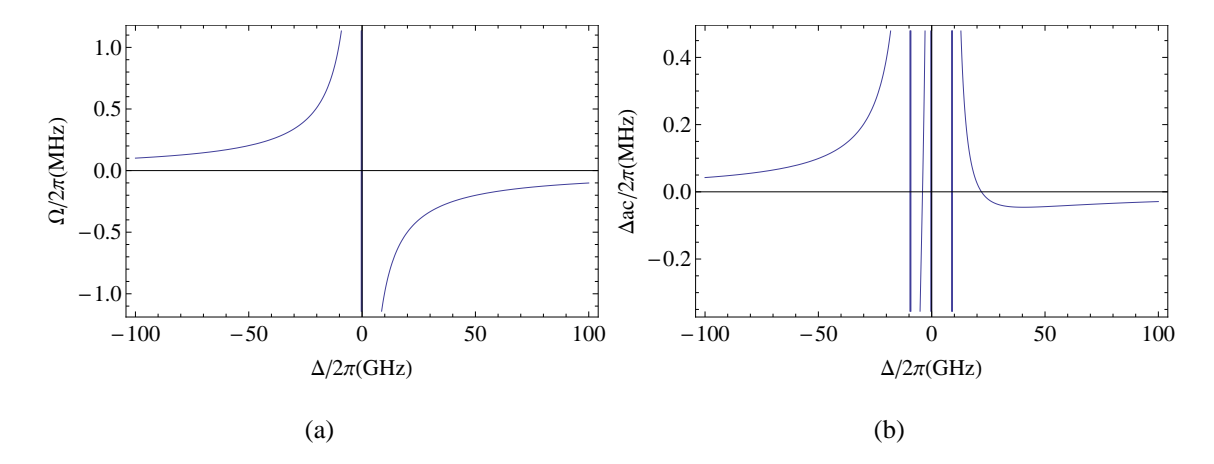


Figure 6.2 Caculated Rabi frequency and AC Stark shift of ground state Raman transition, from $6S_{1/2}, F=4, m_F=0$ to $6S_{1/2}, F=3, m_F=0$ via $7P_{1/2}, m_F=1, P_1=1 \mathrm{mW}, P_2=0.5 \mathrm{mW},$ $w_{457}=5.9 \mu \mathrm{m}.$

AMO is inserted to stabilize the power, and the zero order diffraction is the output. A double pass AOM path is used in one of the lasers (back laser) to work as the fast feedback of the phase lock loop. But half of the back laser power is lost in this double pass AOM setup. Before the lasers are sent to a fiber, they are combined by a 50/50 beam splitter. Half of the power is sent out through a fiber. The other half is sent to a fast photo detector. The detector outputs a beat signal of the two blue lasers. Then the beat signal is mixed with a $f \sim 9.2 \mathrm{GHz}$ reference RF signal generated by a frequency generator. The error signal is feedback to the reference cavity and double pass AOM of the back laser. This way the back laser is phase locked to the front laser with a frequency offset equal to the hyperfine splitting of Cs $6S_{1/2}$. The back laser (power P_2) frequency is set higher than the front laser (power P_1) frequency.

We can get about 7mW of back laser and 14mW of front laser in front of the output fiber. The power is 3+6mW after the fiber. Before going to the atom, another AOM is set up between two fiber launchers to work as an on/off switch. The output after the last blue fiber is about 1+2mW, 70% of which gets to the atom eventually.

6.4 Experimental Results of TPS and RFE

At the beginning of our experiments, we usually initialize the atom into the $|6S_{1/2}, F = 4\rangle$ state, $(c_1(0), c_2(0)) = (1, 0)$. According to Equation 6.2, the probability of the atom in state $|6S_{1/2}, F = 3\rangle$ after a Rabi pulse of time t is given by

$$|c_2(t)|^2 = \left|\frac{\Omega_R}{\Omega'}\sin(\frac{\Omega't}{2})\right|^2$$

So for a two photon spectrum scan with a fixed pulse length t, the retention (F=3) can be fitted with a sinc squared function. Figure 6.4 shows a typical TPS experimental results.

Figure 6.5 shows a typical ground state Rabi flopping curve.

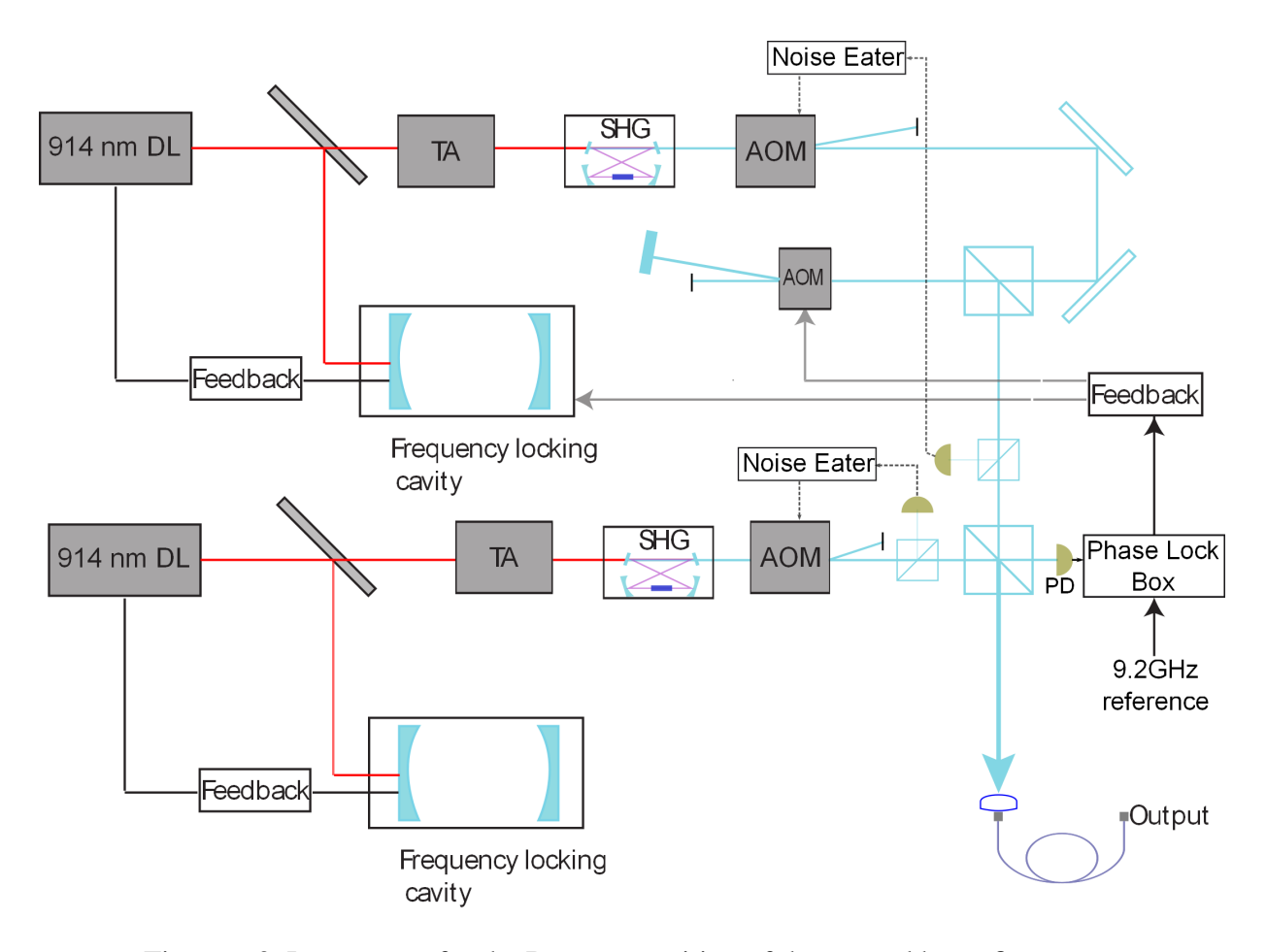


Figure 6.3 Laser setup for the Raman transition of the ground hyperfine states.

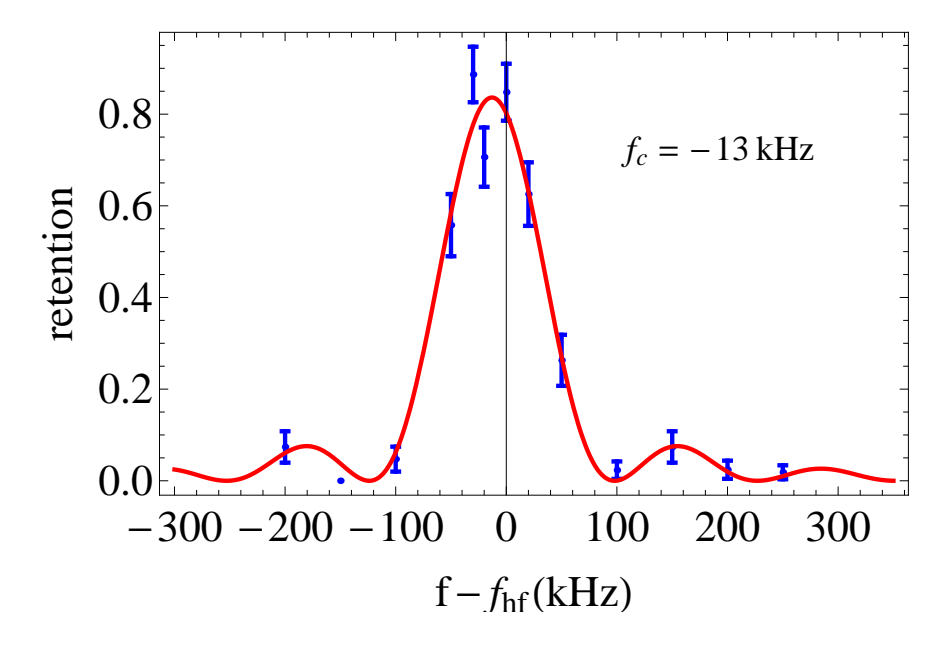


Figure 6.4 Two photon spectrum of the ground Raman transition, with fitted $f_c=-13 \mathrm{kHz}$, $\Omega_R=53 \mathrm{kHz}$. The beam parameters are $P_1=0.93 \mathrm{mW}$, $P_2=0.47 \mathrm{mW}$ with some misalignment, $w=5.9 \mu \mathrm{m}$, $\Delta=40 \mathrm{GHz}$.

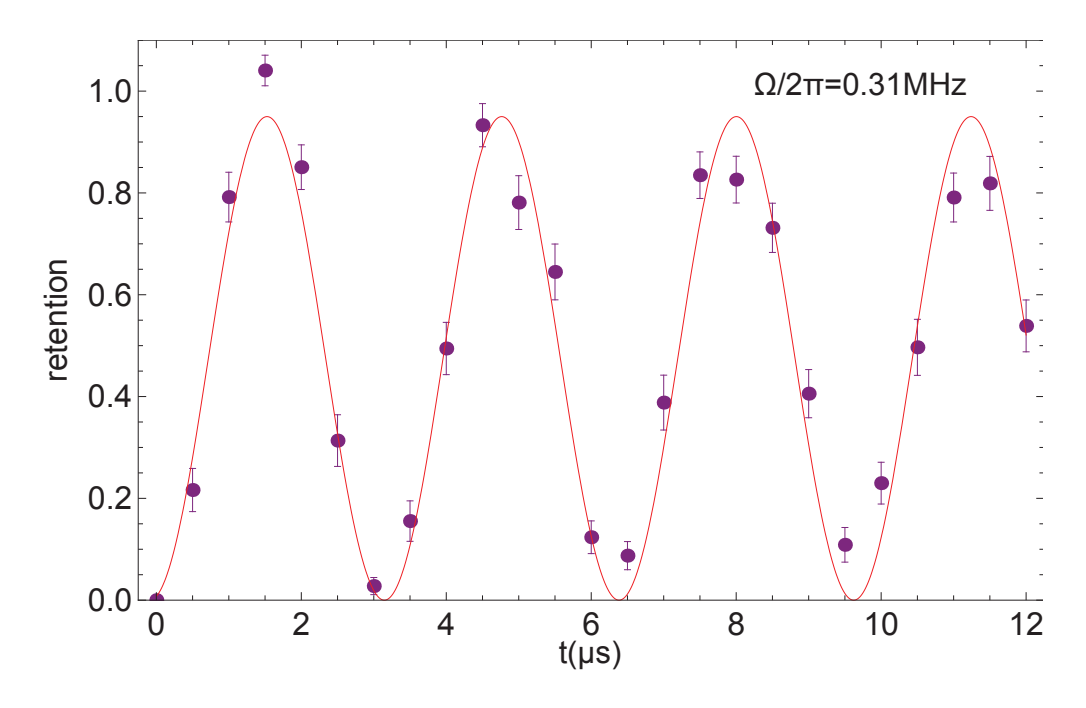


Figure 6.5 Rabi flopping of ground hyperfine states, $P_1=0.93 \mathrm{mW}$, $P_2=0.47 \mathrm{mW}$, $w=5.9 \mu \mathrm{m}$, $\Delta=40 \mathrm{GHz}$, $f_{RF}=9.192620 \mathrm{GHz}$, Rabi frequency $\Omega/2\pi=0.31 \mathrm{MHz}$, amplitude A=0.95.

6.5 T2 measurements

The coherence time is measured in the usual Ramsey fringe method: a $\frac{\pi}{2}$ pulse is applied to prepare the atom into the superposition state; and then it left to freely precess in the trap for a time of T_p ; then a second $\frac{\pi}{2}$ pulse is applied before the final state measurement. The oscillation fringes are measured for different T_p s, and the oscillation amplitudes are exponentially fitted to interpolate the T2 time in Figure 6.7. The T2 time we have measured is $43 \pm 9 \text{ms}$.

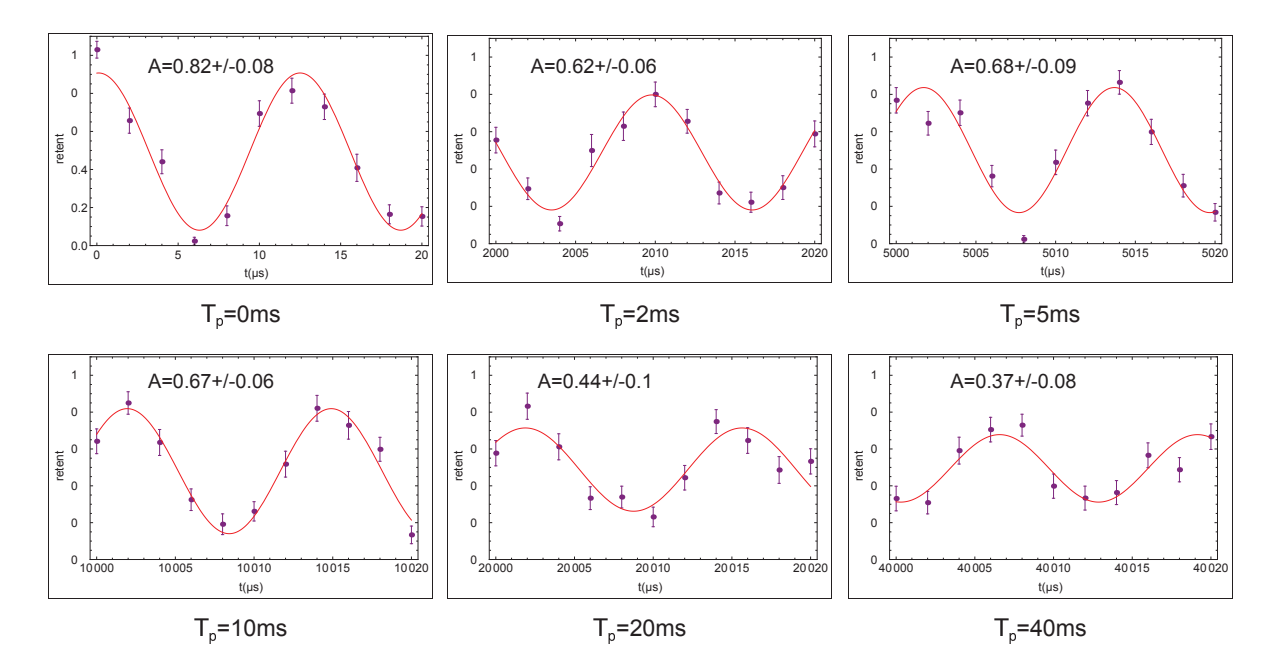


Figure 6.6 Ramsey fringes for different T_p intervals.

6.6 Decoherence Factors

6.6.1 Motional Decoherence

One of the main factor for dephasing is the atomic motion. As the atom moves in the trap, it experiences varying trapping light intensity, thus varying differential potential shifts for the $|F=4,m_F=0\rangle$ and $|F=3,m_F=0\rangle$ states. The differential shift is given by

$$\hbar\delta(x, y, z) = \eta U(x, y, z) \tag{6.16}$$

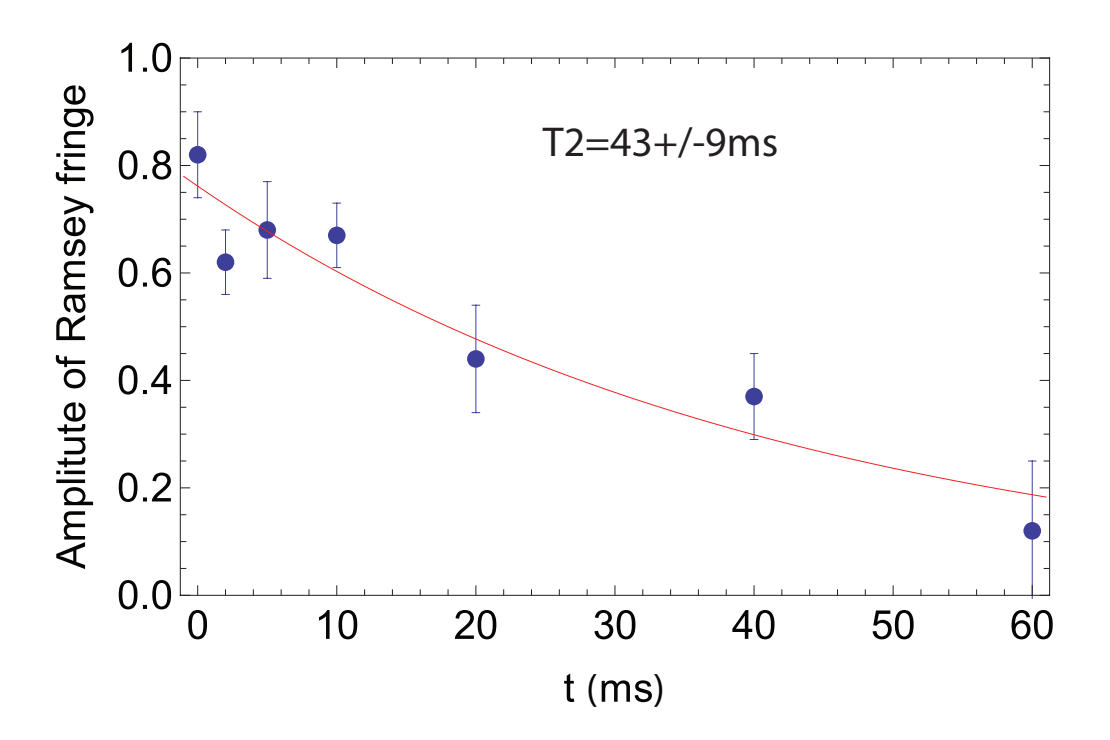


Figure 6.7 T2 decoherence time fit.

where U(x,y,z) is the potential energy, $\eta = \frac{f_{hf}}{c/\lambda_{BBT} - c/\lambda_0} = 4.34 \times 10^{-5}$. For an atom of temperature T, the energy distribution of the atom in the dipole trap obeys a three dimensional Boltzmann distribution with probability density

$$p(E) = \frac{E^2}{2(k_B T)^3} \exp\left(-\frac{E}{k_B T}\right) \tag{6.17}$$

Here $E = E_{kin} + U$ is the total energy of the atom. If the atom is cold enough and it is sitting at the center of the trap, the trap can be approximated by a harmonic trap. According to the virial theorem, $\langle U \rangle = E/2$, so the average differential light shift for an atom with energy E is

$$\delta_{ls} = \frac{\eta E}{2\hbar}.\tag{6.18}$$

The probability distribution of the light shift is

$$p(\delta_{ls}) = \frac{K^3}{2} \delta_{ls}^2 \exp(-K\delta_{ls}), \tag{6.19}$$

with $K = 2\hbar/(\eta k_B T)$.

Starting with state $|F=4,m_F=0\rangle$, $(c_1(0),c_2(0))=(1,0)$, the state vector amplitude of state $|F=3,m_F=0\rangle$ after a Ramsey sequence $T_p=t$ is

$$c_2(t) = \cos \delta t, \tag{6.20}$$

where the two photon detuning $\delta = \Delta_{AC} - \delta_{ls} - \delta_{B}$ with δ_{B} the quadratic Zeeman shift. So the average Ramsey signal

$$c_{2}(t) = \int_{0}^{2U_{m}} p(\delta_{ls}) \cos \left[(\Delta_{AC} - \delta_{ls} - \delta_{B})t \right] d\delta_{ls}$$

$$\approx \int_{0}^{\infty} p(\delta_{ls}) \cos \left[(\Delta_{AC} - \delta_{ls} - \delta_{B})t \right] d\delta_{ls}$$

$$= \frac{K^{3}}{(K^{2} + t^{2})^{3/2}} \cos \left[(\Delta_{AC} - \delta_{B})t + \kappa(t, K) \right],$$
(6.21)

where, $\kappa(t, K) = -3 \arctan(t/K)$.

The 1/e decoherence time T_2^* can be calculated by $\left|\frac{K^3}{(K^2+T_2^{*2})^{3/2}}\right|^2=1/e$ (because we are measuring $|c_2(t)|^2$ in experiments), and we get

$$T_2^* = \sqrt{e^{1/3} - 1}K = 0.63 \frac{2\hbar}{\eta k_B T}.$$
 (6.22)

This is the same as that for the red detuned dipole trap[Kuhr 05]. In Figure 6.8(a) is the calculated motional decoherence T_2 time for Cs atom in a 532nm BBT. For an atomic temperature $T=4\sim 5\mu {\rm K}$ as we have measured, $T_2^*=55\sim 44{\rm ms}$.

6.6.2 Magnetic Field Fluctuations

For the clock transition from $|F=4,m_F=0\rangle \to |F=3,m_F=0\rangle$, the quadratic Zeeman shift is given by $\delta_B=\mu_2 B^2$, where the coefficient $\mu_2/2\pi=427.45 {\rm Hz/G^2}$ for Cs. Suppose there is Gaussian noises in the bias field,

$$p(B) = \frac{1}{\sqrt{2\pi}\sigma_B} \exp\left(-(B - B_0)^2 / 2\sigma_B^2\right)$$
 (6.23)

The Ramsey visibility, ignoring the motional dephasing, is

$$\langle c_{2}(t) \rangle = \int p(\delta_{B}) \cos \left[(\Delta_{AC} - \delta_{ls} - \delta_{B})t \right] d\delta_{B}$$

$$= \frac{1}{\sqrt{2\pi}\sigma_{B}} \int_{-\infty}^{\infty} \cos \left[(\Delta_{AC} - \delta_{ls} - \mu_{2}B^{2})t \right] e^{-(B-B_{0})^{2}/2\sigma_{B}^{2}} dB$$

$$\approx \frac{1}{\sqrt{2\pi}\sigma_{B}} \int_{-\infty}^{\infty} \cos \left[(\Delta_{AC} - \delta_{ls} - \mu_{2}B_{0}^{2} - 2\mu_{2}B_{0}(B - B_{0}))t \right] e^{-(B-B_{0})^{2}/2\sigma_{B}^{2}} dB$$

$$= \exp \left(-2\sigma_{B}^{2}\mu_{2}^{2}B_{0}^{2}t^{2} \right) \cos \left[(\Delta_{AC} - \delta_{ls} - \mu_{2}B_{0}^{2})t \right].$$
(6.24)

So the 1/e time for $|c_2(t)|$ is $1/\sqrt{2}\mu_2B_0\sigma_B$, and the 1/e time for $|c_2|^2$

$$T_{2,B} = \frac{1}{2\mu_2 B_0 \sigma_B}. (6.25)$$

The results for different bias fields are shown in Figure 6.8(b). If we assume atomic temperature $T=4\mu\mathrm{K}$, bias field $B_0=0.7\mathrm{G}$, and magnetic field fluctuation $\sigma_B=1.3\mathrm{mG}$, we will get $T_2^*=55\mathrm{ms}$, $T_{2,B}=200\mathrm{ms}$, and $T_2=43\mathrm{ms}$.

6.7 Quantum Tomography

To characterize a quantum system experimentally, we need to perform some complex procedures, called quantum tomography, to uniquely determine the input and output quantum states of the system, and describe the quantum processes performed by the system.

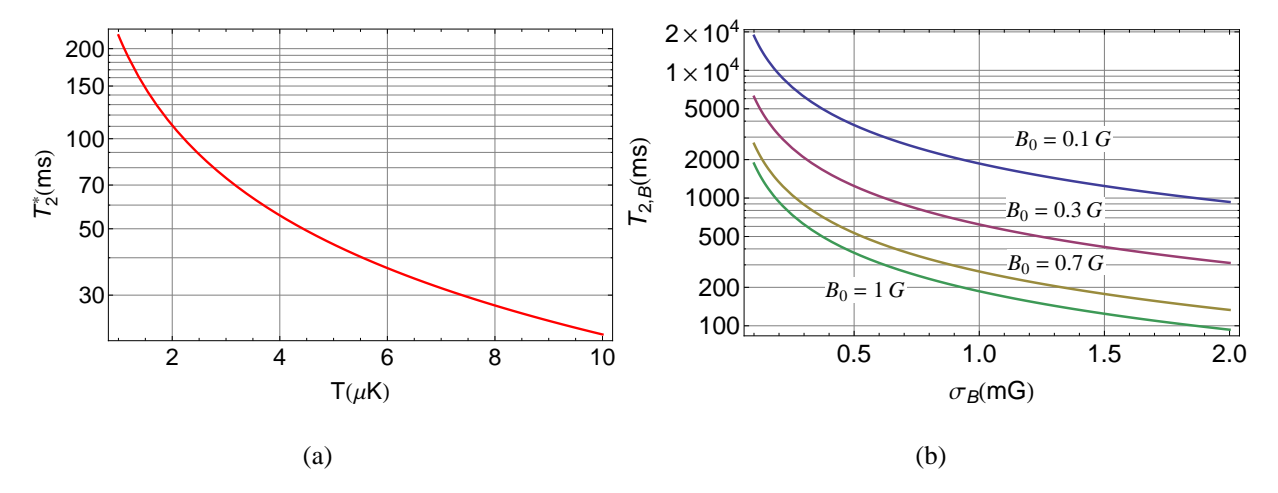


Figure 6.8 Calculated (a)motional decoherence T_2 time for Cs atom in a 532nm BBT, (b)decoherence caused by magnetic field fluctuations.

6.7.1 State Tomography

Quantum state tomography is the procedure of experimentally determining an unknown quantum state.

For single qubits, the Pauli matrices are

$$I \equiv \sigma_0 = \begin{pmatrix} 1 & 0 \\ 0 & 1 \end{pmatrix}, \sigma_x = \begin{pmatrix} 0 & 1 \\ 1 & 0 \end{pmatrix}, \sigma_y = \begin{pmatrix} 0 & -i \\ i & 0 \end{pmatrix}, \sigma_z = \begin{pmatrix} 1 & 0 \\ 0 & -1 \end{pmatrix}. \tag{6.26}$$

The set $\sigma_0/\sqrt{2}$, $\sigma_x/\sqrt{2}$, $\sigma_y/\sqrt{2}$, $\sigma_z/\sqrt{2}$ forms an orthonormal set of matrices with respect to the Hilbert-Schmidt inner product, so any state ρ can be expanded as[Nielsen 00]

$$\rho = \frac{\operatorname{tr}(\sigma_0 \rho)\sigma_0 + \operatorname{tr}(\sigma_x \rho)\sigma_x + \operatorname{tr}(\sigma_y \rho)\sigma_y + \operatorname{tr}(\sigma_z \rho)\sigma_z}{2}.$$
(6.27)

It is easy to see that $\operatorname{tr}(\sigma_0\rho)$ and $\operatorname{tr}(\sigma_z\rho)$ are the sum and difference respectively, of P_0 the population in state $|0\rangle$ and P_1 the population in state $|1\rangle$ in the z basis. $\operatorname{tr}(\sigma_x\rho)$ and $\operatorname{tr}(\sigma_y\rho)$ cannot be directly obtained from measurements in the z basis, and we need to do some rotations first, using the following identities.

$$\sigma_x = R_y^{\dagger}(-\pi/2)\sigma_z R_y(-\pi/2),$$

$$\sigma_y = R_x^{\dagger}(\pi/2)\sigma_z R_x(\pi/2),$$
(6.28)

where the rotation operators about the x, y, z axes are

$$R_{x}(\theta) = \begin{pmatrix} \cos \theta/2 & -i\sin \theta/2 \\ -i\sin \theta/2 & \cos \theta/2 \end{pmatrix}, R_{y}(\theta) = \begin{pmatrix} \cos \theta/2 & -\sin \theta/2 \\ \sin \theta/2 & \cos \theta/2 \end{pmatrix}, R_{z}(\theta) = \begin{pmatrix} e^{-i\theta/2} & 0 \\ 0 & e^{i\theta/2} \end{pmatrix}.$$
(6.29)

So the density matrix of the quantum state ρ can be reconstructed from experimental observables by

$$\rho = \frac{(P_0 + P_1)_I \sigma_0 + (P_0 - P_1)_{R_y(-\pi/2)} \sigma_x + (P_0 - P_1)_{R_x(\pi/2)} \sigma_y + (P_0 - P_1)_I \sigma_z}{2}.$$
 (6.30)

To be more specific to our neutral atom experiments, $R_x(\theta)$ corresponds to a ground Rabi pulse of t with $\theta = \Omega_R t$, $R_z(\theta)$ corresponds to a free precession of time t with $\theta = \Delta_{AC} t$, and $R_y(\theta) = 0$

$$R_z(\frac{\pi}{2})R_x(\theta)R_z(-\frac{\pi}{2}).$$

Due to experimental uncertainties and errors, a simple appliance of Equation 6.30 may not produce a physically valid density matrix. Instead, a maximum likelihood estimator method is often used to reconstruct ρ .

We did the state tomography for the initialized state after optical pumping, $|1\rangle = |F = 4, m_F = 0\rangle$. The measured density matrix reconstructed from maximum likelihood is

$$\rho_{\text{meas}} = \begin{pmatrix} 0.13 & 0.30 - 0.12i \\ 0.30 + 0.12i & 0.84 \end{pmatrix}. \tag{6.31}$$

The calculated fidelity measures with respect to $ho_{\mathrm{id}}=\left(\begin{array}{cc}0&0\\0&1\end{array}\right)$ are

$$F_{\rm O}^{1/2} = \text{Tr} \left[\sqrt{\sqrt{\rho_{\rm meas}} \rho_{\rm id} \sqrt{\rho_{\rm meas}}} \right] = 0.92,$$

$$F_{\rm O} = \text{Tr}^2 \left[\sqrt{\sqrt{\rho_{\rm meas}} \rho_{\rm id} \sqrt{\rho_{\rm meas}}} \right] = 0.84,$$

$$F_{\rm D} = 1 - \frac{1}{2} \text{Tr} \left[\sqrt{(\rho_{\rm id} - \rho_{\rm meas})^{\dagger} (\rho_{\rm id} - \rho_{\rm meas})} \right] = 0.64.$$
(6.32)

6.7.2 Process Tomography

A quantum operation is a process that maps a quantum state ρ to an output state $E(\rho)$. If we choose a set of operators O_i , $i=1,...,d^2$ and $d=2^n$ for n qubit gates, which form a basis for the set of any operator on the state space, then a quantum process on a qubit can be represented by a χ matrix,

$$E(\rho) = \sum_{jk} \chi_{jk} O_j \rho O_k^{\dagger}. \tag{6.33}$$

Experimentally, the quantum process can be characterized by performing quantum state tomography on $E(\rho_j)$ for a basis set of input states. For the single qubit gate process tomography, the experimental sequence is performing state tomography after applying the gate on 4 different input states from the set $\{|0\rangle, |1\rangle (|0\rangle + |1\rangle)/\sqrt{2}, (|0\rangle + i|1\rangle)/\sqrt{2}\}$, and we choose the expansion operators O_1, O_2, O_3, O_4 to be $\sigma_0/\sqrt{2}, \sigma_x/\sqrt{2}, \sigma_y/\sqrt{2}, \sigma_z/\sqrt{2}$. The $4 \times 4 \chi$ matrix can be reconstructed

from this complete set of measurements. Figure 6.9 shows our experimental results and Table 6.1 is a summary of the fidelities.

Table 6.1 Process tomography results for single qubit gates. The fidelity measures used are
$$F_{\rm O}^{1/2} = {\rm Tr} \left[\sqrt{\sqrt{\chi_{\rm meas}} \chi_{\rm id} \sqrt{\chi_{\rm meas}}} \right], F_{\rm O} = {\rm Tr}^2 \left[\sqrt{\sqrt{\chi_{\rm meas}} \chi_{\rm id} \sqrt{\chi_{\rm meas}}} \right], \\ F_{\rm D} = 1 - \frac{1}{2} {\rm Tr} \left[\sqrt{\left(\chi_{\rm id} - \chi_{\rm meas}\right)^\dagger \left(\chi_{\rm id} - \chi_{\rm meas}\right)} \right].$$

Gate	$F_{\mathrm{O}}^{1/2}$	F_{O}	$F_{ m D}$
$R_x(\pi)$	0.83	0.69	0.67
$R_x(\pi/2)$	0.92	0.85	0.84
$R_y(\pi)$	0.90	0.80	0.79
$R_y(\pi/2)$	0.90	0.81	0.76
$R_z(\pi/4)$	0.88	0.77	0.76
average	0.89	0.78	0.76

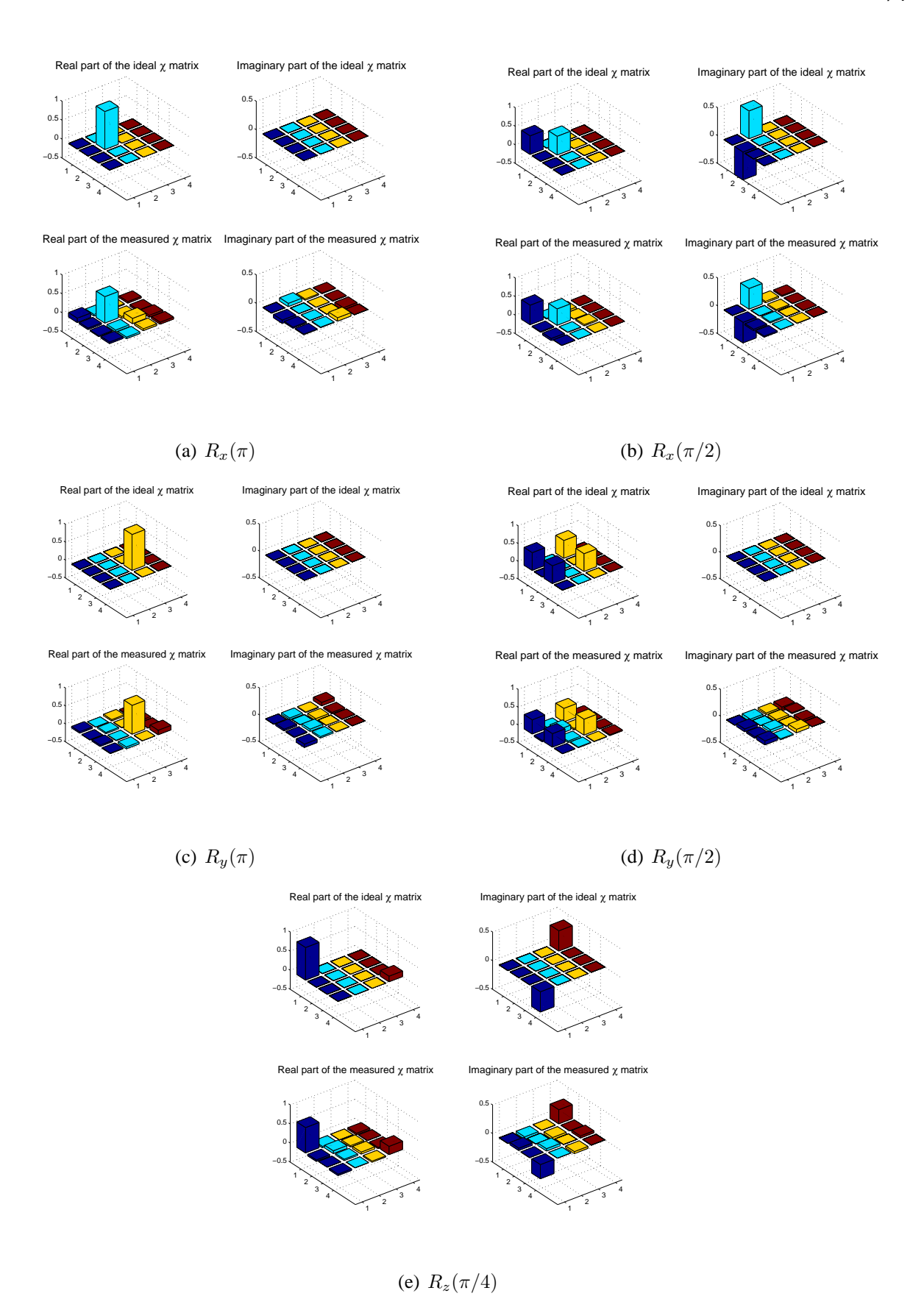


Figure 6.9 χ matrices for the process tomography of different rotation gates.

Chapter 7

Rydberg Excitation

One of the most important features of the blue detuned optical dipole traps is that they can trap ground and Rydberg state atoms simultaneously. The Raithel group have demonstrated trapping Rydberg atoms in an optical lattice by a lattice inversion immediately after laser excitation[Anderson 11]. But they only showed the trapping indirectly by the trap induced Rydberg energy shifts. In addition, with the lattice inversion method, we cannot trap ground and Rydberg state atoms simultaneously, and the inversion process could heat up the atom.

In this chapter, we will show some unambiguous measurements of trapping single Rydberg atoms in the blue detuned crossed vortex BBT.

7.1 Rabi Frequency

We use a two photon transition to excite the Cs to a Rydberg state. In the preliminary experiments, we use a D state because it has a larger dipole moment and easier to detect compared with a S state. The atomic levels involved are shown in Figure 7.1.

With the polarization setting as in Figure 7.1, the Rabi frequency could be calculated as

$$\begin{split} \Omega_R = & \frac{e^2}{\hbar^2} \frac{\langle 7P_{1/2}, F = 4, m_F = m_{F,g} + 1 | E_1 r_1 | 6S_{1/2}, F = 4, m_{F,g} \rangle \langle 61D_{3/2}, m_J | E_2 r_{-1} | 7P_{1/2}, F = 4, m_F = m_{F,g} + 1 \rangle}{2\Delta} \\ + & \frac{e^2}{\hbar^2} \frac{\langle 7P_{1/2}, F = 3, m_F = m_{F,g} + 1 | E_1 r_1 | 6S_{1/2}, F = 4, m_{F,g} \rangle \langle 61D_{3/2}, m_J | E_2 r_{-1} | 7P_{1/2}, F = 3, m_F = m_{F,g} + 1 \rangle}{2(\Delta + \Delta_{hf,7P_{1/2}})} \\ = & \frac{\Omega_{1,0} \Omega_{2,0}}{2\Delta} \left(\frac{\Delta}{\Delta + \Delta_{hf,7P_{1/2}}} c_3 + c_4 \right) \end{split}$$

(7.1)

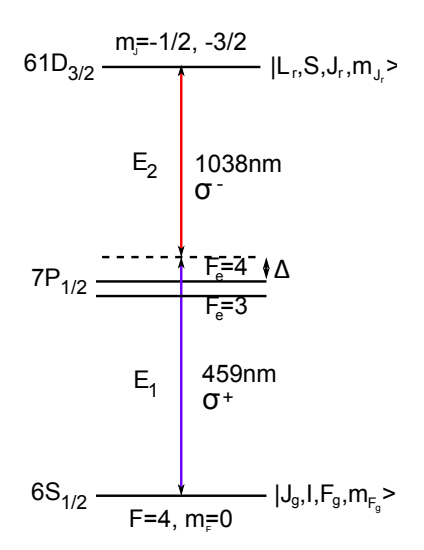


Figure 7.1 Two photon excitation of Cs Rydberg state.

where
$$\Omega_{1,0} = ea_0 E_1 \langle 7P_{1/2} || r || 6S_{1/2} \rangle / \hbar$$
, $\Omega_{2,0} = ea_0 E_2 \langle 61D_{3/2} || r || 7P_{1/2} \rangle / \hbar$.
$$c_{F_e} = \sum_{p,q=-1,0,1} a_{1,p} a_{2,q} c_{hf} (J_g, I, F_g, m_{F_g}; J_e, I, F_e, m_{F_e} = m_{F_1} + p; p)$$

$$\left(\sum_{m_{J_e}} C_{J_e, m_{J_e}; I, m_{F_e} - m_{J_e}}^{F_e, m_{F_e}} c_{fs} (L_e, S, J_e, m_{J_e}; L_r, S, J_r, m_{J_r}; q) \right)$$

$$(7.2)$$

$$\Delta_{ac} = \frac{e^2}{\hbar^2} \frac{|\langle 61D_{3/2}, m_J | E_2 r_{-1} | 7P_{1/2}, F = 4, m_F = m_{F,g} + 1 \rangle|^2 - |\langle 7P_{1/2}, F = 4, m_F = m_{F,g} + 1 | E_1 r_1 | 6S_{1/2}, F = 4, m_{F,g} \rangle|^2}{4\Delta} + \frac{e^2}{\hbar^2} \frac{|\langle 61D_{3/2}, m_J | E_2 r_{-1} | 7P_{1/2}, F = 3, m_F = m_{F,g} + 1 \rangle|^2 - |\langle 7P_{1/2}, F = 3, m_F = m_{F,g} + 1 | E_1 r_1 | 6S_{1/2}, F = 4, m_{F,g} \rangle|^2}{2(\Delta + \Delta_{hf,7P_{1/2}})}$$

$$(7.3)$$

Figure 7.2 shows a sample calculation of Rabi frequency and AC Stark shift of two photon excitation to $61D_{3/2}$ Rydberg state, using the scheme in Figure 7.1. For a large detuning, the Rabi frequency of $m_J = -3/2$ is much smaller than that of $m_J = -1/2$, so we will consider only the $m_J = -1/2$ Rydberg state from now on.

7.2 TPS and RFE

The TPS scan in Figure 7.3 is done with the following laser settings: the detuning $\Delta/2\pi=2{\rm GHz}$, 459nm laser power $P_{459}=60\sim70\mu{\rm W}$, waist size $w_{459}=6\mu{\rm m}$,

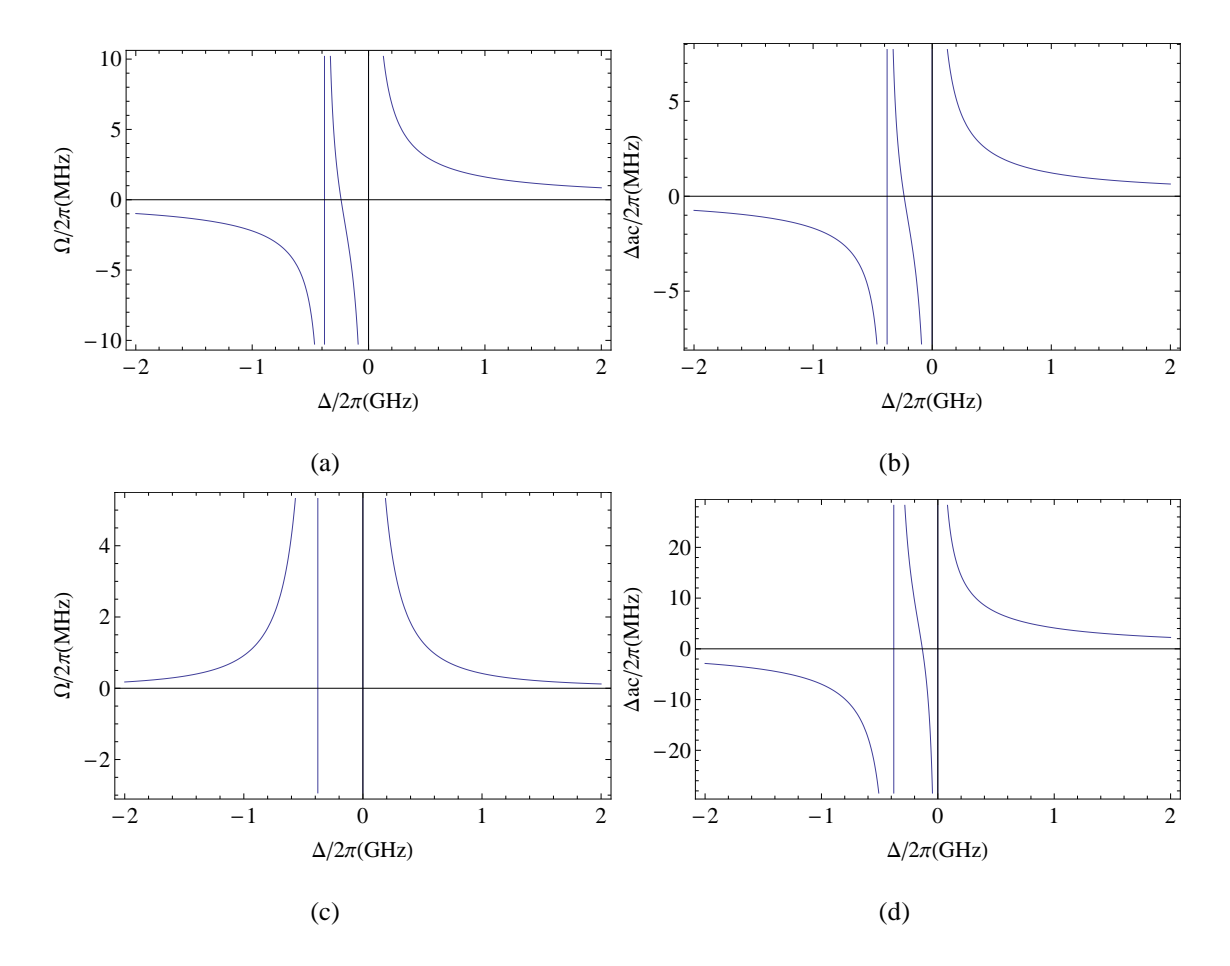


Figure 7.2 Calculated Rabi frequency and AC Stark shift of two photon excitation to $61D_{3/2}$ Rydberg state via $7P_{1/2},\,P_{459}=65\mu\mathrm{W},\,w_{459}=6\mu\mathrm{m},\,P_{1038}=3.5\mathrm{mW},\,w_{1038}=2.8\mu\mathrm{m},\,$ $\Delta/2\pi=2\mathrm{GHz}$, (a)(b) $m_J=-1/2$, (c)(d) $m_J=-3/2$.

1038nm laser power $P_{1038}=3\sim 4 \mathrm{mW}$, waist size $w_{1038}=2.8 \mu \mathrm{m}$, so that the calculated Rabi frequency $\Omega/2\pi=0.76\sim 0.94 \mathrm{MHz}$, and AC Stark shift $\Delta_{AC}/2\pi=0.54\sim 0.75 \mathrm{MHz}$.

The measured frequency is summarized in Table 7.1. The measured value is $14.4 \sim 13.8$ MHz above theory[Weber 87]. To account for the difference, we consider all the possible frequency shifts:

- 1)Zeeman shift in the 0.7G bias field for $61D_{3/2}$, $m_J = -1/2$ is $0.56 \text{MHz/G} \times 0.7 \text{G} = 0.4 \text{MHz}$;
- 2)AC Stark shift $\Delta_{AC}/2\pi = 0.54 \sim 0.75 \text{MHz}$;
- 3)green bottle trap shift is about $\Delta_{bob} = 0.34 \text{MHz}$;
- 4)differential dipole shift induced by the strong 1038nm laser, $U=-\frac{2\pi 10^{-6}}{c}(\alpha_{cgs,1038,r}-\alpha_{cgs,1038,g})I_{1038}=2.0\sim2.7 \mathrm{MHz}$, where the polarizability $\alpha_{cgs,1038,r}=-76.9 \mathrm{A}^3$ for Rydberg states, and $\alpha_{cgs,1038,g}=187 \mathrm{A}^3$ for ground states.

These four factors add to $3.27 \sim 4.18 \mathrm{MHz}$. So our measured transition frequency is about $9.61 \sim 11.12 \mathrm{MHz}$ higher than the theoretical value.

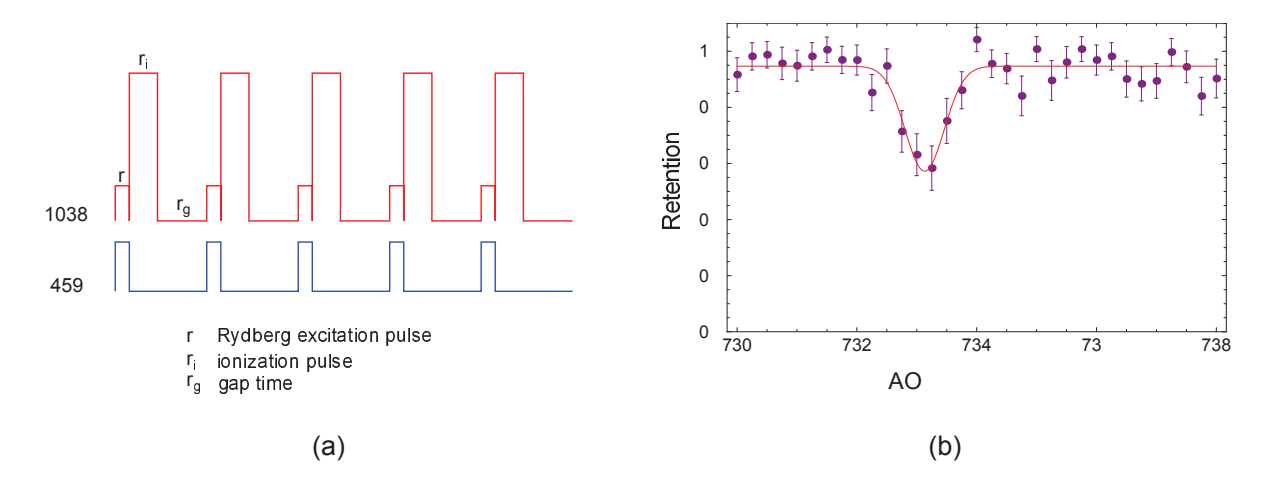


Figure 7.3 TPS scan of Cs Rydberg state $61D_{3/2}$. (a)pulse sequence for detecting Rydberg state with 1038nm laser photoionization, in which Rydberg excitation pulse $r=0.6\mu\mathrm{s}$, high power 1038 ionization pulse $r_i=2\mu\mathrm{s}$, and a gap time of $r_g=10\mu\mathrm{s}$ is used to enhance retention. (b)TPS curve, with $f_{center}=733.131\pm0.043\mathrm{MHz}$, half line width $df=0.768\mathrm{MHz}$.

The RFE is measured with the same setting as the TPS experiment in Figure 7.3, with AOM frequency set at 733.2 MHz, shown in Figure 7.4. The measured Rabi frequency is 0.4 MHz, as compared with $0.76 \sim 0.94$ MHz from calculations. The discrepancy could be due to that the

Table 7.1 Measurement of transition frequency (in GHz) of $|6S_{1/2}, F = 4, m_F = 0\rangle \rightarrow |61D_{3/2}, m_J = -1/2\rangle$.

f_{918}	f_{1038}	$f_{918,AOM}$	$f_{gr,measured}$	$f_{gr,theory}$	$f_{gr,measured} - f_{gr,theory}$
326254.058029	288071.054	$-0.7331 \sim -0.7334$	940577.70438 ~	940577.690	$0.0144 \sim 0.0138$
			940577.70378		

beams are slightly misaligned so the atom does not see the peak intensity, or the laser frequency is off. In this experiment, the Rydberg state is detected by a single high power 1038nm photoionization pulse, and the detection or excitation amplitude is 27%.

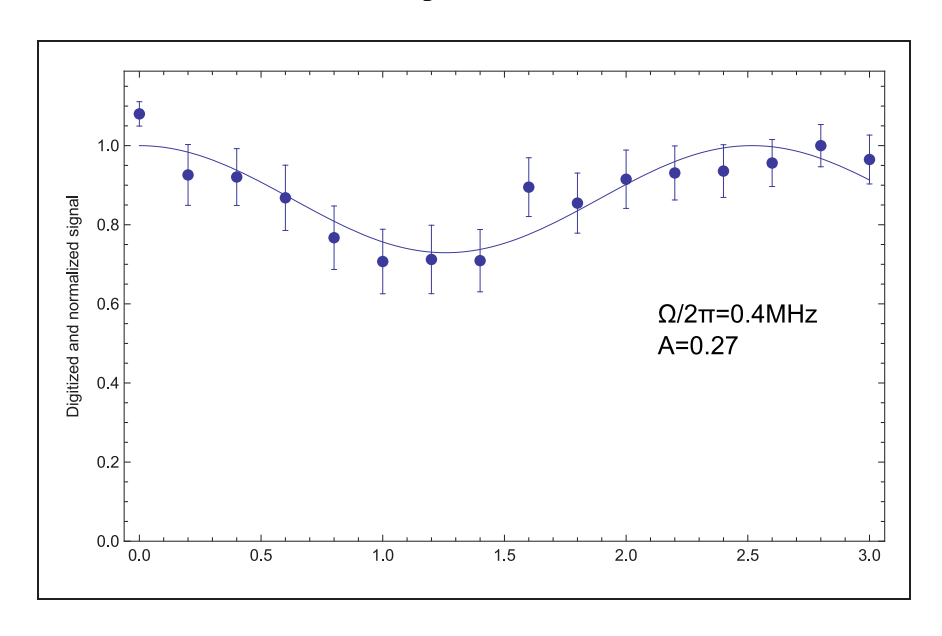


Figure 7.4 Rabi flopping between ground state $6S_{1/2}$, F=4, $m_F=0$ and Rydberg state $61D_{3/2}$, $m_J=-1/2$.

7.3 Photoionization Rate

In the experiments, we initially used high power 1038nm light to photoionization the Rydberg atom as the state detection method. Then we used a high intensity 852nm beam to blow away the ground state atom to detect Rydberg states. It is helpful to estimate the photoionization rate of the Rydberg atom under these high intensity lasers. The photoionization cross section for a beam of

wavelength λ is

$$\sigma = \frac{4\pi^2 hc}{3\lambda \alpha m_e c^2} \sum_{E=E_r + \hbar \omega, L} \frac{L_{>}}{2L_r + 1} |R_r^{L,E}|^2$$
(7.4)

where the radial integral between the Rydberg state Ψ_r and the continuum state $\phi_{L,E}$ is $R_r^{L,E} = \int \Psi_r(r) r \phi_{L,E}(r) r^2 dr$, and L_r is the larger of L_r and L. The results are in Figure 7.5. The cross

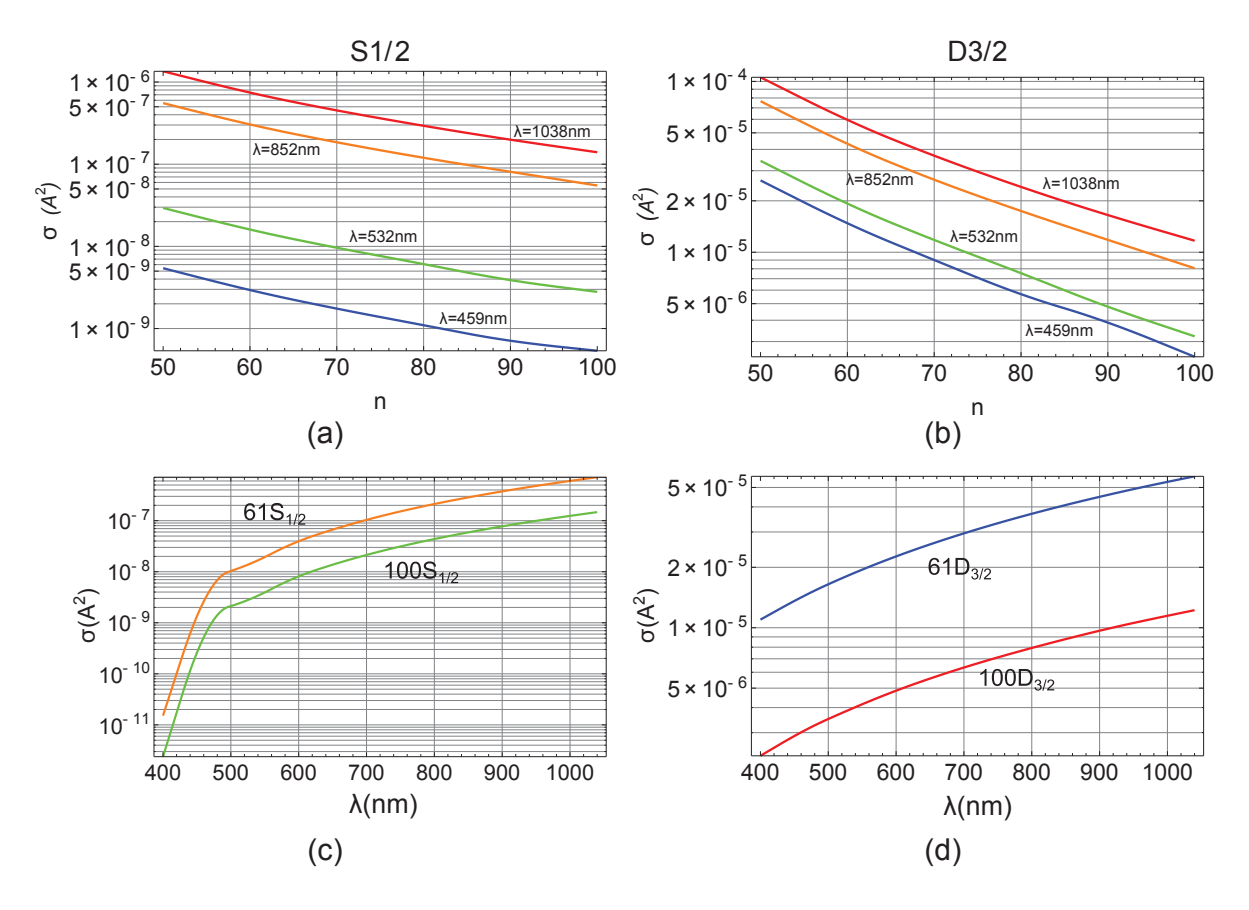


Figure 7.5 Cross section of photoionization of Cs Rydberg states.

section of 1038nm photoionization for $61D_{3/2}$ is about $6 \times 10^{-5}A^2$. So for the 75mW high power 1038 pulse we were using, the ionization rate is about 19kHz. If a 2μ s pulse is used, the possibility of photoionization is about 4%. The detection efficiency in Figure 7.4 is more than that because there is also strong dipole force on the Rydberg atom resulting in mechanical atom loss. So photoionization using 1038nm laser is not a very effective way of detecting the Rydberg atoms.

In the following experiments, we used a strong resonant 852nm beam to blow away ground state atoms. The beam power is about 0.4mW and it is focused to a waist size about 100μ m, so the

photoionization rate and mechanical force are reduced to $I_{852}/I_{1038}=4\times10^{-6}$ of those when using the 1038 beam. With this method, we got a cleaner signal and a detection efficiency about 40%.

Another interesting point to notice is that, if we look at the photoionization cross sections for a broader range of wavelengths in Figure 7.6, we can find minima of photoionization for Rydberg states $S_{1/2}$ and $D_{3/2}$. These minima are called Cooper minima[Beterov 12]. These minima arise from the cancellation of the radial integral for some transitions, depending on the overlap between the wavefunctions of the initial and final quantum states of the atoms. An example is shown in Figure 7.7. The relative radial matrix element R_{rel} in Figure 7.7(a) is defined as

$$R_{rel}(E_n L \to E' L') = \frac{R(E_n L \to E' L') \times (-2E_n)^{-3/4} \times |E' - E_n|^{5/3}}{0.418},$$
(7.5)

which varies more slowly with n than the radial matrix element.

The results are quite different from the data calculated in [Beterov 12]. In the calculations of the $S_{1/2} \to P_{1/2}$ bound-free matrix element, our results show a single minimum near $E_2 = 0.12$ a.u., while in [Beterov 12], there are two minima at around $E_2 = 0.06$ and 0.16 a.u., and the numerical values are quite different (maximum is 0.25 in our plot and 0.6 in Figure 6(a) of [Beterov 12]). We are using two different computation methods. The discrepancy may result from the possible fact that one of the methods does not work well for bound-free matrix element calculations.

7.4 Rydberg Energy Shift in Bottle Beam Trap

With the ponderomotive potential theory in Chapter 3, we calculated the energy shift of Rydberg states in the crossed vortex BBT, in Figure 7.8, with the actual experimental bottle beam parameters. For state $|61D_{3/2}, m_J = -1/2\rangle$, the shift is 0.34MHz.

To measure the energy shift in the BBT, we took the two photon spectra of Cs $61D_{3/2}$ with the trap on and off consecutively (Figure 7.9), by scanning the RF frequency of the 918 laser double pass AOM. The Rydberg atoms are detected by blowing away the ground state atoms. The transition frequency with trap on is (0.033+/-0.05)x4=0.13+/-0.2 MHz higher than the frequency with trap

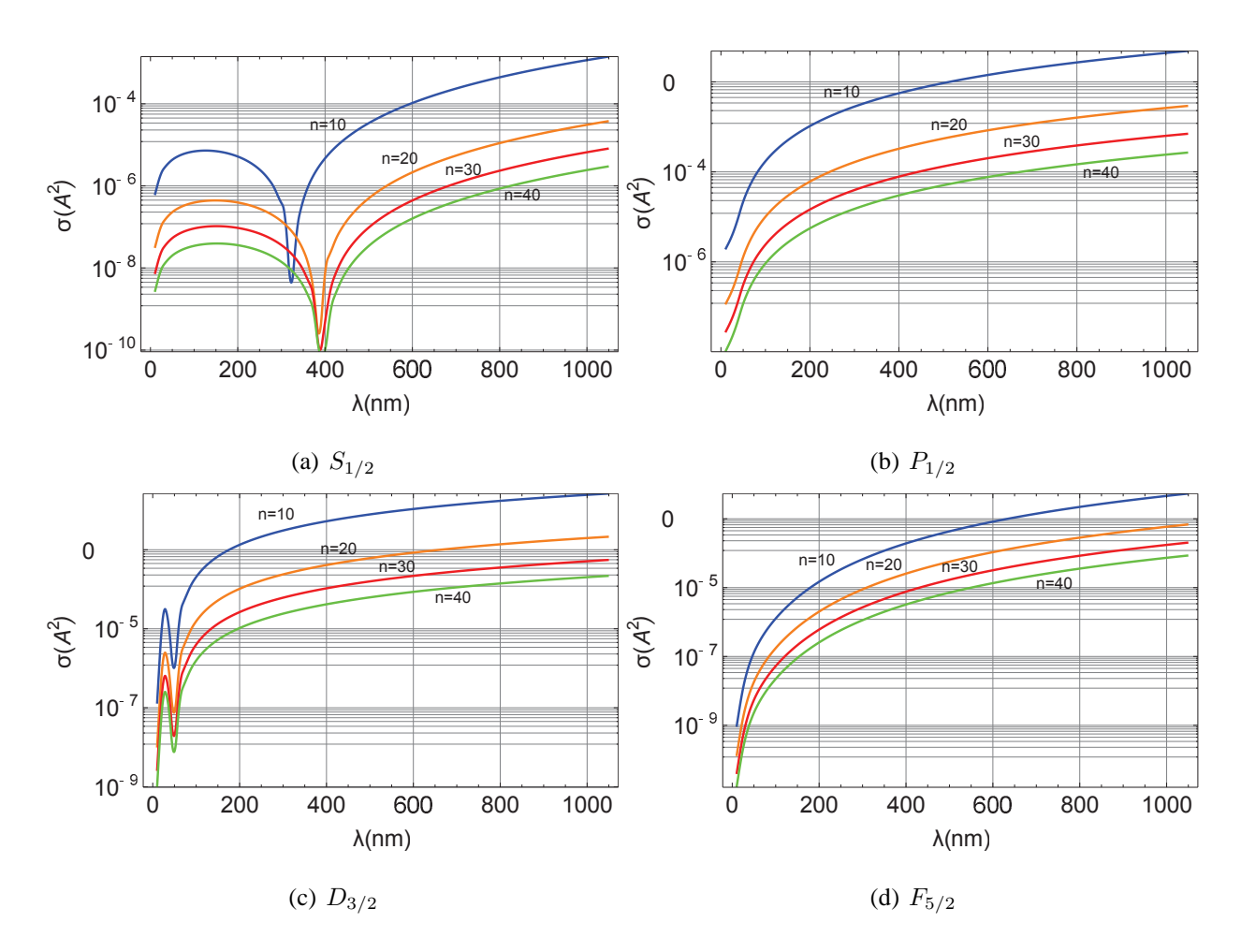


Figure 7.6 Cross section of photoionization of Cs Rydberg states for different wavelengths.

off. The theoretical value 0.34MHz is right on the edge of experimental uncertainty range. More data points with different *n*s are needed before any conclusion can be made.

7.5 Rydberg Lifetime

7.5.1 Decay of Rydberg States

The decay of Rydberg states is mainly due to spontaneous decay and black body radiation (BBR) induced decay. The effective lifetime could be estimated by [Beterov 09]

$$\tau_{eff} = \left(\frac{1}{\tau_0} + \Gamma_{BBR}\right)^{-1} \tag{7.6}$$

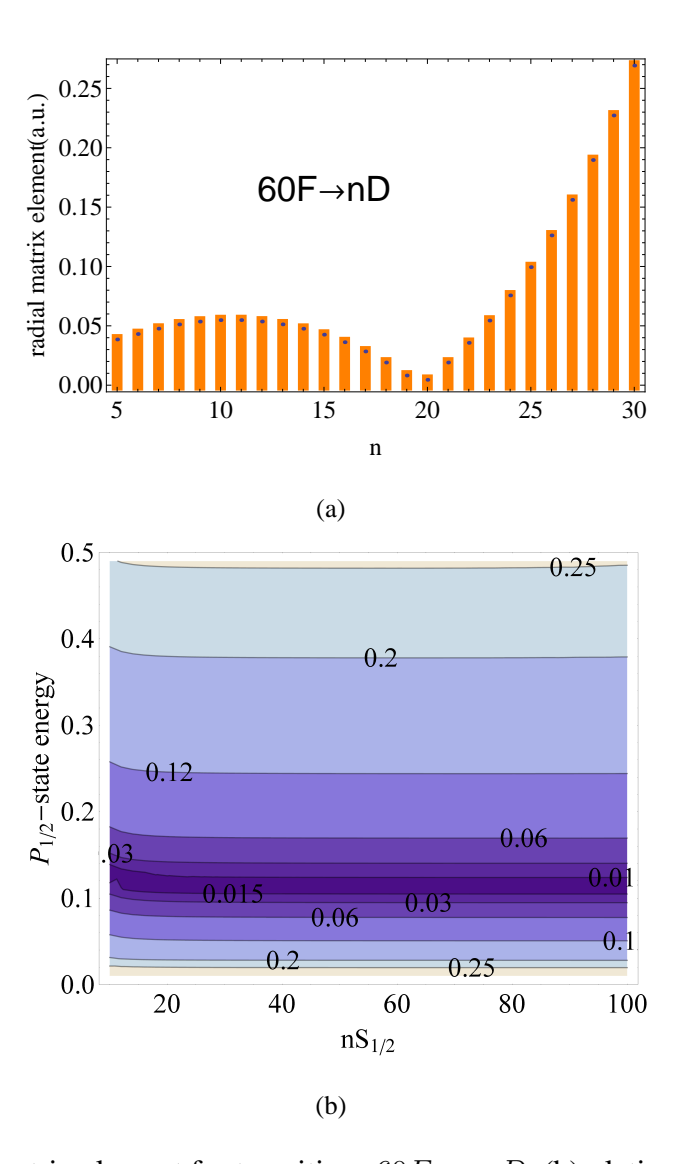


Figure 7.7 (a)Radial matrix element for transitions $60F \rightarrow nD$, (b)relative radial matrix element for transitions from $nS_{1/2}$ bound states to $P_{1/2}$ free states.

The spontaneous decay lifetime τ_0 , and the BBR induced decay rate Γ_{BBR} can be estimated by the semiempirical formula

$$\tau_0 = \tau_s n_{eff}^{\sigma}$$

$$\Gamma_{BBR} = \frac{A}{n_{eff}^D} \frac{2.14 \times 10^{10}}{\exp(315780B/n_{eff}^C T) - 1} (s^{-1})$$
(7.7)

where $n_{eff}=n-\delta_{qd}$ is the effective quantum number with δ_{qd} the quantum defect number. The parameters for Cs are listed in Tab. 7.2. $\tau_{61d_{3/2}}=78.5\mu s$.

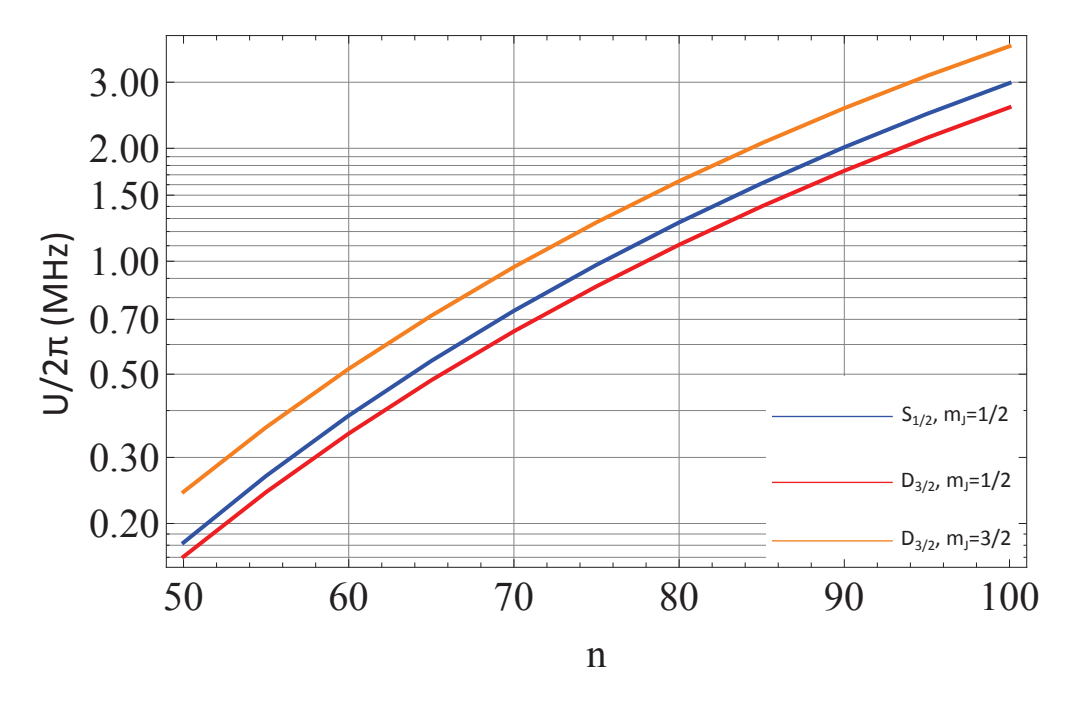


Figure 7.8 Ponderomotive energy shift of Rydberg states in the crossed vortex BBT, with trap parameters λ =532nm, d=6mm, f=34mm, $w_0 = 3\mu$ m, P=0.4W.

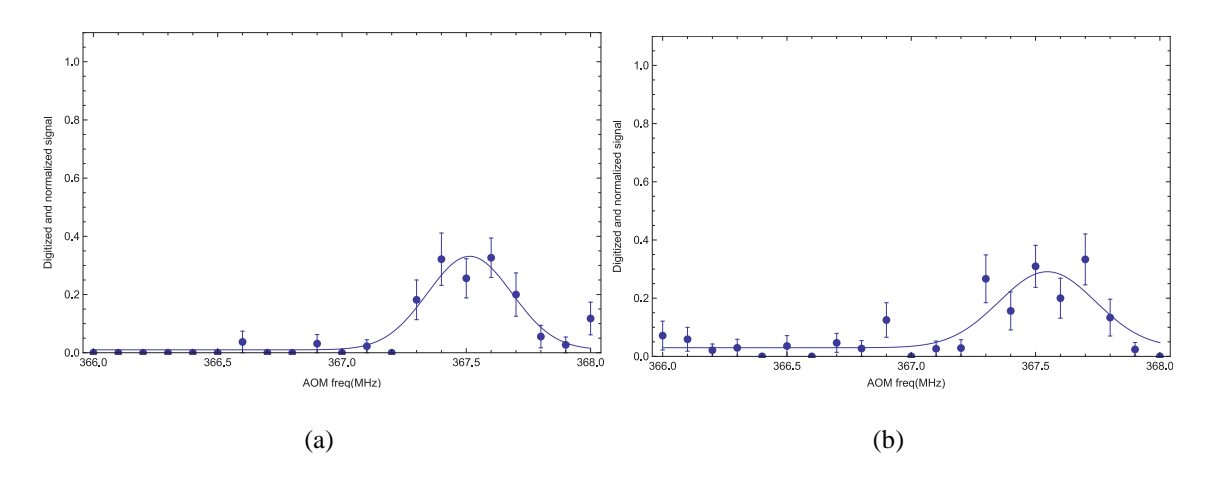


Figure 7.9 Two photon spectrum of Cs $61D_{3/2}$, (a)with the BBT on, $f_{center}=367.514\pm0.02 \mathrm{MHz}$; (b)with BBT off, $f_{center}=367.547\pm0.03 \mathrm{MHz}$.

Figure 7.15 shows the lifetime estimates of Cs Rydberg states.

	$S_{1/2}$	$P_{1/2}$	$P_{3/2}$	$D_{3/2}$	$D_{5/2}$			
$ au_s(\mathrm{ns})$	1.2926	2.9921	3.2849	0.6580	0.6681			
σ	3.0005	2.9892	2.9875	2.9944	2.9941			
A	0.123	0.041	0.038	0.038	0.036			
В	0.231	0.072	0.056	0.076	0.073			
C	2.517	1.693	1.552	1.790	1.770			
D	4.375	3.607	3.505	3.656	3.636			
700								
600								

Table 7.2 Scaling coefficients of Cs in Equation 7.7, data taken from [Beterov 09].

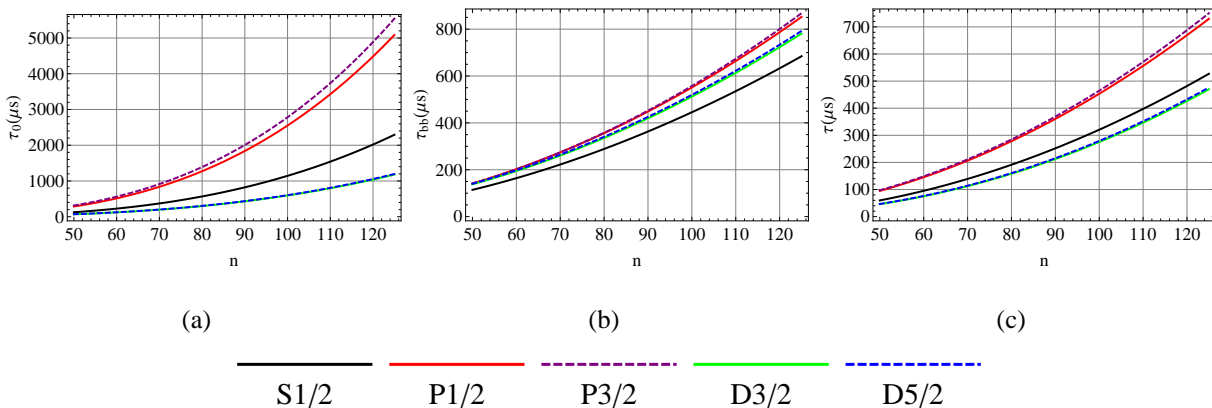


Figure 7.10 Lifetime of Rydberg states, (a)0K lifetime, (b)blackbody lifetime at 300K, (c)lifetime at 300K.

Model of Rydberg Atom Loss with Multiple Rydberg Ionization Pulses 7.5.2

Suppose the Rydberg atom decays at a rate of Γ_r , the loss rate from the 1038 high power blow away beam is Γ_{1038} (either from photoionization or mechanical pushing), the loss rate from the 532nm BoB is Γ_{bob} (either from photoionization or not trapping, as shown in Figure 7.11. Then the Rydberg population P_r and ground state population P_g change with time according to

$$\frac{dP_r}{dt} = -(\Gamma_r + \Gamma_{bob} + \Gamma_{1038})P_r \tag{7.8}$$

$$\frac{dP_r}{dt} = -(\Gamma_r + \Gamma_{bob} + \Gamma_{1038})P_r$$

$$\frac{dP_g}{dt} = \Gamma_r P_r$$
(7.8)

The solution is

$$P_r(t) = P_r(t=0)e^{-(\Gamma_r + \Gamma_{bob} + \Gamma_{1038})t}$$
(7.10)

$$P_{r}(t) = P_{r}(t=0)e^{-(\Gamma_{r}+\Gamma_{bob}+\Gamma_{1038})t}$$

$$P_{g}(t) = \frac{\Gamma_{r}}{\Gamma_{r}+\Gamma_{bob}+\Gamma_{1038}} (1-e^{-(\Gamma_{r}+\Gamma_{bob}+\Gamma_{1038})t})P_{r}(t=0) + P_{g}(t=0)$$
(7.10)

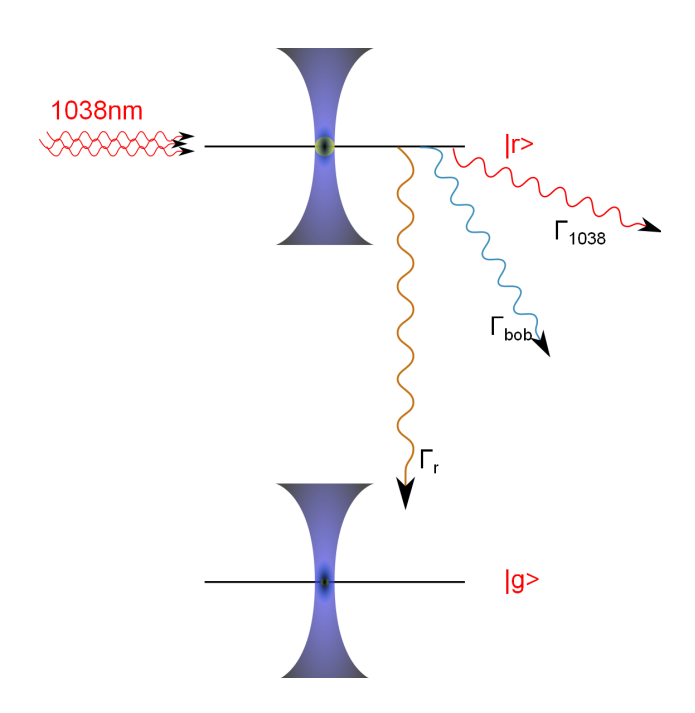


Figure 7.11 Model of Rydberg atom decay and loss.

Let us consider the pulse sequence in Figure 7.3(a). To simplify the model, suppose after each Rydberg excitation pulse, the atom is at the Rydberg state with a fixed probability $P_{r,0}$. So

$$P_r(t=0) = P_{r,0} (7.12)$$

$$P_g(t=0) = P_{g,0} = 1 - P_{r,0}$$
 (7.13)

Define $\Gamma_1 \equiv \Gamma_r$, $\Gamma_2 \equiv \Gamma_r + \Gamma_{bob}$, and $\Gamma_3 \equiv \Gamma_r + \Gamma_{bob} + \Gamma_{1038}$. After the first high power ionization pulse

$$P_r(t = r_i) = P_{r,0}e^{-\Gamma_3 r_i} (7.14)$$

$$P_g(t=r_i) = \frac{\Gamma_1}{\Gamma_3} (1 - e^{-\Gamma_3 r_i}) P_{r,0} + P_{g,0}$$
 (7.15)

after the gap time r_g ,

$$P_{r}(t = r_{i} + r_{g}) = e^{-\Gamma_{3}r_{i} - \Gamma_{2}r_{g}} P_{r,0}$$

$$P_{g}(t = r_{i} + r_{g}) = \frac{\Gamma_{1}}{\Gamma_{2}} (1 - e^{-\Gamma_{2}r_{g}}) P_{r}(t = r_{i}) + P_{g}(t = r_{i})$$

$$= \frac{\Gamma_{1}}{\Gamma_{2}} (1 - e^{-\Gamma_{2}r_{g}}) e^{-\Gamma_{3}r_{i}} P_{r,0} + \frac{\Gamma_{1}}{\Gamma_{3}} (1 - e^{-\Gamma_{3}r_{i}}) P_{r,0} + P_{g,0}$$

$$= -\frac{\Gamma_{r}}{\Gamma_{2}} e^{-\Gamma_{3}r_{i} - \Gamma_{2}r_{g}} P_{r,0} + \frac{\Gamma_{r}\Gamma_{1038}}{\Gamma_{2}\Gamma_{3}} e^{-\Gamma_{3}r_{i}} P_{r,0} - \frac{\Gamma_{bob} + \Gamma_{1038}}{\Gamma_{3}} P_{r,0} + 1$$

$$P_{t}(t = r_{i} + r_{g}) = \frac{\Gamma_{bob}}{\Gamma_{2}} e^{-\Gamma_{3}r_{i} - \Gamma_{2}r_{g}} P_{r,0} + \frac{\Gamma_{r}\Gamma_{1038}}{\Gamma_{2}\Gamma_{3}} e^{-\Gamma_{3}r_{i}} P_{r,0} - \frac{\Gamma_{bob} + \Gamma_{1038}}{\Gamma_{3}} P_{r,0} + 1$$

After 5 repetitions,

$$P_r(t = 5r_i + 5r_g) = (P_t(t = r_i + r_g))^4 P_r(t = r_i + r_g)$$

$$P_g(t = 5r_i + 5r_g) = (P_t(t = r_i + r_g))^4 P_g(t = r_i + r_g)$$

$$P_t(t = 5r_i + 5r_g) = (P_t(t = r_i + r_g))^5$$
(7.17)

What is left on the ground state eventually is

$$P_{g,5}(t=\infty) = \frac{\Gamma_r}{\Gamma_2} P_r(t=5r_i+5r_g) + P_g(t=5r_i+5r_g)$$

$$= \frac{\Gamma_r}{\Gamma_2} (P_t(t=r_i+r_g))^4 P_r(t=r_i+r_g) + (P_t(t=r_i+r_g))^4 P_g(t=r_i+r_g)$$
(7.18)

If we are using one pulse repetition

$$P_{g,1}(t=\infty) = \frac{\Gamma_r}{\Gamma_2} P_r(t=r_i+r_g) + P_g(t=r_i+r_g)$$

$$= \frac{\Gamma_r \Gamma_{1038}}{\Gamma_2 \Gamma_3} e^{-\Gamma_3 r_i} P_{r,0} - \frac{\Gamma_{bob} + \Gamma_{1038}}{\Gamma_3} P_{r,0} + 1$$
(7.19)

If the blowaway r_i is applied after the gap time r_g ,

$$P_r(t = r_g) = P_{r,0}e^{-\Gamma_2 r_g}$$

$$P_g(t = r_g) = \frac{\Gamma_1}{\Gamma_2} (1 - e^{-\Gamma_2 r_g}) P_{r,0} + P_{g,0}$$
(7.20)

$$P_{r}(t = r_{g} + r_{i}) = e^{-\Gamma_{2}r_{g} - \Gamma_{3}r_{i}} P_{r,0}$$

$$P_{g}(t = r_{g} + r_{i}) = \frac{\Gamma_{1}}{\Gamma_{3}} (1 - e^{-\Gamma_{3}t_{i}}) e^{-\Gamma_{2}r_{g}} P_{r,0} + \frac{\Gamma_{1}}{\Gamma_{2}} (1 - e^{-\Gamma_{2}r_{g}}) P_{r,0} - P_{r,0} + 1$$

$$= -\frac{\Gamma_{r}}{\Gamma_{3}} e^{-\Gamma_{2}r_{g} - \Gamma_{3}r_{i}} P_{r,0} - \frac{\Gamma_{r}\Gamma_{1038}}{\Gamma_{2}\Gamma_{3}} e^{-\Gamma_{2}r_{g}} P_{r,0} - \frac{\Gamma_{bob}}{\Gamma_{2}} P_{r,0} + 1$$

$$P_{t}(t = r_{g} + r_{i}) = \frac{\Gamma_{bob} + \Gamma_{1038}}{\Gamma_{2}} e^{-\Gamma_{2}r_{g} - \Gamma_{3}r_{i}} P_{r,0} - \frac{\Gamma_{r}\Gamma_{1038}}{\Gamma_{2}\Gamma_{3}} e^{-\Gamma_{2}r_{g}} P_{r,0} - \frac{\Gamma_{bob}}{\Gamma_{2}} P_{r,0} + 1$$

$$(7.21)$$

The final ground state atom probability could be again calculated with Equation 7.18.

Using this model, we fitted the experimental data to estimate different lifetimes, Figure 7.12,7.13, 7.14. The best fit parameters are $P_{r,0}=0.8$, $\tau_{bob}=392\mu\mathrm{s}$, $\tau_{1038}=15.7\mu\mathrm{s}$, assuming Rydberg decay time $\tau_r=78.5\mu\mathrm{s}$.

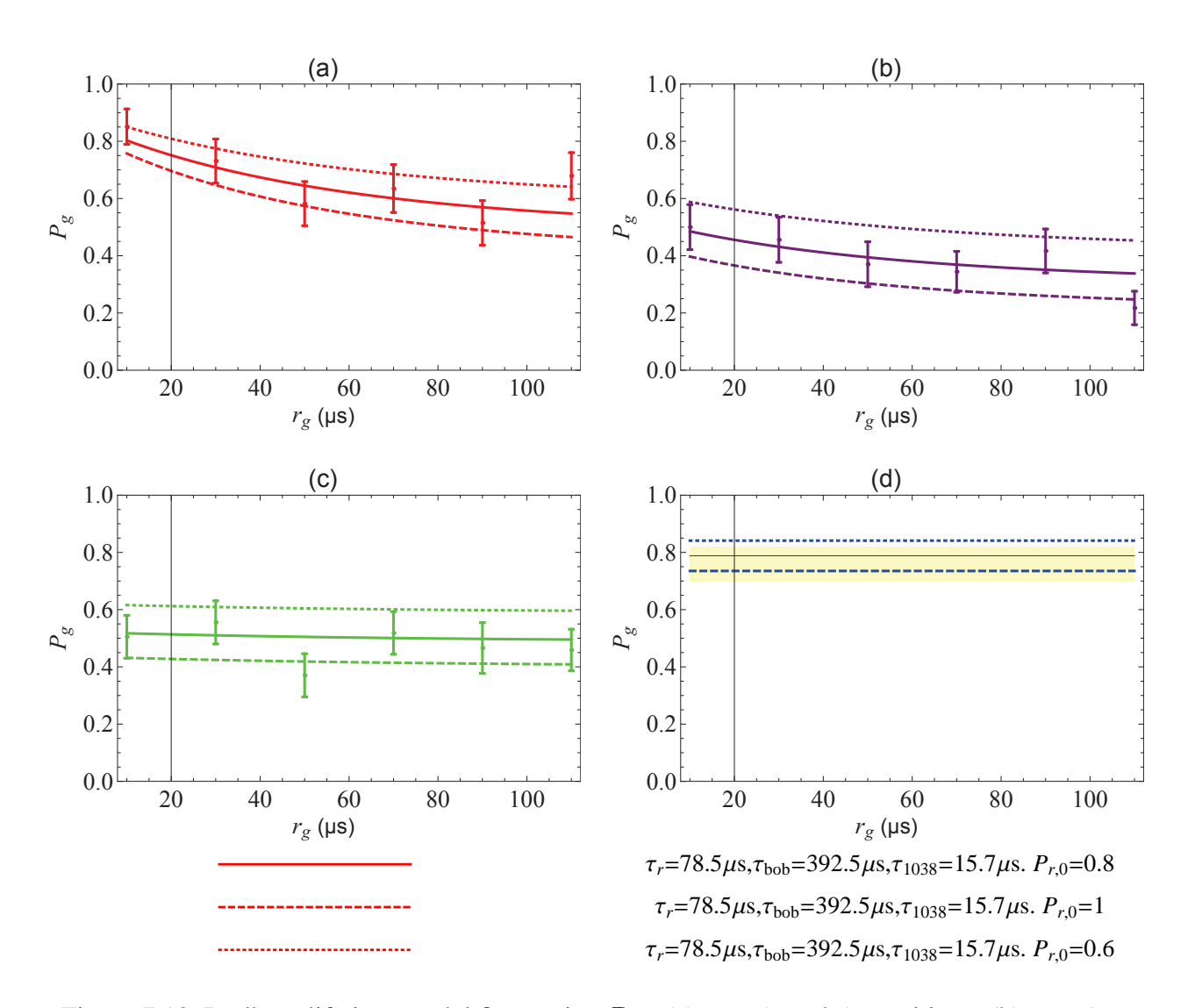


Figure 7.12 Rydberg lifetime model fit, varying $P_{r,0}$. (a) $r_i=0$, and 5 repetitions; (b) $r_i=2\mu s$, gap time r_g after 1038 pulse r_i , and 5 repetitions; (c) $r_i=2\mu s$, gap time r_g before 1038 pulse r_i , and 5 repetitions; (d) $r_i=2\mu s$, gap time r_g after 1038 pulse r_i , 1 repetition, Shade area is the experimental Rabi flopping amplitude uncertainty range.

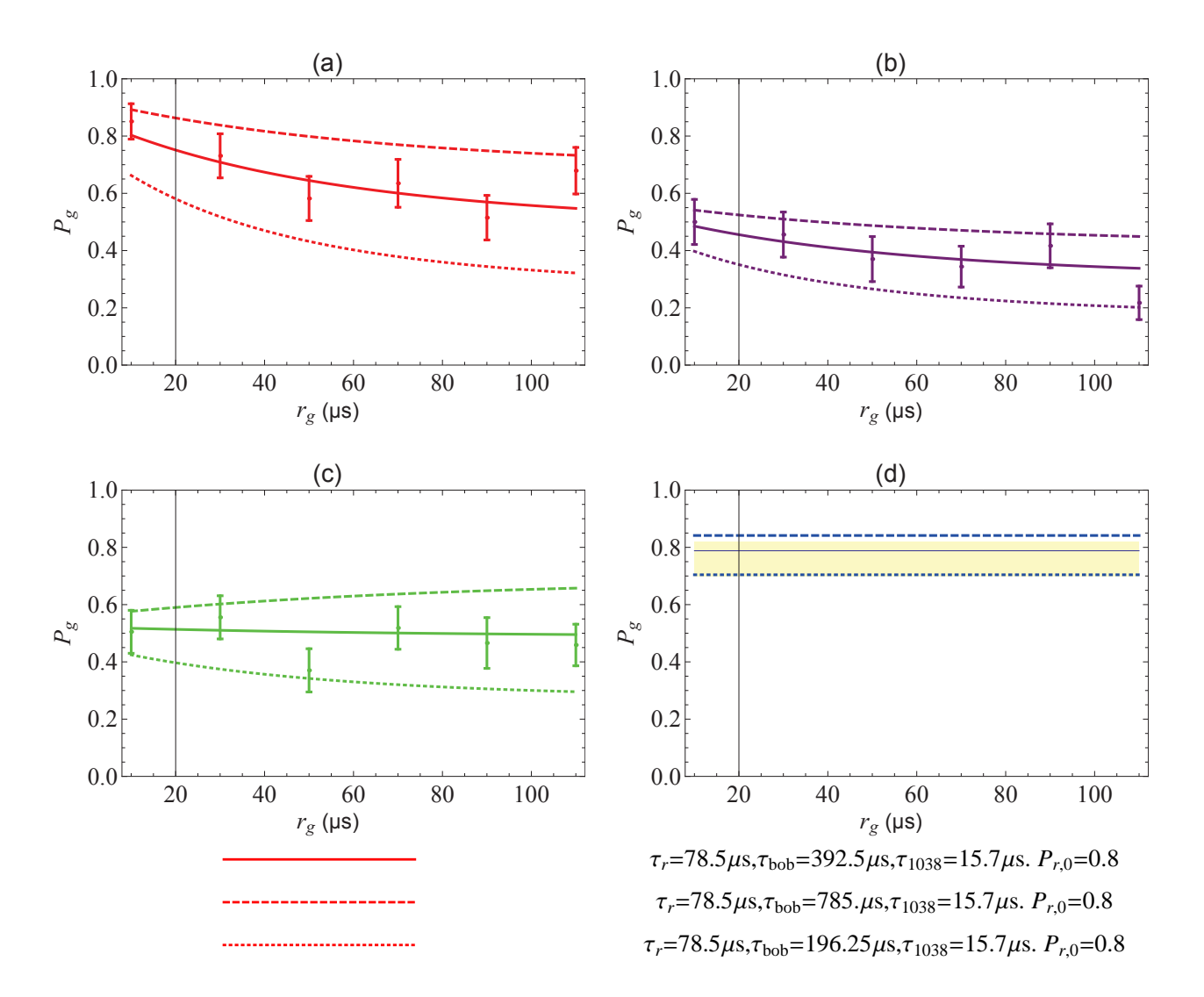


Figure 7.13 Rydberg lifetime model fit, varying $\tau_{bob}=1/\Gamma_{bob}$. (a) $r_i=0$, and 5 repetitions; (b) $r_i=2\mu s$, gap time r_g after 1038 pulse r_i , and 5 repetitions; (c) $r_i=2\mu s$, gap time r_g before 1038 pulse r_i , and 5 repetitions; (d) $r_i=2\mu s$, gap time r_g after 1038 pulse r_i , 1 repetition, Shade area is the experimental Rabi flopping amplitude uncertainty range.

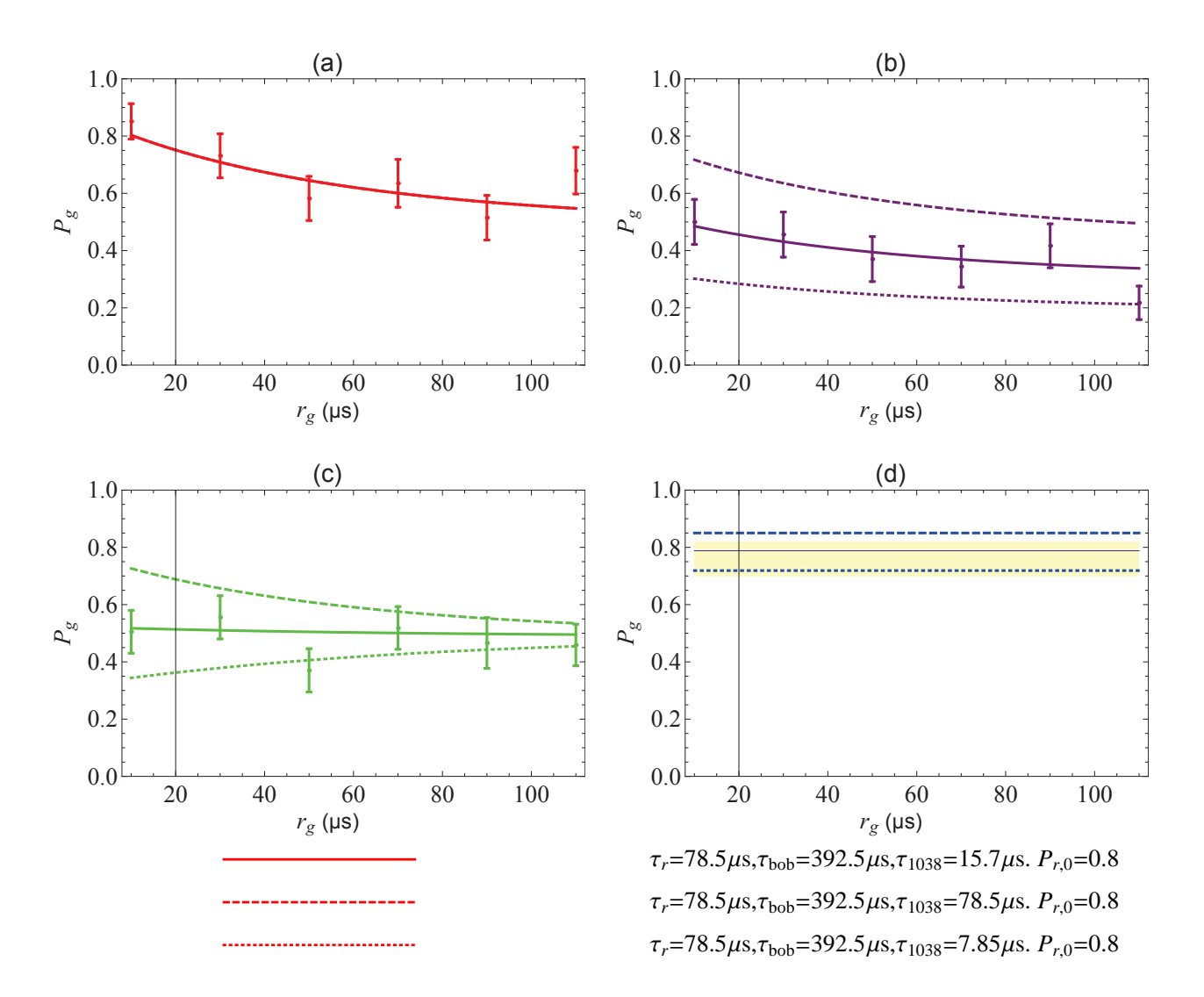


Figure 7.14 Rydberg lifetime model fit, varying $\tau_{1038}=1/\Gamma_{1038}$. (a) $r_i=0$, and 5 repetitions; (b) $r_i=2\mu {\rm s}$, gap time r_g after 1038 pulse r_i , and 5 repetitions; (c) $r_i=2\mu {\rm s}$, gap time r_g before 1038 pulse r_i , and 5 repetitions; (d) $r_i=2\mu {\rm s}$, gap time r_g after 1038 pulse r_i , 1 repetition, Shade area is the experimental Rabi flopping amplitude uncertainty range.

7.5.3 Direct Lifetime Measurement with Ground State Blowaway

Then we did a more direct measurement of the lifetime with the following pulse sequence:

1) apply a Rydberg π pulse; 2) wait for a time gap of t (with the trap on or off), at the end of which a ground state blowaway pulse of $5\mu s$ is applied to blow away the F=4 ground state atom; 3) a second π pulse is used to bring the atom back to ground state; 4) in the end, readout MOT beams are turned on to check if there is any atom left in the trap.

The results are shown in Figure 7.15. By comparing the lifetime with and without the trap, it is obvious that the bottle trap traps the Rydberg atom. One interesting point is that the lifetime with the trap on $\tau=102\pm17\mu\mathrm{s}$ is actually longer than the natural decay lifetime of $61D_{3/2}$ $\tau_r=78.5\mu\mathrm{s}$. The reason could be due to experimental errors, or the fact that the Rydberg atom does not decay directly to the ground state which is detected eventually. To confirm the second reason, we did a Monte Carlo simulation of the decaying process as shown in the next section.

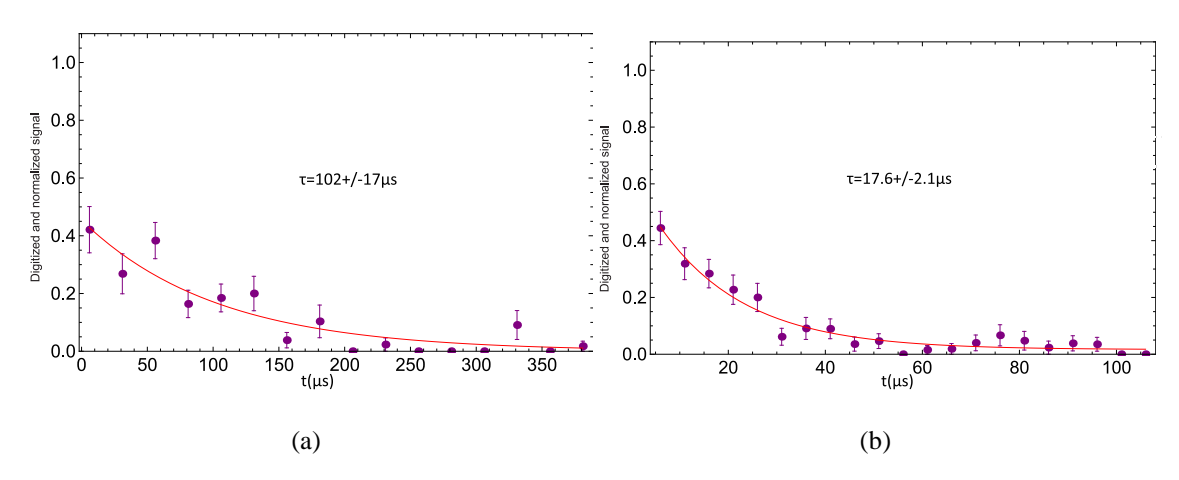


Figure 7.15 Lifetime measurement of Rydberg state $61D_{3/2}$ with the bottle trap (a)on and (b)off.

7.5.4 Monte Carlo Simulation of Rydberg Decay

To simulate the decay process, we consider all the transition channels. The rate of spontaneous transition between nL and n'L' is given by [Beterov 09]

$$A(nL \to n'L') = \frac{e^2 a_0^2}{3\pi\epsilon_0 \hbar c^3} \frac{\omega_{nn'}^3 L_{max}}{2L+1} R^2 (nL \to n'L')$$
 (7.22)

where L_{max} is the larger of L and L', $\omega_{nn'} = |E_{nL} - E_{n'L'}|/\hbar$, and the radial matrix element $R(nL \to n'L')$ is calculated numerically with the method in Chap.3 (in atomic units). The black-body radiation(BBR) induced transition rate is given by

$$W(nL \to n'L') = A(nL \to n'L') \frac{1}{\exp(\hbar\omega_{nn'}/k_BT) - 1}$$
(7.23)

We compared the numerically calculated lifetime values with the numbers given by Equation 7.7, in Figure 7.16, in which $1/\tau_0 = \Gamma_0 = \sum_{E_{nL} > E_{n'L'}} A(nL \to n'L')$, $\Gamma_{BBR} = \sum_{n'L'} W(nL \to n'L')$, and $\tau = 1/(\Gamma_0 + \Gamma_{BBR})$. It shows a pretty good agreement.

To do the Monte Carlo simulation, the spontaneous and BBR transition rates to all the other states

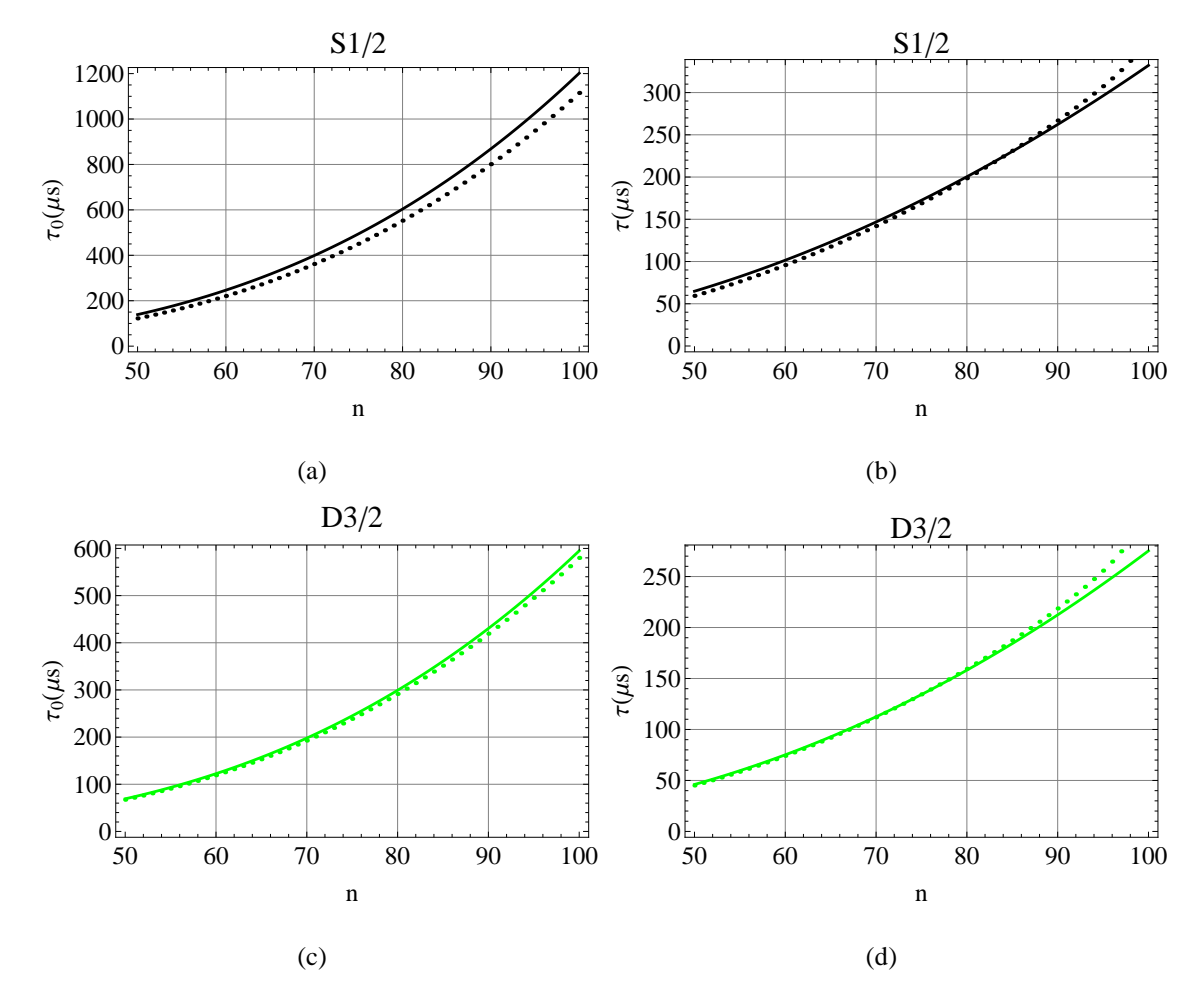


Figure 7.16 Verification of the numerical lifetime calculation. (Solid lines represent calculated values from the empirical Equation 7.7, and dotted lines represent numerical results).

are first calculated for each state, from n=5 to n=100, with angular quantum number $L\leq 3$. Then decay process is simulated with a random number generator. For the Cs $61D_{3/2}$ state in Figure 7.17 and 7.18, the maximum simulated time of decay is $200\mu s$ with time step $dt=0.1\mu s$. A total of 10000 atoms are simulated. To verify the parameters, a test is run with the assumption that the Rydberg atom decays directly to the ground state. So the ground state population curve should follow the simple curve of $P_g(t)=1-\exp(-t/\tau_{61D_{3/2}})$, as shown in Figure 7.17. The actual simulation results are in Figure 7.18. So the simulated time constant for the atom to decay back to the ground state is $143\mu s$, greater than the natural decay time as expected. The average time the atom spent on each state is shown in Figure 7.18(b).

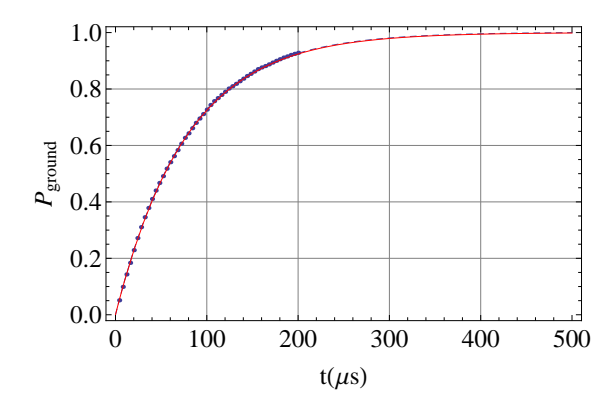


Figure 7.17 Verification of the Monte Carlo simulation, assuming Rydberg Cs atom $61D_{3/2}$ decays directly the the ground state.

From the simulation results, we get a time constant of decaying to ground state $\tau=143\mu s$. Using the measured lifetime in Figure 7.15(a) $\tau=102\pm17\mu s$, we get a trap lifetime $\tau_{bob}=356\mu s$, with bounds $210\mu s \leq \tau_{bob} \leq 709\mu s$, which is consistent with the analysis results in Section 7.5.2.

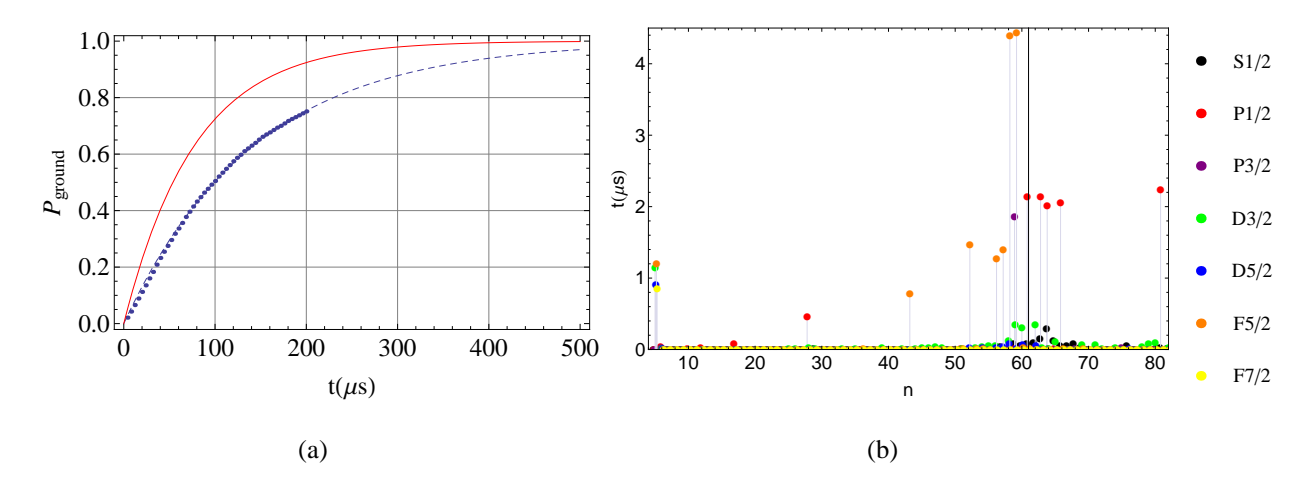


Figure 7.18 Ground state population results of Monte Carlo decay simulation for Cs state $61D_{3/2}$, T=300K, (a)ground state population, with blue dots representing the simulation, red solid curve represents the lifetime curve, time constant $\tau_{red}=77.5\mu \text{s}$, $\tau_{blue}=143\mu \text{s}$, (b)the average time the atom spent on each intermediate state before decaying to the ground state.

Chapter 8

Summary

In summary, we have designed three types of bottle beam trap, and have demonstrated a micrometer-sized crossed vortex BBT. It is shown that single Cs atoms could be loaded into the BBT with 50% probability, and the atoms have lifetimes of several seconds and coherence times as long as \sim 43ms, and single qubit gates can be performed on the trapped atoms with a fidelity of around 70%.

We have theoretically investigated the effect of the BBTs on the energies of Rydberg states, and have come up with a scheme to reduce the differential AC Stark shifts between Rydberg and ground levels.

We have also successfully excited trapped single Cs atoms to high lying Rydberg states, and have demonstrated the Rydberg atoms could be trapped in the BBT for a time longer than their intrinsic lifetime.

We can thus conclude that the BBT is a promising building block for Rydberg-mediated multi-qubit quantum information experiments.

LIST OF REFERENCES

- [Abrams 97] Daniel S. Abrams & Seth Lloyd. *Simulation of Many-Body Fermi Systems on a Universal Quantum Computer*. Phys. Rev. Lett., vol. 79, page 2586, 1997.
- [Anderson 11] S. E. Anderson, K. C. Younge & G. Raithel. *Trapping Rydberg Atoms in an Optical Lattice*. Phys. Rev. Lett., vol. 107, page 263001, 2011.
- [Bateman 10] J. E. Bateman, R. L. D. Murray, M. Himsworth, H. Ohadi, A. Xuereb & T. Freegarde. *HnschCouillaud locking of MachZehnder interferometer for carrier removal from a phase-modulated optical spectrum*. J. Opt. Soc. Am. B, vol. 27, page 1530, 2010.
- [Beijersbergen 94] M. W. Beijersbergen, R. P. C. Coerwinkel, M. Kristensen & J. P. Woerdman. Helical-wavefront laser beams produced with a spiral phaseplate. Opt. Commun., vol. 112, page 321, 1994.
- [Beterov 09] I. I. Beterov, I. I. Ryabtsev, D. B. Tretyakov & V. M. Entin. *Quasiclassical calculations of blackbody-radiation-induced depopulation rates and effective lifetimes of Rydberg* nS, nP, and nD alkali-metal atoms with $n \le 80$. Phys. Rev. A, vol. 79, page 052504, 2009.
- [Beterov 12] I I Beterov, C W Mansell, E A Yakshina, I I Ryabtsev, D B Tretyakov, V M Entin, C MacCormick, M J Piotrowicz, A Kowalczyk & S Bergamini. *Cooper minima in the transitions from low-excited and Rydberg states of alkali-metal atoms*. arXiv:1207.3626, Jul 2012.
- [Bethe 57] H. A. Bethe & E. E. Salpeter. Quantum mechanics of one-and two-electron atoms. Springer-Verlag, 1957.
- [Bjorkholm 88] J. E. Bjorkholm. *Collision-limited lifetimes of atom traps*. Phys. Rev. A, vol. 38, page 1599, 1988.
- [Blatt 12] R. Blatt & C. F. Roos. *Quantum simulations with trapped ions*. Nature Phys., vol. 8, page 277, 2012.
- [Dalibard 89] J. Dalibard & C. Cohen-Tannoudji. *Laser cooling below the Doppler limit by polarization gradients: simple theoretical models*. J. Opt. Soc. Am. B, vol. 6, page 2023, 1989.

- [Davidson 95] Nir Davidson, Heun Jin Lee, Charles S. Adams, Mark Kasevich & Steven Chu. *Long Atomic Coherence Times in an Optical Dipole Trap.* Phys. Rev. Lett., vol. 74, page 1311, 1995.
- [Dennis 09] Mark R. Dennis, Kevin O'Holleran & Miles J. Padgett. *Singular Optics: Optical Vortices and Polarization Singularities*. Progess in Optics, vol. 53, page 293, 2009.
- [DiVincenzo 01] D. P. DiVincenzo. *Dogma and heresy in quantum computing*. Quantum Inform. Comput., vol. 1, page 1, 2001.
- [DiVincenzo 09] David P. DiVincenzo. Fault tolerant architectures for superconducting qubits. Phys. Scr., vol. T 137, page 014020, 2009.
- [Donley 05] E. A. Donley, T. P. Heavner, F. Levi, M. O. Tataw & S. R. Jefferts. *Double-pass acousto-optic modulator system*. Rev. Sci. Instrum., vol. 76, page 063112, 2005.
- [Drewsen 94] M. Drewsen, Ph. Laurent, A. Nadir, G. Santarelli, A. Clairon, Y. Castin, D. Grison & C. Salomon. *Investigation of sub-Doppler cooling effects in a cesium magneto-optical trap.* Appl. Phys. B, vol. 59, page 283, 1994.
- [Dutta 00] S. K. Dutta, J. R. Guest, D. Feldbaum, A. Walz-Flannigan & G. Raithel. *Ponderomotive optical lattice for Rydberg atoms*. Phys. Rev. Lett., vol. 85, page 5551, 2000.
- [Fatemi 07] F. K. Fatemi, M. Bashkansky & Z. Dutton. *Dynamic high-speed spatial manipulation of cold atoms using acousto-optic and spatial light modulation*. Opt. Express, vol. 15, page 3589, 2007.
- [Friedman 00] N. Friedman, L. Khaykovich, R. Ozeri & N. Davidson. *Compression of cold atoms to very high densities in a rotating-beam blue-detuned optical trap.* Phys. Rev. A, vol. 61, page 031403, 2000.
- [Fuhrmanek 11] A. Fuhrmanek, R. Bourgain, Y. R. P. Sortais & A. Browaeys. *Free-Space Lossless State Detection of a Single Trapped Atom*. Phys. Rev. Lett., vol. 106, page 133003, 2011.
- [Gallagher 94] T. F. Gallagher. Rydberg atoms. Cambridge University Press, 1994.
- [Gibbons 11] Michael J. Gibbons, Christopher D. Hamley, Chung-Yu Shih & Michael S. Chapman. *Nondestructive Fluorescent State Detection of Single Neutral Atom Qubits*. Phys. Rev. Lett., vol. 106, page 133002, 2011.
- [Grier 03] David G. Grier. *A revolution in optical manipulation*. Nature, vol. 424, page 01935, 2003.
- [Grimm 00] Rudolf Grimm, Matthias Weidemller & Yurii B. Ovchinnikov. *optical dipole traps for neutral atoms*. Adv. At. Mol. Opt. Phys., vol. 42, page 95, 2000.

- [Grover 97] L. K. Grover. Quantum mechanics helps in searching for a needle in a haystack. Phys. Rev. Lett., vol. 79, page 325, 1997.
- [Hansch 80] T. W. Hansch & B. Couillaud. Laser frequency stabilization by polarization spectroscopy of a reflecting reference cavity. Opt. Commun., vol. 35, page 441, 1980.
- [Isenhower 09] L. Isenhower, W. Williams, A. Dally & M. Saffman. *Atom trapping in an interferometrically generated bottle beam trap.* Opt. Lett., vol. 34, page 1159, 2009.
- [Isenhower 10a] L. Isenhower. *Demonstration of Rydberg blockade, a neutral atom CNOT gate, and entanglement generation.* PhD thesis, University of Wisconsin-Madison, 2010.
- [Isenhower 10b] L. Isenhower, E. Urban, X. L. Zhang, A. T. Gill, T. Henage, T. A. Johnson, T. G. Walker & M. Saffman. *Demonstration of a Neutral Atom Controlled-NOT Quantum Gate*. Phys. Rev. Lett., vol. 104, page 010503, 2010.
- [Jaksch 99] D. Jaksch, H.-J. Briegel, J. I. Cirac, C. W. Gardiner & P. Zoller. *Entanglement of Atoms via Cold Controlled Collisions*. Phys. Rev. Lett., vol. 82, page 1975, 1999.
- [Jaksch 00] D. Jaksch, J. I. Cirac, P. Zoller, S. L. Rolston, R. Côté & M. D. Lukin. *Fast Quantum Gates for Neutral Atoms*. Phys. Rev. Lett., vol. 85, page 2208, 2000.
- [Jersblad 00] J. Jersblad, H. Ellmann & A. Kastberg. *Experimental investigation of the limit of Sisyphus cooling*. Phys. Rev. A, vol. 62, page 051401(R), 2000.
- [Johnson 83] W. Johnson, D. Kohb & K.-N. Huang. *Electric-dipole, quadrupole, and magnetic-dipole susceptibilities and shielding factors for closed-shell ions of the image, and image isoelectronic sequences*. At. Data Nucl. Data, vol. 28, page 33, 1983.
- [Kassal 08] I. Kassal, S. P. Jordan, P. J. Love, M. Mohseni & A. Aspuru-Guzik. *Polynomial-time quantum algorithm for the simulation of chemical dynamics*. Proc. Natl. Acad. Sci. USA., vol. 105, page 18681, 2008.
- [Kuga 97] Takahiro Kuga, Yoshio Torii, Noritsugu Shiokawa, Takuya Hirano, Yukiko Shimizu & Hiroyuki Sasada. *Novel Optical Trap of Atoms with a Doughnut Beam.* Phys. Rev. Lett., vol. 78, page 4713, 1997.
- [Kuhr 05] S. Kuhr, W. Alt, D. Schrader, I. Dotsenko, Y. Miroshnychenko, A. Rauschenbeutel & D. Meschede. *Analysis of dephasing mechanisms in a standing-wave dipole trap.* Phys. Rev. A, vol. 72, page 023406, 2005.
- [Kulin 01] S. Kulin, S. Aubin, S. Christe, B. Peker, S. L. Rolston & L. A. Orozco. *A single hollow-beam optical trap for cold atoms*. J. Opt. B: Quantum Semiclassical. Opt., vol. 3, page 353, 2001.

- [Li 12] G. Li, S. Zhang, L. Isenhower, K. Maller & M. Saffman. *A crossed vortex bottle beam trap for single-atom qubits*. Opt. Lett., vol. 37, page 851, 2012.
- [Lorenzen 84] C. J. Lorenzen & K. Niemax. *Precise quantum defects of nS, nP, and nD levels in Cs I*. Zeitschrift fr Physik A Hadrons and Nuclei, vol. 315, page 127, 1984.
- [Maurer 12] P. C. Maurer, G. Kucsko, C. Latta, L. Jiang, N. Y. Yao, S. D. Bennett, F. Pastawski, D. Hunger, N. Chisholm, M. Markham, D. J. Twitchen, J. I. Cirac & M. D. Lukin. *Room-Temperature Quantum Bit Memory Exceeding One Second.* Science, vol. 336, page 1283, 2012.
- [Mawardi 11] A. Mawardi, S. Hild, A. Widera & D. Meschede. *ABCD-treatment of a propagating doughnut beam generated by a spiral phase plate*. Opt. Express, vol. 19, page 21205, 2011.
- [Nelson 07] K. D. Nelson, X. Li & D. S. Weiss. *Imaging single atoms in a three-dimensional array*. Nature Phys., vol. 3, page 556, 2007.
- [Nielsen 00] Michael A. Nielsen & Issaac L. Chuang. Quantum computation and quantum information. Cambridge University Press, 2000.
- [Niemax 75] K. Niemax & G. Pichle. *New aspects in the self-broadening of alkali resonance lines*. J. Phys. B: Atom. Molec. Phys., vol. 8, page 179, 1975.
- [Olson 07] Spencer E. Olson, Matthew L. Terraciano, Mark Bashkansky & Fredrik K. Fatemi. *Cold-atom confinement in an all-optical dark ring trap*. Phys. Rev. A, vol. 76, page 061404, 2007.
- [Ovchinnikov 97] Yu. B. Ovchinnikov, I. Manek & R. Grimm. *Surface Trap for Cs atoms based on Evanescent-Wave Cooling*. Phys. Rev. Lett., vol. 79, page 2225, 1997.
- [Ozeri 99] Roee Ozeri, Lev Khaykovich & Nir Davidson. *Long spin relaxation times in a single-beam blue-detuned optical trap.* Phys. Rev. A, vol. 59, page R1750, 1999.
- [Paik 11] Hanhee Paik, D. I. Schuster, Lev S. Bishop, G. Kirchmair, G. Catelani, A. P. Sears, B. R. Johnson, M. J. Reagor, L. Frunzio, L. I. Glazman, S. M. Girvin, M. H. Devoret & R. J. Schoelkopf. Observation of High Coherence in Josephson Junction Qubits Measured in a Three-Dimensional Circuit QED Architecture. Phys. Rev. Lett., vol. 107, page 240501, 2011.
- [Pellizzari 95] T. Pellizzari, S. A. Gardiner, J. I. Cirac & P. Zoller. *Decoherence, Continuous Observation, and Quantum Computing: A Cavity QED Model.* Phys. Rev. Lett., vol. 75, page 3788, 1995.
- [Press 92] William H. Press, Saul A. Teukolsky, William T. Vetterling & Brian P. Flannery. Numerical recipes in fortran 77. Cambridge University Press, 1992.
- [Puppe 07] T. Puppe, I. Schuster, A. Grothe, A. Kubanek, K. Murr, P. W. H. Pinkse & G. Rempe. *Trapping and Observing Single Atoms in a Blue-Detuned Intra*cavity Dipole Trap. Phys. Rev. Lett., vol. 99, page 013002, 2007.

- [Robicheaux 96] F. Robicheaux. *Electron impact ionization of* H_2^+ . J. Phys. B: At. Mol. Opt. Phys., vol. 29, page 779, 1996.
- [Robicheaux 97] F. Robicheaux & J. Shaw. *Calculated electron dynamics in an electric field*. Phys. Rev. A, vol. 56, page 278, 1997.
- [Saffman 05] M. Saffman & T. G. Walker. *Analysis of a quantum logic device based on dipole-dipole interactions of optically trapped Rydberg atoms*. Phys. Rev. A, vol. 72, page 022347, 2005.
- [Saffman 12] M. Saffman. Note on blue lattice. University of Wisconsin-Madison, 2012.
- [Schindler 11] Philipp Schindler, Julio T. Barreiro, Thomas Monz, Volckmar Nebendahl, Daniel Nigg, Michael Chwalla, Markus Hennrich & Rainer Blatt. *Experimental Repetitive Quantum Error Correction*. Science, vol. 332, page 1059, 2011.
- [Schlosser 01] Nicolas Schlosser, Georges Reymond, Igor Protsenko & Philippe Grangier. Sub-poissonian loading of single atoms in a microscopic dipole trap. Nature, vol. 411, page 1024, 2001.
- [Sheng 12] D. Sheng, J. Zhang & L. A. Orozco. Sensitivity test of a blue-detuned dipole trap designed for parity non-conservation measurements in Fr. Rev. Sci. Instrum., vol. 83, page 043106, 2012.
- [Shor 94] P. W. Shor. *Algorithms for quantum computation: discrete logarithms and factoring*. In Proceedings of the 35th Annual Symposium on Foundations of Computer Science, SFCS '94, pages 124–134, Washington, DC, USA, 1994. IEEE Computer Society.
- [Sobelman 92] Igor I. Sobelman. Atomic spectra and radiative transitions. Springer, 2 edition, 1992.
- [Steger 12] M. Steger, K. Saeedi, M. L. W. Thewalt, J. J. L. Morton, H. Riemann, N. V. Abrosimov, P. Becker & H. J. Pohl. *Quantum Information Storage for over 180 s Using Donor Spins in a 28Si "Semiconductor Vacuum"*. Science, vol. 336, page 1280, 2012.
- [Svelto 98] Orazio Svelto & David C. Hanna. Principles of lasers. Springer, 4 edition, 1998.
- [Vasilyev 02] A. A. Vasilyev, I. M. Savukov, M. S. Safronova & H. G. Berry. *Measurement* of the 6s-7p transition probabilities in atomic cesium and a revised value for the weak charge Q_W . Phys. Rev. A, vol. 66, page 020101, 2002.
- [Weber 87] K.-H. Weber & Craig J. Sansonetti. *Accurate energies of nS, nP, nD, nF, and nG levels of neutral cesium.* Phys. Rev. A, vol. 35, page 4650, 1987.
- [Weitenberg 11] Christof Weitenberg, Manuel Endres, Jacob F. Sherson, Marc Cheneau, Peter Schauss, Takeshi Fukuhara, Immanuel Bloch & Stefan Kuhr. *Single-spin addressing in an atomic Mott insulator*. Nature, vol. 471, page 319, 2011.

- [Williams 09] W. Williams. *Cold atom dynamics in linear and nonlinear optical potentials*. PhD thesis, University of Wisconsin-Madison, 2009.
- [Xu 10] P. Xu, X. He, J. Wang & M. Zhan. *Trapping a single atom in a blue detuned optical bottle beam trap.* Opt. Lett., vol. 35, page 2164, 2010.
- [Zhang 10] X. L. Zhang, L. Isenhower, A. T. Gill, T. G. Walker & M. Saffman. *Deterministic entanglement of two neutral atoms via Rydberg blockade*. Phys. Rev. A, vol. 82, page 030306, 2010.
- [Zhang 11] S. Zhang, F. Robicheaux & M. Saffman. *Magic-wavelength optical traps for Rydberg atoms*. Phys. Rev. A, vol. 84, page 043408, 2011.
- [Zhang 12] X. L. Zhang, A. T. Gill, L. Isenhower, T. G. Walker & M. Saffman. Fidelity of a Rydberg-blockade quantum gate from simulated quantum process tomography. Phys. Rev. A, vol. 85, page 042310, 2012.

Appendix A: Zemax Designs

A.1 Vortex Bottle Beam Trap

A.1.1 Aspheric Lens

The asphere we are using is custom made from Optimax. The parameters of the lens is listed in Table A.1. The lens was originally designed for a different window glass (3mm BK7), so the performance is not good for the 1.5mm pyrex window of the square cell. By adding a correction lens, Thorlabs LA1908-A f=500mm spherical lens 50mm in front of the asphere, as shown in Figure A.1, the lens focusing quality is greatly improved.

Table A.1 Parameters of the custom Optimax aspheric lens, CT=15mm, DIA=20mm, CA=18mm.

surface	R	Conic	A4	A6
1	25.66	-1.5474	6.93e-6	-1.77e-9
2	INF	-	-	-

A.1.2 Vortex Bottle System

Our goal is to get a waist size of $2.5\mu\mathrm{m}$ to $3\mu\mathrm{m}$ at the final trap. Since the effective focal length of the 500mm lens + asphere is about 34mm, that means we need a waist size of $2.3\mathrm{mm}\sim2\mathrm{mm}$ before the final focusing. To ensure no loss of information of the Laguerre-Gaussian beam, the lens must cover at least the field for $\rho \leq 4w_0$. Supposing the beam separation is d, then the lens diameter must satisfy $D > d + 4w_0$. The clear aperture is 18mm, which means $d < 8\mathrm{mm}$. To allow for some tolerance, we choose $d = 6\mathrm{mm}$. The beam displacer displaces the beam by 3mm, so we need a telescope of magnification M = 2 after the displacer. Using a f=15.29mm collimating aspheric lens, the maximum output Gaussian beam waist size is about 1.25mm, which is about what we need. But the waist size w_0 of the final Laguerre-Gaussian beam could not be simply calculated by the input Gaussian beam waist w_{in} using $w_0 = f\lambda/\pi w_{in}$ as described in Figure A.2.

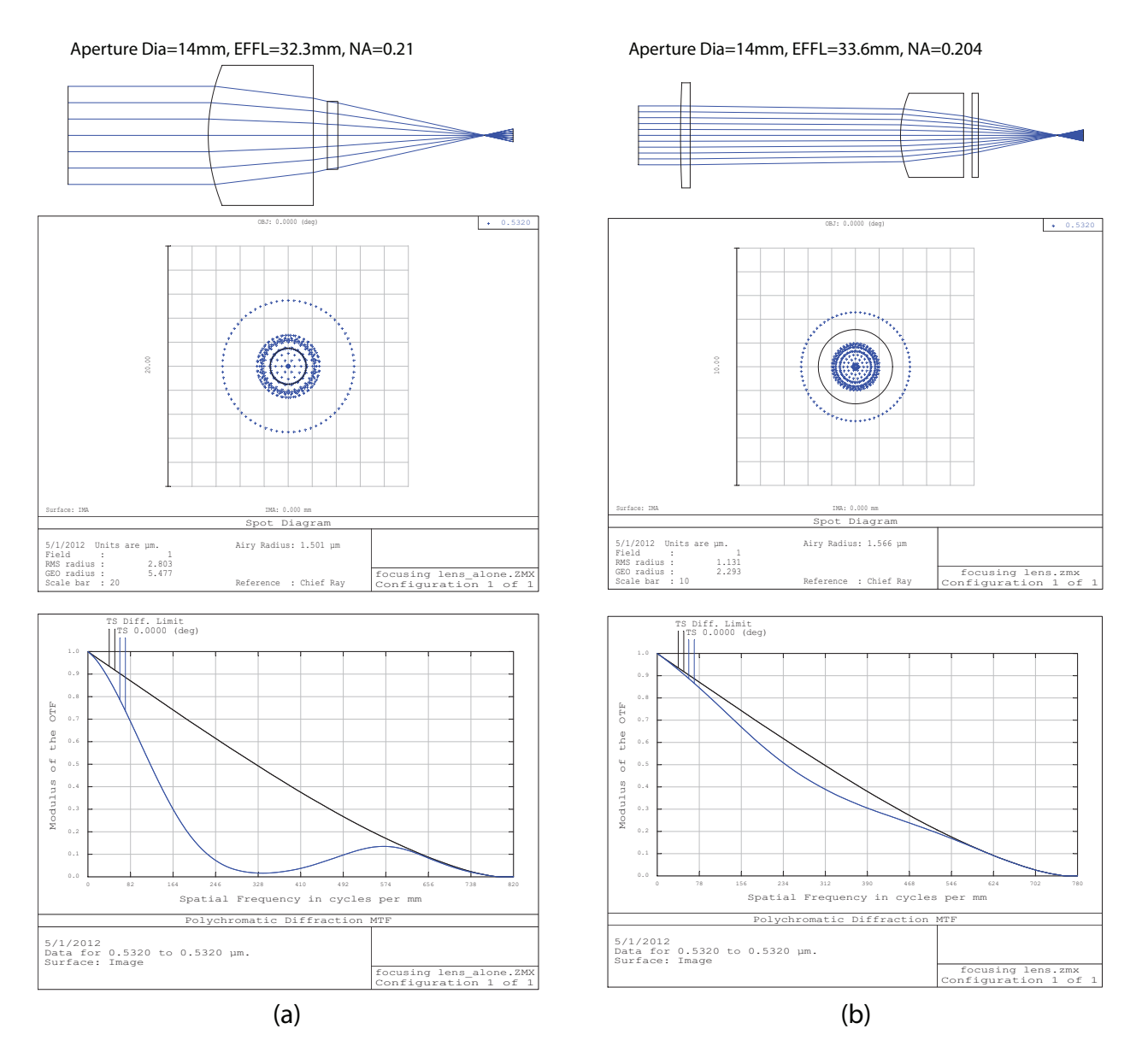


Figure A.1 Performance of the focusing aspheric lens (a)before and (b)after adding a correction lens.

We added a 75mm:60mm telescope in order to get a Laguerre-Gaussian beam well described by $w_0=3\mu\mathrm{m}$.

Figure A.3 is the detailed layout of the optical system for making the vortex bottle beam trap. The part number of the l=1 vortex lens is HOLO/OR VL-209-Q-Y-A. It is made out of 3mm thick fused silica. The part number of the calcite beam displacer is Karl Lambrecht MDBS512-V532.

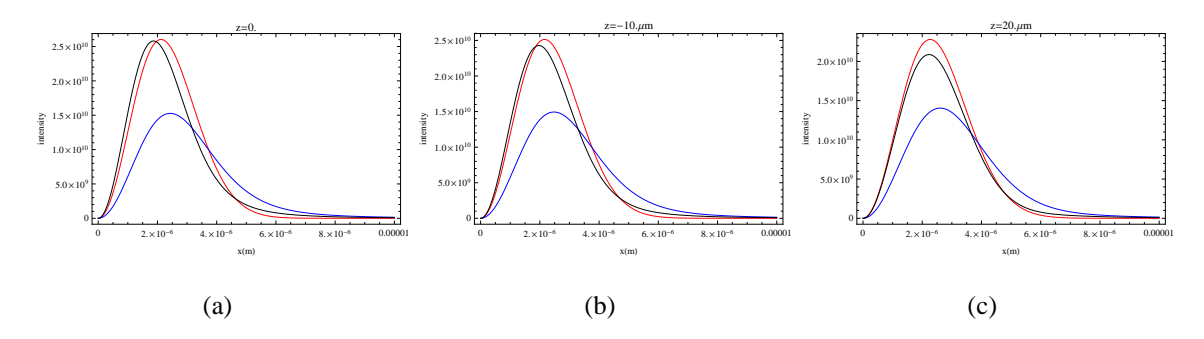


Figure A.2 (red)Intensity profile of a pure LG_{01} mode with $w_0=3\mu\mathrm{m}$; (blue)intensity profile calculated from diffraction, with a Gaussian beam of waist $w_{in}=f\lambda/\pi w_0$ passing through a spiral phase plate, and focused by a lens of focal length f; (black)intensity profile calculated from diffraction, with a Gaussian beam of waist $w_{in}=1.3f\lambda/\pi w_0$ passing through a spiral phase plate, and focused by a lens of focal length f.

It separates the beams with orthogonal polarizations by 3mm, and its thickness is 27mm. We did

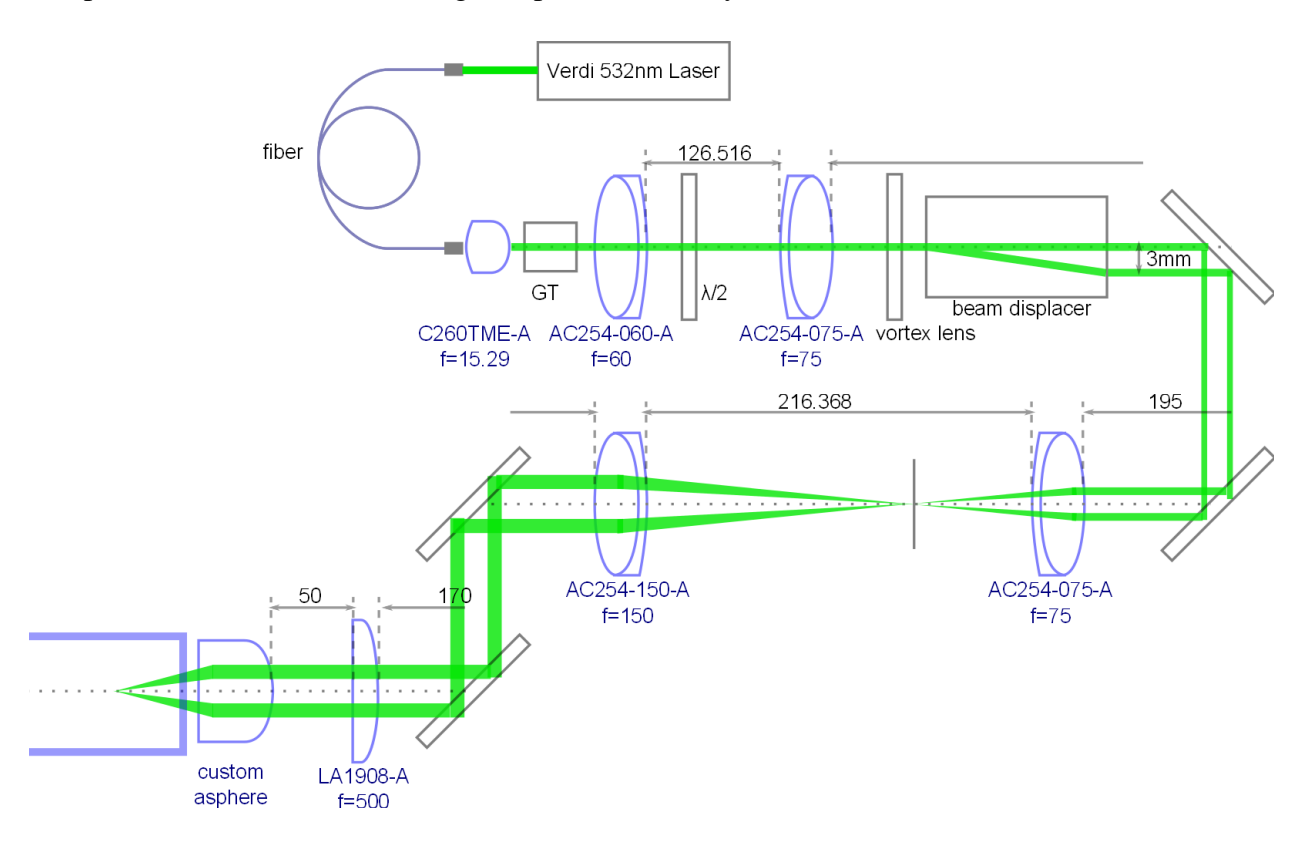


Figure A.3 Layout of the optical system for making the vortex bottle beam trap.

a Physical Optics Propagation (POP) modeling in Zemax with the optics in Figure A.3, using the

equations of Laguerre-Gaussian beams. The results are shown in Figure A.4. Big decentering and tilting of the beam was observed when the beam was coming out of the fiber, due to the imperfect angle of the fiber coupler. So we added to the simulation some tolerance of the lens decentering and tilting. We can see from the simulation results that when the final beam waist is $3\mu m$, the system can tolerate a large misalignment and still make a bottle. As the beam size gets smaller, the requirement on the precision of alignment is higher. We decided to go with the $3\mu m$ waist in our experiments. The beam intensity profile across X and Y on the focus plane is shown in Figure A.5.

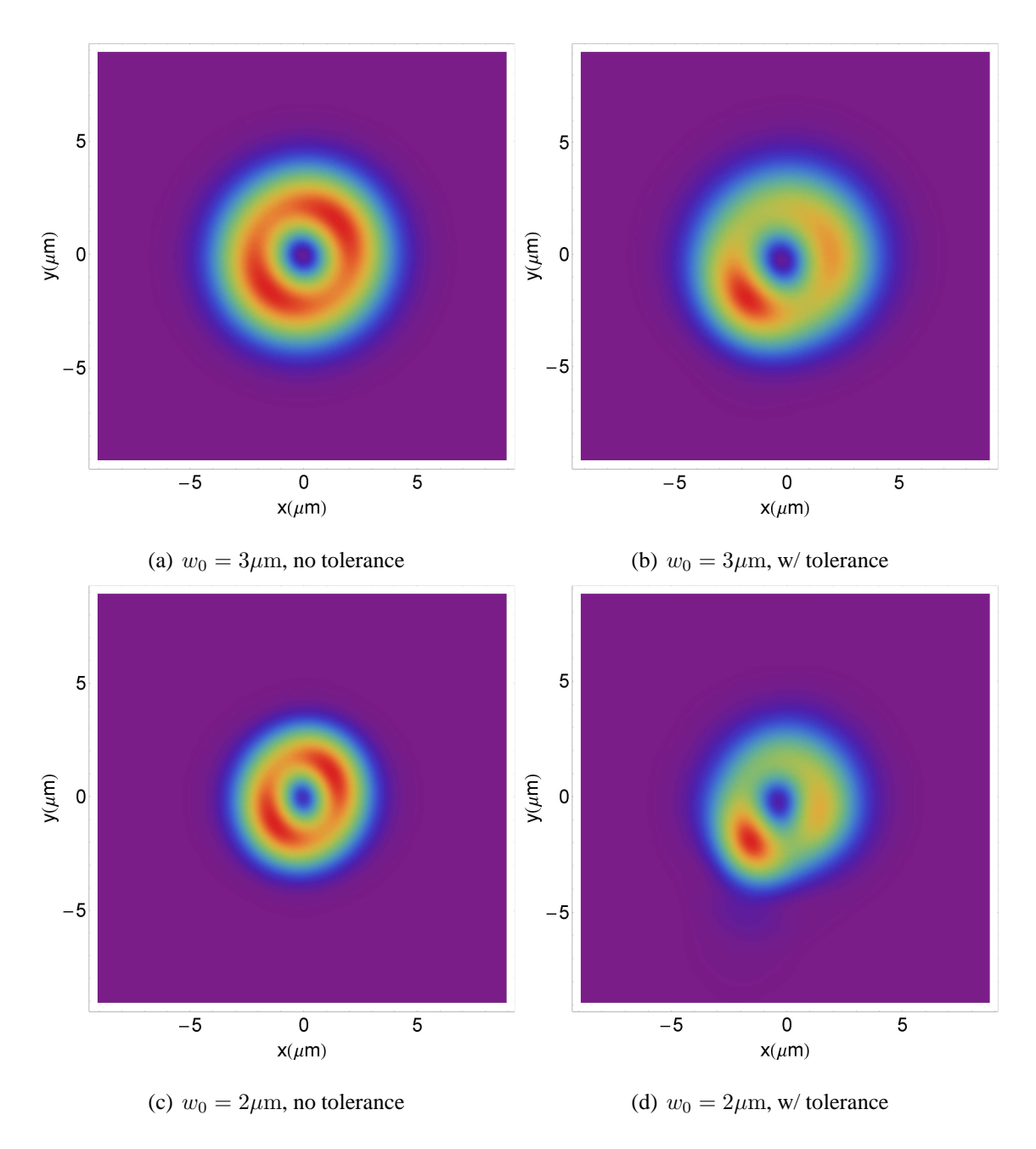


Figure A.4 Zemax POP modeling of the crossed vortex BBT, (a)(c) are assuming the alignments are perfect, (b)(d) include tolerances with up to 0.5mm lens decentering and 0.5 deg lens tilting.

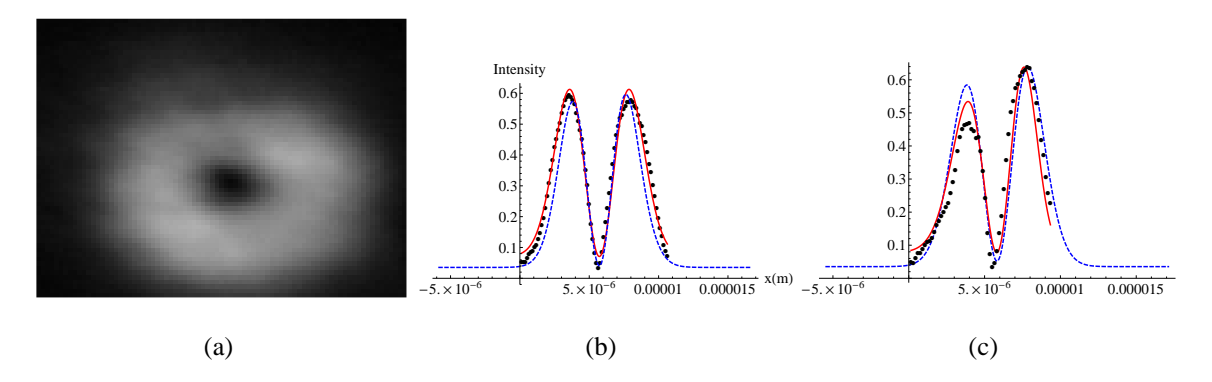


Figure A.5 Measurement of the waist size of the final focused vortex beam (single beam), (a)camera picture, (b)(c)1D intensity profile, measured data(black dots),theoretical calculation from LG_{01} mode with $w_0=3\mu\mathrm{m}$ (red line), and Zemax simulation(blue dashed).

Appendix B: Electric Field of a Strongly Focused Gaussian Beam

B.1 Field behind the lens

Suppose the waist (w_1) of the input Gaussian beam is at the front focal plane of the lens, and it is right hand polarized. The electric field can be calculated by

$$\vec{E}(\rho, z = -2f) = E_0 \hat{\varepsilon}_+ e^{-\rho^2/w_1^2},$$
 (B.1)

where $E_0 = \frac{1}{w_1} \sqrt{\frac{4P_{in}}{\varepsilon_0 \pi c}}$, $\rho = \sqrt{x^2 + y^2}$ and z = 0 is set at the back focal plane of the lens. Then the field at the front surface of the lens is

$$\vec{E}_{front}(z=-f) = E_1 \hat{\varepsilon}_+ e^{-\rho^2/w_1^2} e^{ikf + \frac{ik\rho^2}{2R_1} - i\arctan\frac{f}{z_R}}, \tag{B.2}$$

in which
$$E_1=E_0\frac{w_0}{w_1},$$
 $z_R=\pi w_0^2/\lambda,$ $w_1=w_0\sqrt{1+(z/z_R)^2},$ and $R_1=z(1+(z_R/z)^2).$

And ideal lens should focus a plane wave such that it becomes a point source at the focus. So it is reasonable to assume the high N.A. lens introduces a spherical phase shift

$$\varphi_{sp} = \exp(-ik\sqrt{\rho^2 + f^2} + ikf). \tag{B.3}$$

Based on the projection of the \vec{k} vector, and the fact that this is a transverse mode, after going through the lens the polarization of the light changes according to

$$\hat{\varepsilon}_{\pm}(\rho) \to \frac{1 + \cos\theta}{2} \hat{\varepsilon}_{\pm} + \frac{\sin\theta e^{\pm i\phi}}{\sqrt{2}} \hat{z} + \frac{\cos\theta - 1}{2} e^{\pm 2i\phi} \hat{\varepsilon}_{\mp}, \tag{B.4}$$

where $\theta = \arctan(\frac{\rho}{f})$.

The overall electric field at the back surface of the lens becomes

$$\vec{E}_{back}(\rho, \phi, z = -f) = E_1 \frac{1}{\sqrt{\cos \theta}} \left(\frac{1 + \cos \theta}{2} \hat{\varepsilon}_+ + \frac{\sin \theta e^{i\phi}}{\sqrt{2}} \hat{z} + \frac{\cos \theta - 1}{2} e^{2i\phi} \hat{\varepsilon}_- \right) \times \exp(-\rho^2/w_1^2 + 2ikf - ik\sqrt{\rho^2 + f^2} + \frac{ik\rho^2}{2R_1} - i\arctan\frac{f}{z_R}).$$
(B.5)

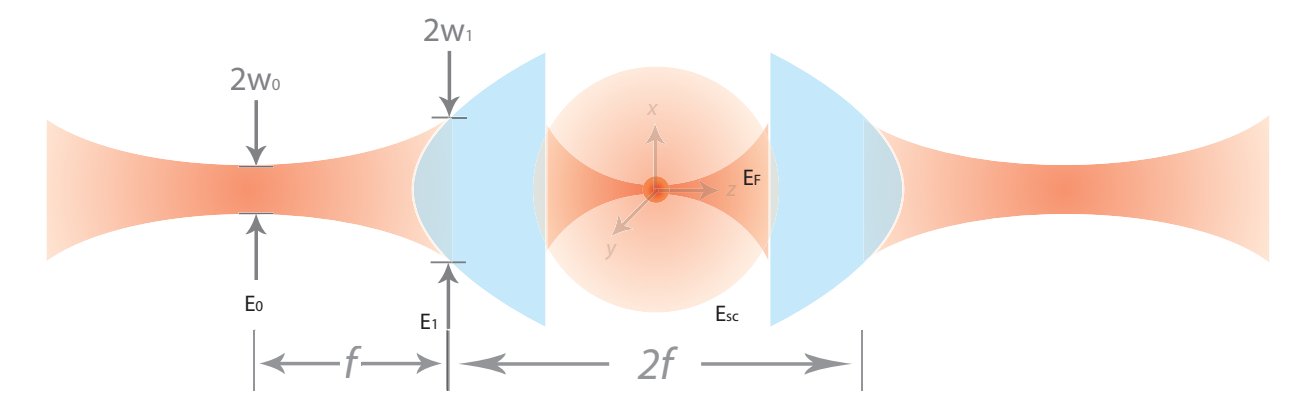


Figure B.1 Electric field of a strongly focused Gaussian beam.

B.2 Paraxial Approximation

In the simple paraxial Gaussian beam model, in the confocal configuration, a input beam with waist size w_1 is focused to a beam with a waist size $w_2 = f\lambda/\pi w_1$ at the focus. So the field at the focal plane can be calculated by

$$\vec{E}_{para}(\rho, \phi, z = 0) = E_0 \frac{w_1}{w_2} \hat{\varepsilon}_+ e^{-\rho^2/(w_2)^2 + 2ikf - i\arctan\frac{f}{z_R} - i\arctan\frac{f}{z_R'}}.$$
 (B.6)

Here, $z_R' = \pi(w_2)^2/\lambda$.

B.3 Numerical Propagation To The Focus

For an EM field with cylindrical symmetry, we can expand the field by Debye expansion

$$\vec{E}_F(\rho,\phi,z) = \sum_{\mu} \kappa_{\mu} \vec{F}_{\mu}(\rho,\phi,z), \tag{B.7}$$

where $\sum_{\mu} = \int dk_t \sum_s \sum_m$, k_t is the transverse wave vector, m is an integer valued angular momentum index, and $s=\pm 1$ is the helicity. The complete orthogonal set of modes \vec{F}_{μ} are

$$\vec{F}_{\mu}(\rho,\phi,z) = \frac{1}{4\pi} \frac{sk + k_z}{k} J_{m-1}(k_t \rho) e^{ik_z z} e^{i(m-1)\phi} \hat{\varepsilon}_+ - i \frac{\sqrt{2}}{4\pi} \frac{k_t}{k} J_m(k_t \rho) e^{ik_z z} e^{im\phi} \hat{z} + \frac{1}{4\pi} \frac{sk - k_z}{k} J_{m+1}(k_t \rho) e^{ik_z z} e^{i(m+1)\phi} \hat{\varepsilon}_-,$$
(B.8)

where $k_z = \sqrt{k^2 - k_t^2}$.

For the electric field in Equation B.6, the field after the lens could be numerically integrated by

$$\vec{E}(\rho,\phi,z) = \int dk_t \sum_{s} \sum_{m} \vec{F}_{\mu} = F_{+}\hat{\varepsilon}_{+} + F_{z}\hat{z} + F_{-}\hat{\varepsilon}_{-}, \tag{B.9}$$

in which

$$F_{+} = \sum_{s=\pm 1} \int_{0}^{k} dk_{t} \frac{1}{4\pi} \frac{sk + k_{z}}{k} J_{0}(k_{t}\rho) e^{ik_{z}z} \kappa_{\mu}, \tag{B.10}$$

$$F_z = \sum_{s=\pm 1} \int_0^k dk_t (-i) \frac{\sqrt{2}}{4\pi} \frac{k_t}{k} J_1(k_t \rho) e^{ik_z z} e^{im\phi} \kappa_\mu,$$
 (B.11)

$$F_{-} = \sum_{s=+1} \int_{0}^{k} dk_{t} \frac{1}{4\pi} \frac{sk - k_{z}}{k} J_{2}(k_{t}\rho) e^{ik_{z}z} e^{2i\phi} \kappa_{\mu}, \tag{B.12}$$

and

$$\kappa_{\mu}(k_{t}) = E_{1}e^{2ikf - i\arctan\frac{f}{2R}}\delta_{m1}\pi k_{t} \int_{0}^{\infty}\rho d\rho \frac{1}{\sqrt{\cos\theta}} \left\{ \left(\frac{1 + \cos\theta}{2}\right) \frac{sk + k_{z}}{k} J_{0}(k_{t}\rho) + \frac{\sin\theta}{\sqrt{2}} \frac{i\sqrt{2}k_{t}}{k} J_{1}(k_{t}\rho) + \left(\frac{\cos\theta - 1}{2}\right) \frac{sk - k_{z}}{k} J_{2}(k_{t}\rho) \right\} \exp\left[-ik\sqrt{\rho^{2} + f^{2}} + ik_{z}f + \frac{ik\rho^{2}}{2R_{1}} - \rho^{2}/w_{1}^{2}\right].$$
(B.13)

We can immediately see that on the axis where $\rho=0$, $J_1(0)=0$, $J_2(0)=0$, only the $F_+\hat{\varepsilon}_+$ term left. So the polarization on the optical axis after the lens is the same as that before the lens. Some numerical integration results are shown in Figure B.2. At high focusing powers, the electric field is more spread out than the field calculated from paraxial approximation

The field at the focal point has a simple analytical form

$$\vec{E}(\rho=0,\phi,z=0) = -E_1 \frac{ikf}{4} \exp\left(2ikf - i\arctan\frac{f}{z_R} + \frac{f^2}{w_1^2} - \frac{ikf^2}{2R_1}\right) \left[E_{\frac{3}{4}}(\frac{f^2}{w_1^2} - \frac{ikf^2}{2R_1}) + E_{\frac{5}{4}}(\frac{f^2}{w_1^2} - \frac{ikf^2}{2R_1})\right] \hat{\varepsilon}_+,$$
(B.14)

where $E_n(x) = \int_1^\infty e^{-xt} t^{-n} dt$. The amplitude

$$E_A = |\vec{E}(\rho = 0, \phi, z = 0)| = \sqrt{\frac{\pi P_{in}}{\epsilon_0 c \lambda^2}} \frac{f}{w_1} e^{\frac{f^2}{w_1^2}} \left| E_{\frac{3}{4}} \left(\frac{f^2}{w_1^2} - \frac{ikf^2}{2R_1} \right) + E_{\frac{5}{4}} \left(\frac{f^2}{w_1^2} - \frac{ikf^2}{2R_1} \right) \right|.$$
 (B.15)

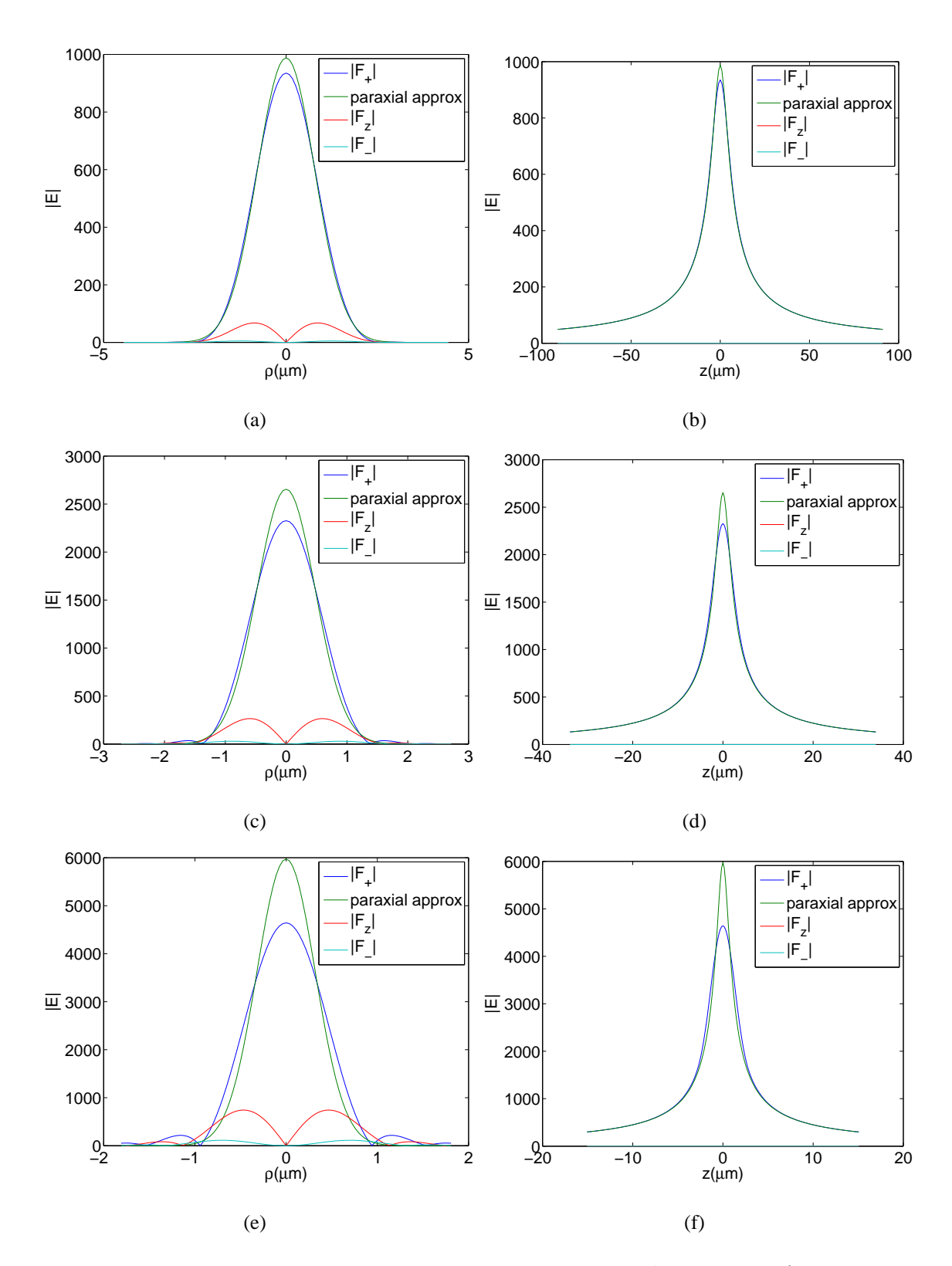


Figure B.2 Field at the focus for different focusing powers with $\lambda=852\mathrm{nm},\,f=4.5\mathrm{mm},$ and (a)(b) $w_1=1.1\mathrm{mm},$ (c)(d) $w_1=1.8\mathrm{mm},$ (e)(f) $w_1=2.7\mathrm{mm},$ and the field amplitudes are normalized to $|E_1|$ on the front surface of the lens.

B.4 Scattering Ratio

For a two level system, the scattering rate of single atom on a laser beam with intensity I and detuning Δ is given by

$$R_{sc} = \left(\frac{\Gamma}{2}\right) \frac{I/I_{sat}}{1 + 4(\Delta/\Gamma)^2 + (I/I_{sat})}.$$

In the limit of weak probe beam ($I \ll I_{sat}$), the ratio of scattered power to the input power is

$$r_{sc} = \left(\frac{\hbar\omega\Gamma}{2P_{in}}\right) \frac{I/I_{sat}}{1 + 4(\Delta/\Gamma)^2}.$$
 (B.16)

If the atom is located at the focal point of the lens, $I = \frac{c\epsilon_0}{2}E_A^2$. If the laser is near resonant, the ratio simplifies to

$$r_{sc} = \left(\frac{3c\epsilon_0 \lambda^2 E_A^2}{4\pi P_{in}}\right) \frac{1}{1 + 4(\Delta/\Gamma)^2}.$$
(B.17)

If we use the Gaussian paraxial approximation

$$R_{sc} = \frac{3w_1^2}{f^2}. ag{B.18}$$

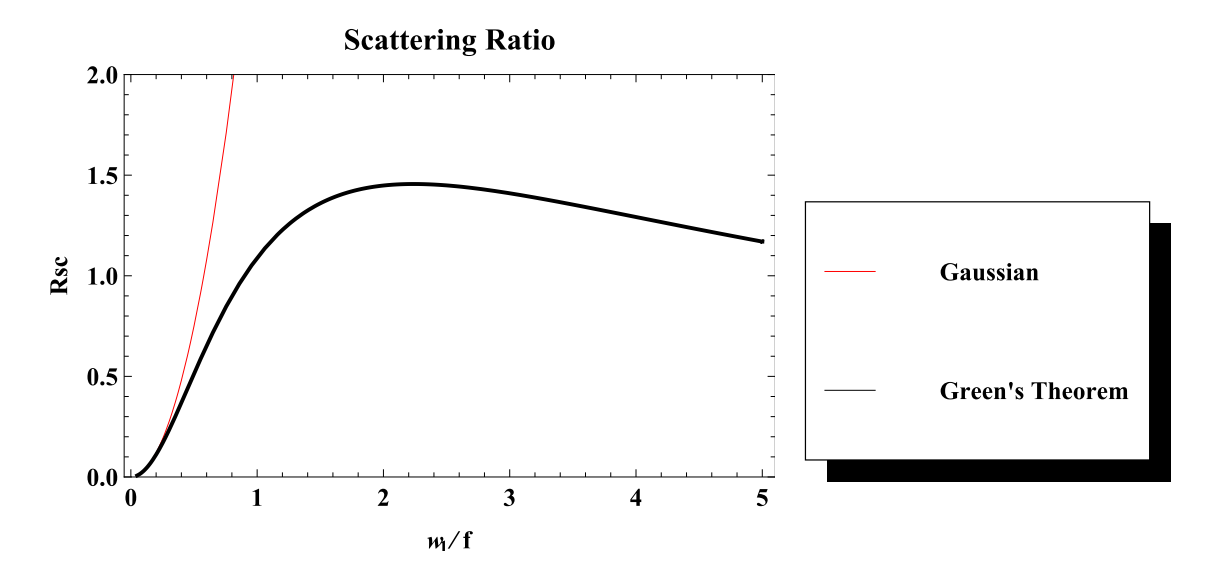


Figure B.3 Scattering ratio of strongly focused Gaussian beam of a single atom for different waist sizes.

B.5 Transmission and Phase Shift

In the far field limit, the dipole field radiated by the atom is

$$\vec{E}_{sc}(\vec{r}) = \frac{3E_A e^{i(kr+\pi/2)}}{2kr} [\hat{\varepsilon}_+ - (\hat{\varepsilon}_+ \cdot \hat{r})\hat{r}] \frac{i\Gamma}{2\Delta + i\Gamma}.$$
 (B.19)

At the output lens, the original field is

$$\vec{E}_{F}(\rho,\phi,z=f) = E_{1} \frac{1}{\sqrt{\cos\theta}} \left(\frac{1+\cos\theta}{2} \hat{\varepsilon}_{+} - \frac{\sin\theta e^{i\phi}}{\sqrt{2}} \hat{z} + \frac{\cos\theta - 1}{2} e^{2i\phi} \hat{\varepsilon}_{-} \right) \\ \exp(-\rho^{2}/w_{1}^{2} + 2ikf + ik\sqrt{\rho^{2} + f^{2}} - \frac{ik\rho^{2}}{2R_{1}} - i\arctan\frac{f}{z_{R}} + i\pi).$$
(B.20)

So the total electric field is

$$\vec{E}_t = \vec{E}_{sc} + \vec{E}_F. \tag{B.21}$$

If only the mode that is the same as the probe beam is collected, the peak electric field after the second lens is

$$E_{out} = E_{in} \frac{\int_{z=f} \hat{k} \cdot \hat{n} dS(\vec{E}_{sc} + \vec{E}_{F}) \cdot \vec{E}_{F}^{*}}{\int_{z=f} \hat{k} \cdot \hat{n} dS \vec{E}_{F} \cdot \vec{E}_{F}^{*}}$$

$$= E_{in} \left(1 + \frac{i\Gamma}{2\Delta + i\Gamma} \cdot \frac{\int 3E_{1}E_{A}e^{-i\pi/2 - 2ikf + i\arctan\frac{f}{z_{R}} - \rho^{2}/w_{1}^{2} + \frac{ik\rho^{2}}{2R_{1}}} \frac{(1 + \cos\theta)}{4k\sqrt{f^{2} + \rho^{2}}\sqrt{\cos\theta}} \cos\theta dS} \right)$$

$$= E_{in} \left(1 - \frac{i\Gamma}{2\Delta + i\Gamma} \cdot \frac{3f^{2}}{8w_{1}^{2}} e^{\frac{2f^{2}}{w_{1}^{2}} - \frac{ikf^{2}}{R_{1}}} \left[E_{\frac{3}{4}} \left(\frac{f^{2}}{w_{1}^{2}} - \frac{ikf^{2}}{2R_{1}} \right) + E_{\frac{5}{4}} \left(\frac{f^{2}}{w_{1}^{2}} - \frac{ikf^{2}}{2R_{1}} \right) \right]^{2} \right).$$
(B.22)

Transmission

$$T = \left|1 - \frac{i\Gamma}{2\Delta + i\Gamma} \frac{3f^2}{8w_1^2} e^{\frac{2f^2}{w_1^2} - \frac{ikf^2}{R_1}} \left[E_{\frac{3}{4}} \left(\frac{f^2}{w_1^2} - \frac{ikf^2}{2R_1}\right) + E_{\frac{5}{4}} \left(\frac{f^2}{w_1^2} - \frac{ikf^2}{2R_1}\right)\right]^2\right|^2.$$
 (B.23)

Phase shift with respect to the probe beam going through the double lens system without any atom trapped

$$\Delta \varphi = \arg\left(1 - \frac{i\Gamma}{2\Delta + i\Gamma} \frac{3f^2}{8w_1^2} e^{\frac{2f^2}{w_1^2} - \frac{ikf^2}{R_1}} \left[E_{\frac{3}{4}} \left(\frac{f^2}{w_1^2} - \frac{ikf^2}{2R_1} \right) + E_{\frac{5}{4}} \left(\frac{f^2}{w_1^2} - \frac{ikf^2}{2R_1} \right) \right]^2 \right).$$
 (B.24)

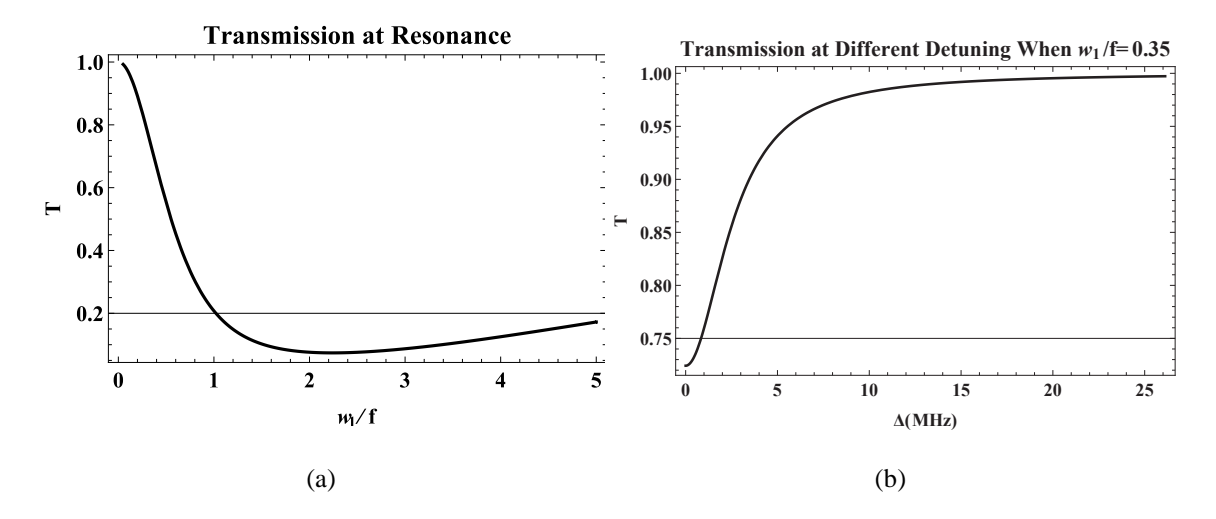


Figure B.4 Transmission of strongly focused Gaussian beam for a single atom (a)at resonance and (b)at different laser detunings.

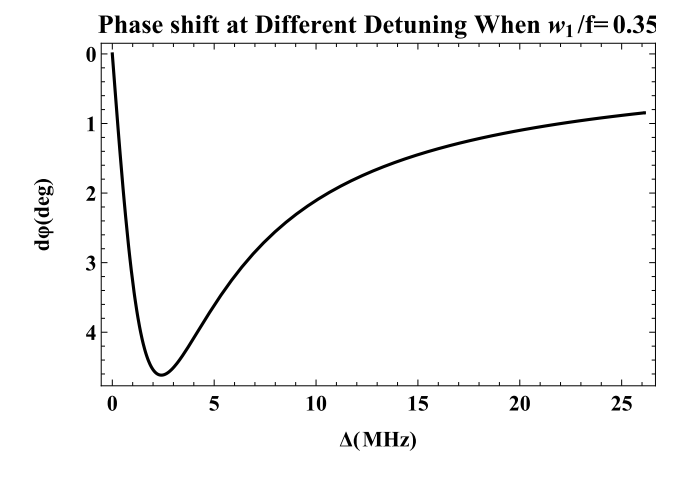


Figure B.5 Phase shift of strongly focused Gaussian beam for a single atom at different laser detunings.